The CSIRO Mk3 Climate System Model

H.B. Gordon, L.D. Rotstayn, J.L. McGregor, M.R. Dix, E.A. Kowalczyk, S.P. O'Farrell,
L.J. Waterman, A.C. Hirst, S.G. Wilson, M.A. Collier, I.G. Watterson, and T.I. Elliott.

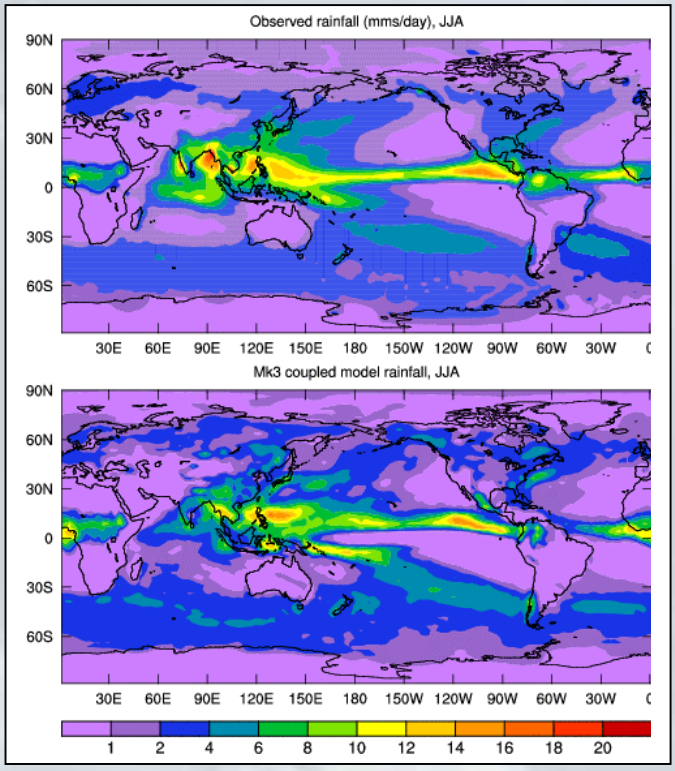

CSIRO
Atmospheric Research

CSIRO Atmospheric Research Technical Paper No.60

CSIRO Atmospheric Research Technical Paper No. 60

The CSIRO Mk3 Climate System Model

H.B. Gordon, L.D. Rotstayn, J.L. McGregor, M.R. Dix, E.A. Kowalczyk, S.P. O'Farrell, L.J. Waterman, A.C. Hirst, S.G. Wilson, M.A. Collier, I.G. Watterson, and T.I. Elliott.

CSIRO Atmospheric Research

National Library of Cataloguing-in-Publication Entry

The CSIRO Mk3 Climate System Model.

ISBN 0 643 06878 3.

1. Atmospheric circulation - Computer simulation. 2. Ocean circulation - Computer simulation. 3. Ocean-atmosphere interaction - Computer simulation. I. Gordon, Hal B.
II. CSIRO. Division of Atmospheric Research.
(Series : CSIRO Atmospheric Research technical paper (Online) ; 60).

551.524

Address and contact details:
CSIRO Atmospheric Research
Private Bag No. 1, Aspendale, Victoria, 3195 Australia
phone +61 3 9239 4400 Fax: +61 3 9239 4444

Email: chief@dar.csiro.au

CSIRO Atmospheric Research Technical Papers may be issued out of sequence.

Contents

Model development team

H.B. Gordon	(Hal.Gordon@dar.csiro.au)	: Coupled model, spectral AGCM, atmospheric convection
L.D. Rotstayn	(Leon.Rotstayn@dar.csiro.au)	: Cloud microphysics, code parallelization
J.L. McGergor	(John.McGregor@dar.csiro.au)	: SLT, PBL, vertical mixing
M.R. Dix	(Martin.Dix@dar.csiro.au)	: Radiation, gravity wave drag
E.A. Kowalczyk	(Eva.Kowalczyk@dar.csiro.au)	: Land surface model
S.P. O'Farrell	(Siobhan.OFarrell@dar.csiro.au)	: Sea-ice model
L.J. Waterman*	(ljw@uvic.ca)	: MOM2 implementation and development
A.C. Hirst	(Tony.Hirst@dar.csiro.au)	: Ocean model parameterizations
S.G. Wilson	(Stephen.Wilson@dar.csiro.au)	: Ocean model parameterizations
M.A. Collier	(Mark.Collier@dar.csiro.au)	: MOM2→3
I.G. Watterson	(Ian.Waterson@dar.csiro.au)	: Slab ocean model
T.I .Elliott	(Tracey.Elliott@dar.csiro.au)	: Code maintenance.

*Current affiliation: Earth and Ocean Sciences, University of Victoria, BC, Canada

1 Executive summary

The CSIRO Mk3 climate system model contains a comprehensive representation of the four major components of the climate system (atmosphere, land surface, oceans and sea-ice), and in its current form is as comprehensive as any of the global coupled models available worldwide. The documentation here represents a considerable team effort. A full history of the development path of the Mk3 model is provided, and it is noteworthy that the forerunners to this model (the Mk1 and Mk2 models) have been used in a large number of climate related experiments, and for multi-seasonal predictions. The major aim in the development of the Mk3 climate model has been to provide a coupled atmosphere-ocean system that gives a significantly improved representation of the current climate relative to the prior model generations. It was also highly desirable that this be achieved without the need for any artificial corrections (the so called “flux adjustments”) to the flux quantities connecting the atmospheric and oceanic systems. This has been successfully achieved with the Mk3 climate system model. The Mk3 model will be used to investigate the dynamical and physical processes controlling the climate system, for multi-seasonal predictions, and for investigations of natural climatic variability and climatic change.

This technical report is intended to provide a technical documentation for users of the Mk3 climate system model. There are details about the model computer code structure with specific reference to subroutine names and the operations undertaken by those routines. The model code is the representation of a very complex system of interacting components, and thus the information provided here will not cover all model details. Model code developed at CSIRO Atmospheric Research is however given in some detail. The Mk3 model contains an atmospheric model dynamical core that has been developed entirely in-house. The same applies to the land-surface (vegetation canopy) model and sea-ice model. There are a great number of physical processes that have to be incorporated (detailed in this report), and one significant development in the Mk3 model is the inclusion of a new prognostic cloud scheme. This allows the model to generate its own physically-based cloud properties, based upon cloud water and cloud ice. The cloud scheme has been coupled to an atmospheric convection scheme that is derived from that used in the Hadley Centre model. The oceanic model is based upon the GFDL MOM2 code, which has been specifically configured and developed to match the resolution of the atmospheric model. This approach was adopted so as to avoid the added complication of a “flux coupler” (which would be necessary with non-matching ocean-atmospheric grids). The ocean model also includes several important improvements to its physical parameterizations. The Mk3 coupled model has recently been used in a control run, and some details about the coupled model climatology are included.

2 Introduction and model history

The study of climate variability and climate change has progressed over the last decade from the use of relatively simple global models, consisting of atmospheric models coupled to slab ocean models (IPCC 1990), through to more realistic global coupled ocean-atmosphere-land-ice models (IPCC 1995). Global models of the climate system of the world are an important tool in climate research, and are probably the only way to investigate the highly non-linear interactions between the four major components of the climate system – the atmosphere, biosphere, oceans and sea-ice. Each of these components has responses on very different time scales. These time scales range from very short (days for synoptic weather patterns), to medium (seasonal for land surfaces), to long (multi-year for polar ice), to very long (decades/centuries for changes in vegetation types and distribution), to extremely long (centuries/millenia for changes in the deep oceans). The CSIRO "Mk3 Climate System Model" documented in this technical report is part of a development path towards a model that is able to allow for the interaction timescales of the above components. Each of the current components in the Mk3 climate system model is detailed in this report. The Mk3 model does contain a comprehensive representation of the four major components of the climate system, although some elements such as allowing for vegetation types to evolve, the "breathing biosphere", and ocean biogeochemistry are part of future developments. In its current form, the Mk3 model is as comprehensive as any of the global coupled models available worldwide.

The Mk3 model is being used to investigate the dynamical and physical processes controlling the climate system, for multi-seasonal predictions, and for investigations of natural climatic variability and climatic change. The model has been developed as a fully coupled ocean-atmosphere system, without the need for any adjustments of the interactive fluxes and component fields (for example, surface temperature) that couple the atmosphere to the oceans. The coupled model is in fact assembled from two major modules that are developed independently. These will be denoted as the AGCM (the Atmospheric General Circulation Model), which contains the atmospheric, land surface, and sea-ice components, and the OGCM (the Ocean General Circulation Model). These components can be used independently, provided that the appropriate boundary forcing fields are provided. Thus before the Mk3 coupled model is assembled, the separate AGCM and OGCM modules undergo extensive development and testing, and the documentation here represents the considerable efforts of a team of model developers.

The development path of the Mk3 model is now summarized. The initial development was centered around a spectral atmospheric model. The original CSIRO spectral AGCM had 2 vertical levels, and was developed at the Australian Numerical Meteorology Research Centre (Gordon 1981, 1983; Gordon and Hunt 1987; Hunt and Gordon 1988, 1989). From this model a 4-vertical-level model (CSIRO4) was developed at the CSIRO Division of Atmospheric Research (Gordon and Hunt 1991; Hunt and Gordon 1991; Smith and Gordon 1992). This model has been used for the simulation of the climate from 1950-1988 (Smith 1994, 1995) by the use of observed SSTs for that period. The 4-level model was also used in conjunction with a $50\ m$ deep slab ocean (with implied lateral heat transport by ocean currents). This latter model, although having coarse resolution, has been very useful in the study of climate change and climate variability - see Davies and Hunt (1994), Gordon and Hunt (1994), Moore and Gordon (1994), Syktus and Gordon (1994), Whetton et al. (1994), Hunt et al. (1995), Hunt and Davies (1997),

Hunt (1998), and Hunt (2000a). The 4-level model was also used in an early study of seasonal forecasting (Hunt et al. 1994).

The Mk1 AGCM

A 9-level AGCM model was subsequently developed from the 4-level model and the structure of the 9-level model is described in some detail by McGregor et al. (1993). This model retained the same thermodynamic ice model (based on Parkinson and Washington 1979) as used in the 4-level model. However, it had an improved land surface scheme allowing for 3 soil temperatures and a force restore method (Deardorff 1977) for soil moisture. It was also used in conjunction with a slab ocean model, and this model is now termed the "Mk1" version of the CSIRO climate model.

The Mk1 model has been used in a number of experiments. These include seasonal predictability (Dix and Hunt 1995) and equilibrium climate change (Watterson et al. 1995) experiments; for studies of climate change and variability see Suppiah (1994, 1995), Kidson and Watterson (1995), Watterson and Dix (1996), and Watterson (1997).

The Mk2 AGCM

The Mk1 model was subsequently enhanced in a number of ways, and this major upgrade of the model is referred to as the "Mk2" version. The major changes (non-ocean) were as follows:

a) The sea-ice model was replaced by one that contains both dynamics and thermodynamics (O'Farrell 1998), and also allows for fractional ice cover at a grid point (leads). The ice model is described in Section 19.
b) The land surface scheme was also given a major overhaul, and details of the replacement land surface scheme can be found in Kowalczyk et al. (1991, 1994). The essential parts of the Mk2 model land surface (soil-canopy) scheme are: (i) 12 vegetation types with part vegetation-part bare ground per grid point, (ii) separate energy and moisture flux calculations for vegetation and bare ground, (iii) rainwater and dew interception by vegetation, (iv) 3 soil types with a force-restore method (Deardorff 1977) for soil water for each soil type, (v) 3 levels of soil temperature (full implicit solution involving the surface temperature), and (vi) snow on vegetation/bare ground calculations.
c) The original atmospheric dynamical water vapour transport scheme (moisture held as a grid point field but horizontal transport calculated by the spectral method) was replaced by a SLT (Semi-Lagrangian Transport) method (McGregor 1993). The SLT method provides much more accurate transport for atmospheric variables that are highly spatially variable such as atmospheric water vapour. The SLT method is also essential for quantities that have negligible values at some grid points while adjacent points have significant values (such as cloud water). The latter is crucial for the subsequent development of the model to include cloud microphysics.

The Mk2 atmosphere-land-ice model was used in a number of experiments. These included the use of sea surface temperatures (SSTs) taken from observations (the Global Ice and Sea Surface Temperature (GISST) data set, Parker et al. 1995). These SSTs comprise of monthly mean values from 1871 to 1991. The Mk2 model had high horizontal resolution (1.875°) for these runs (Smith et al. 1998, Smith 1999). The Mk2 model has also been used in seasonal prediction experiments (Hunt 1997, 2000b).

Mk2 + slab ocean model

The inclusion of a slab ocean model ($50\ m$ deep) allowed the Mk2 model to be used in a number of climate variability and equilibrium climate change studies: for climate variability see Kidson and Watterson (1999), Sinclair and Watterson (1999), and Watterson (2000), and for equilibrium climate change see Whetton et al. (1996), Smith et al. (1997), Watterson et al. (1997), and Watterson (1998). There was also an interesting analysis of the reasons for the moderately high equilibrium $2xCO_2$ warming attained in the Mk2 simulations compared to the low magnitude of warming in the BMRC model (Watterson et al. 1999).

Mk2 coupled to ocean GCM

With a view to creating a fully coupled ocean-atmosphere model suitable for climate change and climate variability work, the GFDL ocean model of Cox (1984) was obtained and implemented at a resolution suitable for the Mk2 AGCM. The models were utilized at a modest horizontal resolution ($5.625° \times 3.1°$) with matching land-sea masks. The horizontal resolution was essentially dictated by the computing facilities available at the time, considering that multi-century runs were required for climate change work. In order to minimize climate drift, the method of flux adjustments (Sausen et al. 1988) was employed. This model was successfully used in a transient climate change experiment to 2xCO2, and is described in some detail in Gordon and O'Farrell (1997). This coupled model was very successful in that it had only a minor amount of initial climate drift.

The Mk2 coupled model and its responses under greenhouse change have been analyzed in a variety of ways. The model responses under an imposed freshening in the North Atlantic (simulating a sudden influx of freshwater forming a surface lens) yielded valuable information about the feedbacks between the ocean and the atmosphere (Cai et al. 1997). The behaviour of the coupled model at high latitudes investigated, and the presence of an Antarctic Circumpolar Wave was detected in the model (Cai et al. 1999). The coupled Mk2 model was also analyzed for changes in climate and climate variability under enhanced levels of CO_2 up to three times the current CO_2 amount (Gordon and O'Farrell 1997; Dix and Hunt 1998; Cai and Gordon 1999; Yonetani and Gordon 2001a,b).

Mk2 + (ocean model with GM eddy mixing)

The Mk2 coupled model control run (Gordon and O'Farrell 1997) displayed a minor amount of climate drift. In a three century control run, the global mean surface air temperature decreased by 0.4, 0.12, $0.09°C$ for each successive century. The reasons for the drift in this (flux adjusted) model were investigated (Cai and Gordon 1999; Hirst et al. 2000), and a large part of the cause concerned changes in oceanic convection at high latitudes, and changes in the associated ocean-atmosphere heat fluxes. The ocean model in the Mk2 coupled model was enhanced by the inclusion of the Gent and McWilliams (1990) scheme for adiabatic transport of heat and other water properties by mesoscale eddies, hereafter denoted by "GM". The GM scheme was first implemented into a stand-alone ocean model and tested at length (Hirst and McDougall 1996; England and Hirst 1997; Hirst and McDougall 1998). The addition of the GM scheme had several desirable outcomes, one of which was to markedly reduce the amount of high-latitude convective overturning in the high-latitude Southern Ocean, and to reduce the magnitude of the (implied) surface atmosphere-ocean heat fluxes in that region. As a result, the flux adjustments required at high Southern latitudes in coupled mode were reduced (Hirst et al. 2000). When this

GM enhanced ocean model was subsequently coupled to the Mk2 AGCM, the climate drift that was experienced before was almost entirely eliminated (Hirst et al. 1996, 2000).

The Mk2-GM model proved to have very long term climate stability, and has been used in a 1,000 year control integration (Hunt 2001; Cai et al. 1999; Walland et al. 2000; Vimont et al. 2001, 2002). There has been a subsequent 10,000-year integration that is currently being analyzed, but to date has revealed that parts of the globe may be affected occasionally by droughts that last for many decades (Hunt and Elliott 2002). It has also been used extensively in climate change related experiments (Hirst et al. 1996; Hirst 1999; Matear and Hirst 1999; Cai and Whetton 2000; Jackett et al. 2000; Matear et al. 2001; Bi et al. 2001). The stability of the coupled model and the realistic sea-ice behaviour also allowed for an extensive examination of issues related to Antarctica under greenhouse warming (O'Farrell et al. 1997; Connolley and O'Farrell 1998; O'Farrell and Connolley 1998).

International intercomparisons

The Mk1 and Mk2 model versions have taken part in the international intercomparisons of models - PCMDI (Program for Climate Model Diagnosis and Intercomparison) which has a web site http://www-pcmdi.llnl.gov . The Mk1 and Mk2 *atmospheric* models have taken part in AMIP (Atmospheric Model Intercomparison Project), parts 1 and 2. The Mk2 *coupled* model has taken part in CMIP (Coupled Model Intercomparison Project), parts 1 and 2. To take part in both AMIP and CMIP, data have to be supplied from model control runs and transient CO_2 increase model runs. The data are then used in sub-projects that assess the performance of models for a particular climatically important feature (for example, monsoon behaviour or ENSO behaviour). The PCMDI web site above has a full list of publications arising from these experiments. The CSIRO models have compared well in the PCMDI sub-projects. Some examples of AMIP publications are Gleckler et al. (1995), Slingo et al. (1996) and Zhang et al. (1997), while CMIP publications include Barnett (1999), Covey et al. (2000) and Lambert and Boer (2001).

Recognizing the importance of clouds and radiation, and the role that they play in governing climatic change, there have been a number of investigations into this aspect of the CSIRO climate models (Mk1, Mk2 etc) and intercomparisons made with other international climate models and with observations: see Garratt (1993); Garratt et al. (1993); Garratt (1994,1995); Garratt and Prata (1996); Garratt et al. (1998, 1999); and Garratt (2001). The Mk2 model also took part in the FANGIO (Feedback Analysis for GCM Intercomparison and Observations) project, which was concerned with an evaluation of differences in cloud-radiation feedbacks between models (Cess et al. 1996, 1997). There has been participation in similar investigations about the performance of the land surface schemes, for example Pitman et al. (1993) and Chen et al. (1997).

The Mk3 model version

The next stage in the evolution of the CSIRO climate system model is termed the "Mk3" model. This Technical Report provides a description of the Mk3 model, with particular emphasis on the aspects changed since the Mk1/Mk2 model versions. The Mk2 coupled model proved to be capable of undertaking climate runs of many thousands of years. However, significant climate drift in the model was prevented by the use of flux adjustments (Gordon and O'Farrell 1997). Such flux adjustments are unphysical, and it is most desirable to eliminate their use in coupled

models. Thus the aim with the current version of the model (Mk3) was to develop the model to a stage where minimal or no flux adjustments would be needed in coupled model runs. Thus various aspects of the model have been improved (especially physical parameterizations), and there has been a substantial increase in the resolution of the model (see next section). The end result of several years of development work on the Mk3 model is that it has been successfully run in coupled mode without flux adjustments, and with only a modest amount of climate drift.

The *current* stage (July 2002) of the Mk3 model development path is described in this report. In the following section (3) is a description of the structure of the Mk3 coupled model. The coupled model consists of an extensively upgraded AGCM (relative to Mk2), coupled to the GFDL MOM2 Ocean Model (which also required considerable implementation/development work at the requisite Mk3 resolution). The horizontal and vertical structure of the model components and the resolutions available are given in Section 3.

The Atmospheric Model and Land Surface Model are detailed in Sections 4-18. Section 4 is concerned with the atmospheric model structure, and gives an outline of enhancements since the description given in the Technical Report on the Mk1 atmospheric model (McGregor et al. 1993). A large part of the recent development of the atmospheric model centers around the use of the highly accurate tracer transport delivered by the Semi-Lagrangian method. This has been applied to atmospheric moisture vapour transport, and also cloud water and cloud ice. This is described in Section 5. The land surface scheme in the model (Section 9) has also been substantially revised, and now includes more extensive soil and vegetation types. There is also a multi-layer snow cover scheme included in this component. Another major upgrade of the atmospheric physics, and one very much concerned with the application of this model to climate change, is the inclusion of a prognostic cloud scheme. This allows the model to generate its own physically based cloud properties, based upon cloud water and cloud ice, and this scheme is described in Section 13.

The Sea-ice Model is described in Section 19. The Mk1 model used a simple 1-layer thermodynamic ice model based largely on Parkinson and Washington (1979). This was replaced in the Mk2 model by a multi-layer thermodynamic and dynamic ice model (O'Farrell 1998). The same ice model is used in the Mk3 model with some minor changes in coding and specification of some parameters.

The ocean component of the Mk2 model was based on the GFDL Cox (1984) code. In the Mk3 model the ocean component has been upgraded to the GFDL MOM2.2 code (Section 20). This has been specifically designed to match the horizontal land-sea grid of the Mk3 AGCM .

In Sections 21 and 22 the coupled version of the Mk3 model and some brief aspects of its climatology are presented. Finally, in Section 23, results from a transient CO_2 increase run are described.

3 Coupled model structure

An outline of the current model structure is now given. This sets out the model resolution, and also some details on what model configurations are available. As mentioned above, the AGCM has been developed as a unified package containing an atmospheric model, a land surface model, and the ice model. They are not able to be run independently, although a "single column model"

of the atmospheric model physical parameterizations is available. In the description of the AGCM and OGCM to follow, the horizontal grids used in the models are based around the "Gaussian" latitudes used in spectral models. These latitudes are not evenly spaced in the north-south (meridional) direction, although they are approximately so. Thus the meridional spacing quoted below will be approximate only. However, the longitudinal (east-west) spacing is regular.

3.1 AGCM

The Mk3 AGCM has been developed specifically to use horizontal spectral resolution T63 (1.875°EW x 1.875°NS) with 18 vertical levels. This is also the AGCM resolution for the coupled Mk3 model. However, in research mode, the AGCM can also be run at horizontal spectral resolution R21 (5.625°EW x 3.1°NS). The spectral R42 resolution is also available, but is not now frequently used. The vertical resolution (nominally 18 levels) has research mode variations of 9 and 24 levels available. It is to be noted that the spectral model now contains a Semi-Lagarangian Transport (SLT) method for the moisture components (see Section 5 below). The number of grid boxes in the horizontal for the Mk3 AGCM (nominally T63) is thus 18,432. This is a substantial increase on the number of horizontal grid boxes (3,584) as used in the Mk2 model. There are also twice as many vertical levels (18 instead of 9) in the Mk3 AGCM relative to Mk2.

3.2 OGCM

The ocean component for the Mk3 model has been developed with the specific aim of forming the coupled model with an atmospheric resolution of T63. However, the ocean model resolution is enhanced (relative to the AGCM) in the meridional direction in order that an adequate representation of the highly important El Niño features be obtained. The meridional resolution of the OGCM has thus been set at double that of the AGCM. The resolution is thus 1.875°EW x 0.9375°NS (sometimes referred to as "T63_2" resolution). This means that, horizontally, there are two ocean grid boxes to each atmospheric grid box in a coupled configuration. There are 31 vertical levels in the Mk3 ocean model.

The current version of the coupled Mk3 model can only be run at a resolution of T63 (AGCM) and T63_2 (OGCM). In addition, the AGCM can be run with a "slab" ocean model.

3.3 Computational considerations

Considerable effort has been expended on generating computer code that can be run on a variety of computer platforms. These currently include Cray, NEC, Fujitsu and Silicon Graphics computers. The Mk3 computer coding allows for parallel processing in both the AGCM (Rotstayn and Dix 1992) and OGCM components. The code is now in a highly vectorized form, and efficiency has, in some cases, been gained at the expense of clarity in the code. For example, in the atmospheric code, pairs of latitude rows of grid points (one row from the Northern Hemisphere (NH) and the equivalent row from the Southern Hemisphere (SH)) are joined together thereby doubling the vector length. In future developments, further gains in vector length efficiency will be obtained by processing several latitude rows (north + south) together.

4 The atmospheric model structure

The dynamical framework of the atmospheric model is based upon the spectral method (Bourke 1974), with the equations cast in the flux form that conserves predicted variables (Gordon 1981). Note that the atmospheric dynamical equations are detailed in Appendix B. An important model development concerns the treatment of atmospheric moisture within the Mk3 model. The earlier method entailed having the atmospheric water vapour carried as a grid field with only the advection of the vapour being computed by the spectral method. This has now been replaced by the SLT method (see Section 5). Some other features of the Mk3 atmospheric dynamical core are as follows.

4.1 Hybrid vertical coordinate

The vertical coordinate of the model was originally a σ-coordinate system, where $\sigma = p / p_s$, with p being the vertical pressure and p_s the surface pressure. This vertical coordinate of the model has now been replaced by a hybrid ($\sigma : p$) vertical coordinate. A full description of the implementation of the hybrid vertical coordinate in the AGCM is given in Rautenbach (1999). The hybrid vertical coordinate is denoted as the η-coordinate. In this system, the Earth's surface forms the first coordinate surface (identical to the σ-system), while the remaining vertical coordinate surfaces gradually revert with altitude to isobaric levels. Details about casting the atmospheric model equations in terms of the hybrid vertical coordinate are given in Appendix B.

4.2 Virtual temperature

The model dynamical equations are also configured to include the use of virtual temperature (T_v) rather than temperature (T). This allows for the effects of moisture loading being included in the equations, and the modifications in the equations are to the terms that link the momentum equation to the thermodynamic equation. Details of this are also given in Appendix B, and are also in terms of the above hybrid vertical coordinate.

4.3 Temperature variable

In the original spectral model formulation, the temperature variable was given by $T' = (T - \overline{T})$ where $\overline{T}$ is an isothermal mean temperature (290 K). The temperature variable in the current model has been replaced by one that contains a pressure dependency. This ensures that the cancellation of large terms in the pressure gradient part of the momentum equation is minimized. Details of the formulation (following Simmons and Chen 1990) are given Appendix B, subsection 26.3.

4.4 Surface elevation – reducing the Gibbs effect

The earth's surface elevation in a standard spectral model has to be fitted to the resolution of the spectral model. This can lead, even at the moderately high resolution of T63, to areas of significant negative elevation. For example this can happen at sea points adjacent to the Andes, and is known as the Gibbs phenomenon. (See, for example, Hoskins 1980). In the current Mk3 model this matter has been rectified, to a large degree, by the use of a special adaptation of the surface elevation. In this method the spectral topography is iteratively adapted, by allowing the

fitted topography to adjust (or flex) more in some locations (say mountainous regions) than in other locations (over the oceans). This method is described in Holzer (1996), and the computer program for implementing this method was kindly supplied by the author.

It is a non-trivial task to implement this method, and requires some manual interaction to determine which areas can flex more than others, while still retaining a topography that is very similar to the raw data. The land-sea mask in areas such as along the coast of the Andes may have to be adjusted (slightly) to allow for optimum fitting of the spectral topography. At a resolution of T63, this entails changes from sea points to land points at a very small number of locations.

4.5 Atmospheric model vertical structure

In the description of the AGCM a standard notation is used for variables wherever possible, and a listing of all variables is given in Appendix A. The main spectral prognostic variables of the model are the surface pressure (p_s), and the surface pressure weighted divergence ($\hat{D}$), vorticity ($\hat{\xi}$), and temperature ($\hat{T}$). The prognostic equations for these are derived in Appendix B. The derivation follows Gordon (1981), with the addition of a hybrid vertical coordinate and the Simmons and Chen (1990) treatment of the temperature variable. The specific prognostic equations as used in the Mk3 model are located in Appendix B as follows: The p_s prognostic – Equ. (26.8), the $\hat{T}$ prognostic – Equ. (26.28), the $\hat{\xi}$ prognostic – Equ. (26.46), and the $\hat{D}$ prognostic – Equ. (26.47). The divergence and vorticity have an associated velocity potential ($\hat{\chi}$) and streamfunction ($\hat{\psi}$), which are defined by $\hat{D} = \nabla^2(\hat{\chi})$ and $\hat{\xi} = \nabla^2(\hat{\psi})$. The spectral variables are carried as spectral (complex or split real/imaginary) fields except for moisture (q), which is a grid variable. The main prognostic variables are carried at full-levels, whilst the diagnostics of "vertical" velocity ($\dot{\eta}$) and geopotential height are essentially derived at half-levels as defined by pressure; the full-levels are located midway between the half-levels. The atmospheric water vapour, cloud liquid and frozen water are advected by the SLT method (see Section 5) and are held as model grid point fields only.

The vertical half-levels of the model are defined by a smoothly-varying cubic formula

$$\eta_{k+0.5} = (1 + 2k / NL)(1 - k / NL)^2 \qquad 0 \le k \le NL \qquad 4.1$$

where NL is the number of model levels. This formula is symmetrical about $\eta = 0.5$ and provides $\eta_{0.5} = 1$ and $\eta_{NL+0.5} = 0$. The model full levels are given by $\eta_k = (\eta_{k-0.5} + \eta_{k+0.5})/2$. Choosing a smooth variation for the spacing of the levels reduces truncation errors in the vertical advection part of the SLT scheme. The pressure at a given level η_k is determined by $p_k = A_k P_{00} + B_k p_s$ (see Appendix B). The 18 level Mk3 AGCM model full level η_k values and corresponding A_k and B_k are given in Table 1. These values are generated in the model in subroutine "*vertc*". Table 1 also shows the approximate height of each model level (based upon global annual mean geopotential heights in the model).

Model level k	η_k	A_k	B_k	Approx. level height (m)
18	0.0045	0.00446	0.0	36355
17	0.0216	0.02160	0.0	27360
16	0.0542	0.05380	0.00038	20600
15	0.1001	0.09719	0.00295	16550
14	0.1574	0.14574	0.01167	13650
13	0.2239	0.19160	0.03233	11360
12	0.2977	0.22680	0.07086	9440
11	0.3765	0.24528	0.13126	7780
10	0.4585	0.24456	0.21394	6335
9	0.5415	0.22616	0.31534	5070
8	0.6235	0.19478	0.42867	3970
7	0.7023	0.15660	0.54573	3025
6	0.7761	0.11743	0.65863	2215
5	0.8426	0.08150	0.76109	1535
4	0.8999	0.05116	0.84870	990
3	0.9458	0.02745	0.91837	575
2	0.9784	0.01091	0.96749	300
1	0.9955	0.00225	0.99329	165

Table 1. Hybrid level structure of the Mk3 AGCM and approximate level heights.

4.6 FFT and model timestep

The atmospheric model has been coded for variable spectral (horizontal) resolution, and the most appropriate resolutions are usually based upon the number of east-west grid-points being some power of 2. This enables an efficient usage of currently available Fast Fourier Transform routines (FFTs). (See Section 3.1 for current Mk3 AGCM model resolutions). A semi-implicit leapfrog time scheme is used (current and previous timestep values are retained) together with a Robert (1966) time filter (which is sometimes referred to as the Asselin filter). The T63 model timestep is 15 minutes.

4.7 Model flow diagram

The sequence of operations during each timestep of the AGCM is illustrated in Fig. 1, in which some subroutine names have been included as a guide for model users. A more complete list of subroutine names is given in Appendix C. The atmospheric model as presented here has been coded for use with a coupled ocean model, and details are also given in Appendix C. The atmospheric part of the combined model is controlled by the master routine *main*. This routine controls the initialization of the model (the main model constants are set in *inital* and *initax*, the atmospheric restart file is read via *filerd*, various other input files are read via *datard*, and the Gaussian latitudes and Legendre polynomials are created in *gauleg*). There then follows a sequence of subroutine calls which takes the model through repeated timesteps - the Timestep loop.

The major components involved in each timestep are as follows. From the spectral input data for the streamfunction and velocity potential, the spectral fields for U and V are obtained (*uvharm*). At the same time, the spectral equivalents for $\partial U_{fr}/\partial t$, $\partial V_{fr}/\partial t$ (which are the frictional dissipation terms from the previous timestep) are also created. These components will be used to determine the frictional heating of the atmosphere arising from the frictional dissipation. This particular part of the model physics is discussed more fully in Section 15.

The model then enters the Physics transform loop. Noting that the main prognostic variables of the model ($\hat{\chi}, \hat{\psi}, \hat{T}, p_s, q$) have just been updated via the previous time integration (or the equivalent fields read from the restart file), the temperature and moisture fields (vapour and cloud liquid and frozen water) in particular then need to be adjusted for the physical parameterizations of rainfall, convection and vertical mixing. There will also be implied adjustments to the momentum fields via surface drag, turbulent mixing and gravity wave drag. All of the physical parameterizations (see Sections 7-14) are achieved during the Physics loop, which transforms spectral data to equivalent grid-point fields in order to perform these adjustments. More details of the methodology used in the Physics transform loop, and a subsequent Dynamics transform loop, are given in the next sub-section entitled *Grid transforms*.

The next part of the timestep evaluates the non-linear part of the tendencies for the $\hat{\chi}, \hat{\psi}$ and $\hat{T}$ fields. This is achieved in the Dynamics loop (Section 16) which, like the Physics loop, takes spectral fields and creates grid-point equivalents. The grid-point values are used to determine multiple products on the grid, and by an inverse transform, the relevant spectral tendencies are evaluated. This is the standard spectral technique for such evaluations.

Following the Physics and Dynamics transform loops (Fig. 1), the $\nabla^2 \hat{E}$ (see Appendix B) term of the divergence tendency equation is added (spectrally in the form $-l(l+1)\hat{E}_l^m / a^2$) to the non-linear divergence component derived during the Dynamics loop (subroutine *linear*). In order to prevent decoupling of the time integrated solution at odd and even timesteps, a Robert (1966) time filter is used (see Section 17). This filter is applied in two parts - the first stage being during the time integration (*semii*) and a subsequent part is applied following the physical adjustments (in *assel* on the flow diagram), but before the next timestep.

The time integration of the main atmospheric spectral prognostic variables is then performed (*semii*). The spectral vorticity equation (or the stream function equivalent) is integrated in a simple leapfrog manner. In the case of the spectral divergence, temperature, and surface pressure equations, a semi-implicit time integration method is used in order to handle gravity waves; see Gordon (1981) and McGregor et al. (1993) for details. Following the time integration, the spectral horizontal diffusion (*diffn*) for the temperature, vorticity and divergence fields is applied in a forward implicit manner for numerical stability (see Section 18).

The atmospheric water vapour and cloud liquid water and cloud ice are advected using a SLT method (*jmcgslt*) – see Section 5 for details. A leapfrog time integration method with a time filter is used here as well. The sea-ice model contains not only thermodynamics (computed during the Physics loop using routines *surfupl* and *seaice*), but also ice dynamics. The advection of ice is controlled by the routine *icedrive*. This completes a model timestep of the AGCM.

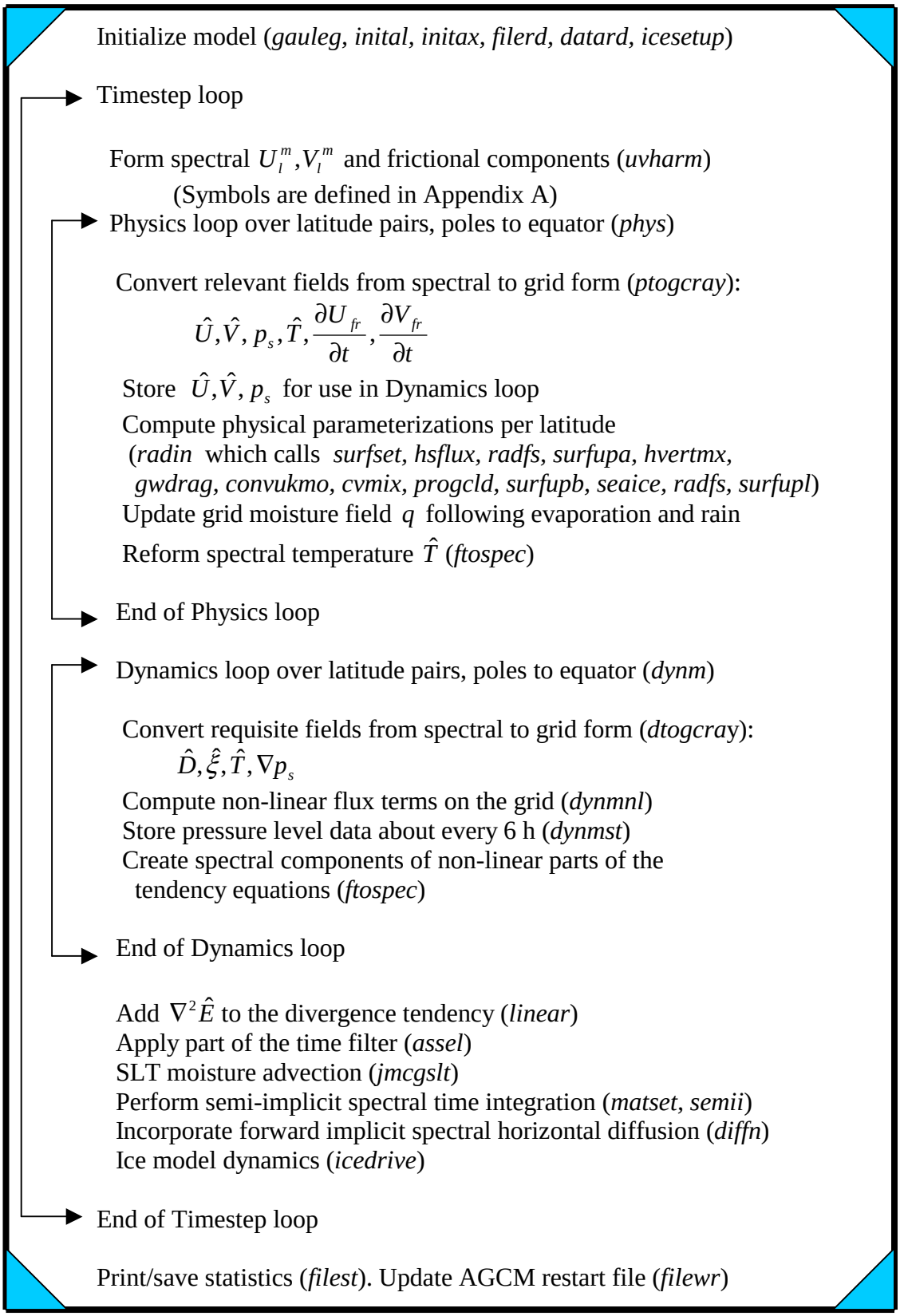

Figure 1. Mk3 AGCM flow diagram. Key subroutine names are given in italics.

4.8 Grid transforms

For each timestep, the atmospheric model uses two grid transforms. The first is termed the Physics transform loop during which various physical parameterizations are implemented. A second grid transform termed the Dynamics loop follows, in which the non-linear dynamical tendencies are evaluated. Both transform loops are parallel processed over latitude bands.

The temperature field will be used as an example to demonstrate the method used in the two grid transforms. During the Physics loop, the temperature is transformed from spectral space (following time integration) into its gridded form. This is achieved in a sequential manner - first the northern-most plus the southern-most latitude, and so on up to the adjacent equatorial latitudes. The temperature field is modified by the physical processes (e.g. heating, convection, vertical mixing), and the new spectral field is generated by an inverse transform technique. This new field is then exactly fitted to the spectral resolution of the model.

The updated temperature field is now in a form suitable for application of the horizontal flux calculations (the Dynamics transform) for evaluation of the non-linear part of the temperature tendencies. This again involves a full spectral-to-grid, and subsequent grid-to-spectral transform as in the Physics loop. The use of two transform loops ensures that a spectrally-fitted temperature field is used during the calculation of advective tendencies on the grid. There is only a small computational overhead associated with the second transform loop for temperature.

The transform from complex spectral space to values on the grid is performed by routines that are appropriate to vector processing or scalar processing computers (*ptogcray*/*dtogcray* or *ptog*/*dtog* respectively) for the Physics and Dynamics loops. The complex fields are held as separate real and imaginary components. The Fourier coefficients for a NH latitude and equivalent SH latitude can be obtained at the same time by summing separately the odd and even components (for both real and imaginary parts) for the Legendre part of the transform. This is due to the fact that

$$P_l^m\{\sin(-\phi)\} = (-1)^{l+m} P_l^m\{\sin(\phi)\} \qquad 4.2$$

where $P_l^m\{\sin(\phi)\}$ is an associated Legendre polynomial of the first kind normalized to unity. The resultant odd and even sums can be either added or subtracted to give Fourier components for the NH or SH. The FFT routines then generate grid values at the latitude.

The inverse transform, whereby a spectral field is re-synthesized from the data on the grid at every latitude, is essentially the reverse of the above. The same efficient odd/even, real/imaginary method is used. This part of the Mk2/3 code has been reformulated (for parallel processing computers) relative to the original Mk1 method. The grid point field for a particular latitude row is used to generate the Fourier coefficients. By using both north + south latitude rows, the odd and even, real and imaginary components are saved *per latitude band*. At the end of processing all latitude bands, the inverse transform is completed by combining all latitude bands with the appropriate Legendre polynomials (*ftospec*). The latter routine can be utilized in an efficient parallel-processing manner.

In the outline of the grid transforms above, it should be noted that the Mk3 model has been coded in Fortran specifically for high speed on vector computers such as a Cray or NEC. There

are alternative routines provided which are better suited to scalar machines (for example *physseca + ptog* and *dynmseca + dtog*). The coding also provides subroutines that use FFT routines for appropriate machines (the *mfftg* and *mfftm* type routines). The FFT vector processing routines perform most efficiently when as many variables as possible are transformed (per latitude row) at the same time.

5 Semi-Lagrangian moisture transport (*jmcgslt*)

The moisture variables (vapour q_V, cloud liquid water q_L and cloud ice q_I) are held as grid point variables and are advected in the Mk3 model by means of SLT method. The model is also coded so that tracers can be advected by the SLT routines. The advection equation (for moisture or tracers denoted by q) is given by

$$\frac{dq}{dt} = 0 . \qquad 5.1$$

This is solved in a split manner, by successively solving for vertical advection

$$\frac{d_V q}{dt} \equiv \frac{\partial q}{\partial t} + \dot{\eta}\frac{\partial q}{\partial \eta} = 0 \qquad 5.2$$

and then horizontal advection

$$\frac{d_H q}{dt} \equiv \frac{\partial q}{\partial t} + u\frac{\partial q}{\partial x} + v\frac{\partial q}{\partial y} = 0 . \qquad 5.3$$

In the following, an air parcel located at a grid point at the end of a time step (or the end of a split time step) has its departure point at the beginning of an advection time step denoted by *, where this same symbol is used for the separate processes of vertical and horizontal advection. The departure point is obtained by interpolation (see below).

The vertical advection is achieved by first determining the vertical departure points (*vadvect*) and then interpolating to find the value of q at the departure points (*vinterp*). Both of these routines are coded for parallel processing over latitudes (longitude-vertical slices). To better handle the typical sharp decrease of water mixing ratio in the vertical, (5.2) is solved in terms of the cube root of moisture $J = q^{1/3}$. (If the quantity is not moisture vapour, then $J = q$ in the following). The vertical advection is achieved by solving the equivalent equation

$$\frac{d_V J}{dt} = 0 \qquad 5.4$$

giving

$$J'' = J(\tau - 1)^* \qquad 5.5$$

where J'' is the intermediate value following vertical advection (using a leapfrog timestep) from the departure points denoted by the *. The vertical interpolations in (5.5) are performed using Akima (1970) cubic interpolation. The symbol (τ) is used here to denote values at the current timestep, while ($\tau - 1$) and ($\tau + 1$) are used to denote values at the previous and next timestep.

The resulting values (obtained from $q'' = (J'')^3$ if moisture vapour, else $q'' = J''$) are provided to the horizontal advection routine, which uses the D3 scheme for departure points in the semi-Lagrangian procedure described by McGregor (1993). The routine that handles the horizontal advection (*jmcghor*) is also coded for parallel processing. In this case the parallel processing is over the vertical levels (latitude-longitude slices). The horizontal advection is achieved by first determining the departure points (*hadvect*) and then interpolating horizontally to find the value of q'' at the departure points (*hinterp*). The updated mixing ratios after horizontal advection are then given by

$$q(\tau + 1) = (q'')^*. \qquad 5.6$$

Lagrange bicubic interpolation is used for finding the departure point values of q'' (denoted by $(q'')^*$) in (5.6).

The final moisture/tracer values after the advection leapfrog timestep, $q(\tau + 1)$, are compared with those before advection, $q(\tau - 1)$, to ensure that the global integral is conserved. For this purpose a global *a posteriori* fixer is applied; the fixer also removes any negative moisture/tracer values created during advection. The names of the fixer routines are *enforce_conq* and *enforce_cont* (for moisture variables and tracers respectively, each having different three-dimensional array structures within the model). These routines are also parallel processed as horizontal slices.

6 Interface to the physical processes (*phys*, *radin*)

Most of the atmospheric model computational burden is associated with the Physics transform loop (radiation and convection in particular). Because of their complexity each major component of the parameterizations for the atmosphere, land surface, and sea-ice is described in separate sections of this report.

For each latitude row certain grid-point values are evaluated from spectral space (subroutine *ptogcray*). These include $\hat{U}, \hat{V}$, p_s and $\hat{T}$. The momentum tendencies due to the horizontal diffusion of momentum are also obtained. The water vapour mixing ratio q_V is already available in grid form. In addition, the Mk3 model employs cloud microphysics (see Section 13), which has cloud liquid water q_L and cloud frozen water (ice) q_I as grid point prognostic variables. The values of $\hat{U}, \hat{V}$, p_s are not altered by the Physics loop and are retained in grid form for the Dynamics loop.

An important physical parameterization calculates the turbulent vertical mixing of momentum, which includes the effect of surface stresses. Special consideration is required in a spectral model, because the implied changes to the velocities would require the re-synthesis of the associated spectral vorticity and divergence fields. To improve computational stability these

tendencies must be either calculated implicitly (similar to the procedure the model uses for temperature and moisture), or backward in time. By taking the latter course, we can apply the vertical mixing tendencies as a grid-point addition to the non-linear dynamics terms, and avoid this re-synthesis. It is necessary that these quantities be saved between timesteps.

7 Surface characteristics (*surfset, hsflux, surfupa, surfupb*)

The distribution of land and non-land T63 model grid-points is shown in Fig. 2. The spectral method requires that the surface topography be spectrally fitted to a resolution of T63 for use by the model. The initial topography is derived from a (1° x 1°) data set, area averaged to the model Gaussian grid (192 x 96 grid points at T63). The Mk3 model dynamical core (see Appendix B) uses a special technique that relies upon a prescribed (time invariant) surface pressure field P_{sr}, which is designed to minimize cancellation of large terms in the momentum equation. The P_{sr} field is directly determined by the surface topography, and may be spectrally synthesized at T63 resolution. A consequence of this procedure is non-zero sea elevations due to the Gibbs phenomenon. In order to minimize the Gibbs phenomenon, the "Optimal spectral topography" method described by Holzer (1996) has been used in the generation of the spectral form of P_{sr} (see also Section 4 "Atmospheric Model" above). The resultant topography is shown in Fig. 3.

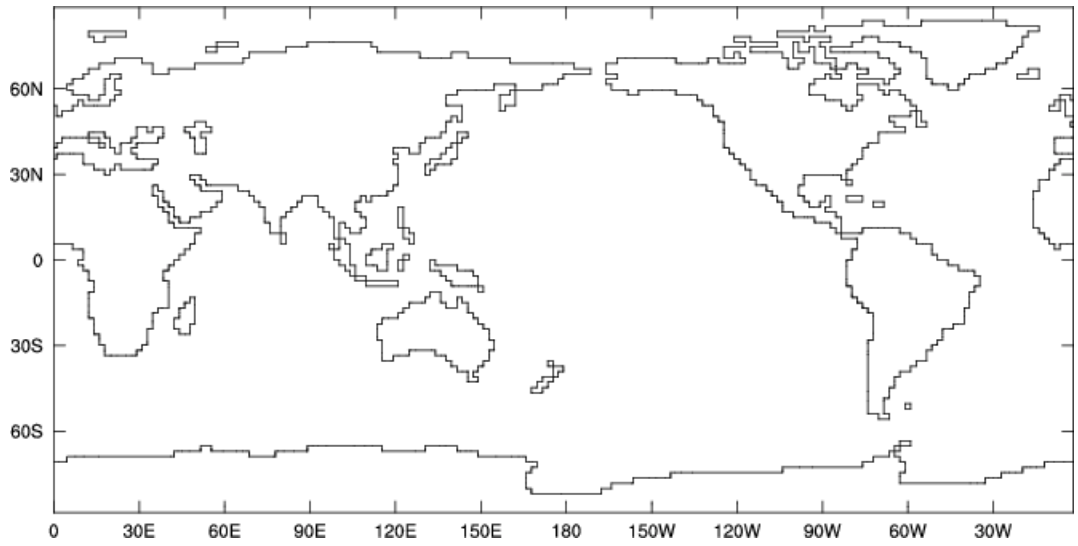

Figure 2. Land mass outline on the T63 model grid (192 x 96 points).

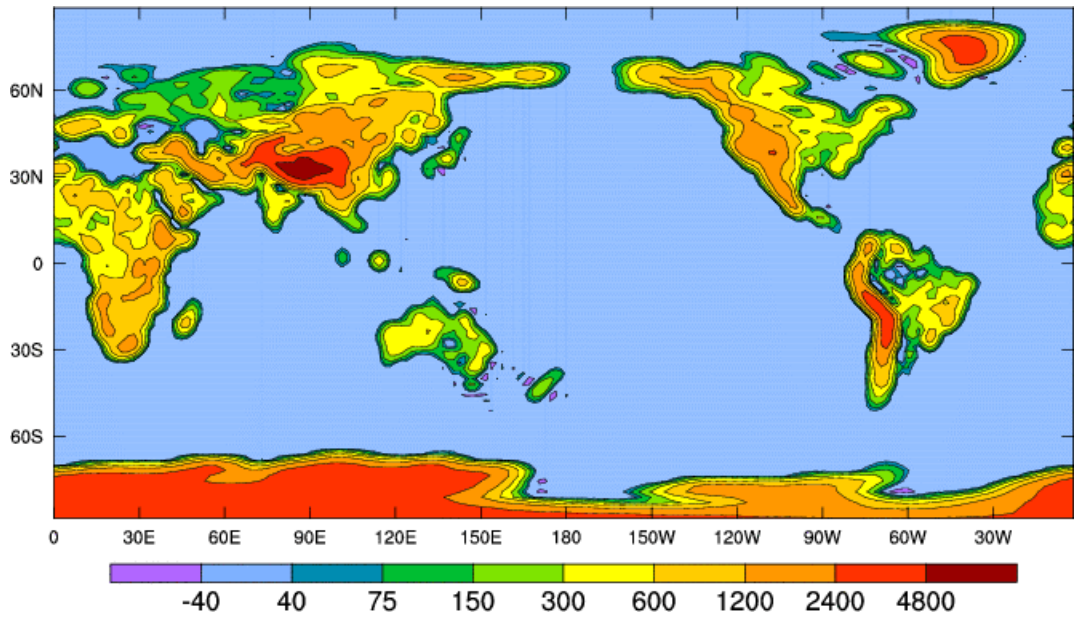

Figure 3. Topography (*m*) on the T63 model grid.

There are four types of surface. These are referenced by a mask ("imsl"), which has integer values 1 for Ice, 2 for Mixed-Layer Ocean (MLO), 3 for Sea, and 4 for Land. This is not a static mask since the model allows for the growth and decay of ice (see the description of sea grid-points below).

7.1 Land

In the Mk3 model, all land grid-points have predetermined properties. These form part of the land surface/vegetation model as described in Section 9. The land properties include seasonally varying albedos, roughness length, and stomatal resistance. There are also constant values for leaf area index, vegetation type and soil type. Soil temperatures and soil moistures are computed for land grid-points, as is snow cover. The surface roughness length (modified for the presence of snow) is used in the determination of the surface fluxes as described in Section 8. Some additional details regarding the surface albedo are given in Section 12 for radiation.

If the atmospheric conditions are sufficiently cold, then precipitation falling on the surface will be snow. This snow alters the properties of the surface according to the depth of snow. The maximum allowable snow depth is set at $0.4\ m$ water equivalent with excess being assumed to be converted to underlying ice (glaciers) with assumed eventual (but in modelling terms immediate) removal to the oceans as a runoff term.

7.2 Sea grid-points

In uncoupled mode, the sea surface has its temperature (T_s) interpolated daily from specified monthly data, and there is no allowance for diurnal variation of sea surface temperature. Near the poles, the sea grid-points may be converted to mixed-layer ocean grid-points with self-computed temperatures, and then to ice grid-points.

Due to the presence of non-zero elevation for sea grid-points, the atmospheric temperature and moisture fields will tend to adjust to this elevation effect. The use of observed sea-level (elevation = 0) temperatures will give rise to incorrect gradients between the surface and the first model level, which are used in the calculation of surface fluxes. In order to correct for this, the SSTs are adjusted to account for the spectral elevations by use of a constant lapse rate of $6.5°C\ km^{-1}$. These adjusted SSTs are then used in the calculation of sensible and latent heat flux.

7.3 Sea-ice grid-points

Sea-ice is formed if the temperature of the ocean (or a mixed-layer point) falls below the freezing point of sea water. The generation of sea-ice is controlled by the sea-ice model, which is described in Section 19. Ice may also be advected over adjacent sea points. The sea-ice model also allows for variable snow cover on the ice. The temperature at the air-surface interface T_s (either ice or snow) is computed as a result of the net flux of energy (from radiation, sensible heat flux, heat of sublimation and heat conduction through the ice) into the surface layer. Sublimation reduces the snow cover at grid-points with snow, and the ice amount at snow-free ice grid-points.

For a description of how ice changes its horizontal extent, see the next subsection detailing the function of the mixed-layer ocean grid-points. (Note that mixed-layer points only exist in uncoupled mode.) Some constraints imposed on the sea-ice are:
i) the maximum snow depth is 2 *m* with the excess being compressed into ice below the snow
ii) a maximum ice depth of 5 *m* is allowed.
(This latter constraint will be removed in the next generation of the AGCM).

7.4 Mixed-layer ocean grid-points

In uncoupled mode, the mixed-layer ocean (MLO) grid-points act as a buffer between the sea grid-points and the ice grid-points. Note that the sea grid-points take their temperature T_s from the observed data set, whereas for ice grid-points the temperature of the sea below the sea-ice is at the freezing point of sea water (the ice/snow surface temperature is computed). For MLO grid-points, a 100 *m* depth is assumed and from the net energy flux at the surface the evolution of temperature for the MLO point can be obtained. However, in reality the temperature of the MLO point is not only influenced by the surface energy flux but also by the influx of heat from the surrounding sea (lateral and from below by overturning). In order that the response of the MLO grid-points be realistic (and also in part because of the diurnal forcing of the model), these effects are parameterized by a relaxation back to the observed SST for that point (with an exponential decay period of about 23 days).

As the model proceeds through an annual cycle, the MLO grid-points can reach freezing point. When this occurs, a MLO point changes to an ice point. If the equatorward point is a sea point, then this point now changes status to a MLO point. The reverse of this occurs for melting. Note that for both cases the current and the *equatorward* grid-points only change status. Since the transform loops compute one latitude row at a time from each pole towards the equator the surface mask can be updated in the correct sequence (subroutine *just_fm*).

8 Surface fluxes (*hsflux*)

If the heat flux into the ground is denoted by G, the net downward shortwave flux by $S_s^{\downarrow}$, the downward longwave flux by $R_s^{\downarrow}$, the upward sensible heat flux by H_s, the upward latent heat flux by E_s, then the energy balance equation linking these quantities may be written as

$$G = (1-\alpha_s)S_s^{\downarrow} + R_s^{\downarrow} - \varepsilon_s \sigma T_s^4 - (H_s + E_s). \qquad 8.1$$

Here T_s represents the effective surface temperature (for longwave radiation purposes), ε_s is the emissivity of the ground, σ is the Stefan-Boltzmann constant, and α_s is surface albedo.

The surface fluxes of heat and moisture, and that of momentum are parameterized following Monin-Obukhov similarity theory. This assumes a surface layer within which the fluxes of heat and momentum are constant in the vertical. The scaling velocity u_* and temperature θ_* are defined from the heat and momentum fluxes; these are constants applying to the whole surface layer. The fluxes can be written as

$$H_s/(\rho C_p) = \overline{\theta' w'} = u_* \theta_* \qquad 8.2$$

$$\left|\underline{\tau}_s\right| / \rho = \left\{(\overline{u' w'})^2 + (\overline{v' w'})^2\right\}^{1/2} = u_*^2. \qquad 8.3$$

In the Louis (1979) method these equations are rewritten as functions of the bulk Richardson number Ri_b:

$$u_*^2 = C_{DN} \left|\underline{V}\right| F_m(z/z_0, Ri_b) \left|\underline{V}\right| \qquad 8.4$$

$$u_* \theta_* = C_{HN} \left|\underline{V}\right| F_h(z/z_T, Ri_b)\,(\theta_s - \theta_1) \qquad 8.5$$

where C_{DN} and C_{HN} are the neutral transfer coefficients for momentum and heat respectively corresponding to height z. In this section and also in Section 10, θ is a column-wise potential temperature defined to equal T_s at the surface (p_s is used rather than p_{1000}); this provides the proper units for the sensible heat flux equation (8.2) to be compatible with the soil fluxes,

$$\theta = T\left(p_s / p\right)^{\kappa}. \qquad 8.6$$

The gradient Richardson number is given by

$$Ri_b = \frac{g}{\theta}\frac{\partial \theta}{\partial z} \Big/ \left|\frac{\partial \underline{V}}{\partial z}\right|^2. \qquad 8.7$$

For the surface flux calculations (surface to model level 1 at height z_1) this becomes

$$Ri_b = gz_1\left(1-\frac{T_s}{T_1}\left(\frac{p_1}{p_s}\right)^{\kappa}\right)/\left|\underline{V}_1\right|^2. \qquad 8.8$$

The incorporation of cloud microphysics in the Mk3 model allows for the effects on surface fluxes of any cloud and latent heating in the model surface layer. In this case the definition of Ri_b is based on that given in Smith (1990):

$$Ri_b = gz_1\left\{\tilde{\beta}_{T1}\left(T_{L1}-T_s\left(\frac{p_1}{p_s}\right)^{\kappa}\right)+\tilde{\beta}_{Q1}\left(q_{W1}-q_{sat}(T_s,p_s)\right)\right\}/\left|\underline{V}_1\right|^2 \qquad 8.9$$

where T_{L1} the liquid-frozen water temperature at the first model level

$$T_{L1} = T_1 - (L_C/C_p)q_{L1} - \{(L_C+L_F)/C_p\}q_{I1} \qquad 8.10$$

and the total water content is

$$q_{W1} = q_{V1} + q_{L1} + q_{I1} = q_{V1} + q_{C1} \qquad 8.11$$

where L_C is the latent heat of condensation and L_F is the latent heat of fusion. The buoyancy parameters $\tilde{\beta}_{T1}$ and $\tilde{\beta}_{Q1}$ are given by

$$\tilde{\beta}_{T1} = (\beta_{T1} - \alpha_{L1}\beta_{C1}), \qquad \tilde{\beta}_{Q1} = \beta_{Q1} + \beta_{C1} \qquad 8.12$$

where

$$\beta_{T1} = \frac{1}{T_1}, \quad \beta_{Q1} = \frac{\delta}{(1+\delta q_{V1} - q_{C1})}, \quad \beta_{C1} = C_1\, a_{L1}\left[\frac{L_C}{C_p}\beta_{T1} - \frac{\beta_{Q1}}{(1-\varepsilon)}\right], \qquad 8.13$$

$$\alpha_{L1} = \frac{L_C}{C_p}\left(\frac{\partial q_{sat}}{\partial T}\right)_1, \qquad a_{L1} = \frac{1}{(1+\alpha_{L1})} \qquad 8.14$$

and C_1 is the cloud fraction. (There is a similar formulation for Ri_b in the stability dependent vertical mixing – see Section 10).

Note that the separate components of the momentum flux are given by

$$\rho\,\overline{u'w'} = \rho C_{DN}\left|\underline{V}\right|F_m(u_s - u_1) \qquad 8.15$$

$$\rho\,\overline{v'w'} = \rho C_{DN}\left|\underline{V}\right|F_m(v_s - v_1) \qquad 8.16$$

where the surface velocity components u_s, v_s are taken to be zero.

The roughness lengths for heat (z_T) and momentum (z_0) are different over land, with $z_0 / z_T = 7.4 \approx e^2$; this corresponds to the currently accepted value of 0.4 for the von Karman constant and follows a suggestion by J.R. Garratt (personal communication, 1991). The transfer coefficients are defined by

$$C_{DN} = k^2 / \{\ln(z / z_0)\}^2 \qquad 8.17$$

$$C_{HN} = k^2 / \{\ln(z / z_0) \ln(z / z_T)\} = k^2 / \{\ln(z / z_0)(2 + \ln(z / z_0))\}. \qquad 8.18$$

For the stable case the functions F_m and F_h are approximated by

$$F_m = (1 + b_m^{\#} Ri_b)^{-2} \qquad 8.19$$

$$F_h = (1 + b_h^{\#} Ri_b)^{-2} \qquad 8.20$$

and for the unstable case

$$F_m = 1 - b_m Ri_b / (1 + c_m |Ri_b|^{1/2}) \qquad 8.21$$

$$F_h = 1 - b_h Ri_b / (1 + c_h |Ri_b|^{1/2}) \qquad 8.22$$

where

$$c_m = c_m^* \, C_{DN} b_m (z / z_0)^{1/2} \qquad 8.23$$

$$c_h = c_h^* \, C_{HN} b_h (z / z_T)^{1/2}. \qquad 8.24$$

The constants are: $b_m = b_h = 10,\ b_m^{\#} = b_h^{\#} = 5$, with $c_m^* = 5.0$ and $c_h^* = 2.6$, as suggested by J.R. Garratt (personal communication, 1991).

In the above equations, all vertical derivatives are evaluated between the surface and the first model level; all other variables are specified at height z, which is here taken to be the height of the first model level above the surface.

Surface latent heat fluxes

Similarly to the sensible heat flux expression derived above, the surface latent heat flux is written as

$$E_s = L\rho \, \overline{q' w'} = L\rho C_{HN} |\underline{V}| F_h (z / z_T, Ri_b) \, (q_s - q_{w1}) \qquad 8.25$$

where L is the latent heat of vaporization. The effective value of surface mixing ratio is denoted by q_s and parameterized as

$$q_s = \alpha\, q_{sat}(T_s) \qquad 8.26$$

where α is a function of soil moisture over land, while $\alpha = 1$ for ice surfaces and $\alpha = 0.98$ over salt water surfaces (the latter value of α being taken from Zeng et al. (1998)).

Surface fluxes over ice

Over ice the fluxes are determined by the above equations, with the exception that the roughness lengths z_0 and z_T are both set to 0.01 *m*.

Surface fluxes over the sea

Over the sea, the above equations require several modifications. The roughness length (z_0) is diagnosed from the Charnock (1955) formula

$$z_0 = 0.018 \left| \underline{\tau_s} \right| / (\rho g), \qquad 8.27$$

which is combined with (8.3) and (8.4) for $\left| \underline{\tau_s} \right|$ and solved iteratively via three Newton-Raphson iterations at each sea point. The first guess is 0.001 *m* and a minimum value of 0.000015 *m* is imposed. The roughness length for heat z_T is presently set equal to z_0 over the sea. The roughness lengths are used in the calculation of C_{DN} and in the unstable calculation of F_m and F_h for the momentum, heat and moisture fluxes. Guided by experimental results (Bunker 1976; Liu et al. 1979; J. R. Garratt, personal communication, 1991), we take C_{HN} over the sea to be constant rather than use (8.18). A value of 0.0012 is considered appropriate for the present height of the lowest model level ($\eta = 0.9955$) for an 18-level T63 model in conjunction with cloud microphysics (Section 13) and the UKMO convection scheme (Section 14).

9 Soil and snow parameterizations (*datard, insoilveg; surfupa, surfa, snowpr, stemp; surfupb, surfb, smoisture)*

An improved version of the land-surface scheme has been implemented into the Mk3 AGCM, with a new snow model and a new parameterization of soil moisture and temperature. The new snow model computes the temperature, snow density and thickness of three snowpack layers, with the processes of snow accumulation, melting, and a physically based snow albedo included. The soil model has six layers with three prognostic variables: soil temperature, liquid water, and ice content, and the amount of ice formed or melted is calculated from energy and mass conservation. (The previous soil scheme (Mk1 model) used a force restore method for moisture and a three-layer diffusion scheme for temperature. These are still available in the model and are contained in subroutines *surfupa* and *surfupb*, with details being available in McGregor et al. 1993)

Surface data sets based on Dorman and Sellers (1989) have been used to describe surface properties for each individual land grid box. The data input (subroutine *datard*) includes seasonally varying data sets (one per month) for albedo, stomatal resistance and roughness length. The vegetation fraction is provided as an annual mean value. However the vegetation fraction varies for some vegetation types (see next) on a seasonal basis. The soil temperature at about $0.5\,m$ is the main factor influencing the seasonal variation in vegetation fraction. The vegetation types most affected are crops, deciduous trees, grasses and ground cover. Each land grid point in the model is ascribed one of 13 possible land surface and/or vegetation types. This is also annually invariant (*datard*). Each of the 13 types is given in Table 2.

1	Broadleaf evergreen trees (tropical forest)
2	Broadleaf deciduous trees
3	Broadleaf and needleleaf trees
4	Needleleaf evergreen trees
5	Needleleaf deciduous trees
6	Broadleaf trees with ground cover (savannah)
7	Groundcover only (perennial)
8	Broadleaf shrubs with groundcover
9	Broadleaf shrubs with bare soil
10	Dwarf trees and shrubs with groundcover
11	Bare soil
12	Winter wheat and broadleaf deciduous trees
13	Perpetual ice

Table 2. Vegetation/land type.

The final land surface data set (in subroutine *datard*) is for the soil types. The data set specifying the geographical distribution of soil type is based on Zobler (1992). There are 9 soil types (Zobler texture) included in the Mk3 model. These are given in Table 3.

1	Coarse	Sand/loamy sand
2	Medium	Clay loam/silty clay loam/silt loam
3	Fine	Clay
4	Coarse-medium	Sandy loam/loam
5	Coarse-fine	Silty clay
6	Medium-fine	Silty clay
7	Coarse-medium-fine	Sandy clay loam
8	Organic	Peat
9	Land ice	Frozen soil below ice

Table 3. Soil type.

The land surface model is initialized (subroutine *insoilveg*) by the specification of various quantities associated with vegetation type, soil type, and soil depth. Some key vegetation parameters (with coding names in quotes) are:

a) ‘rlaim’ : maximum leaf area index
b) ‘slveg’ : variation in leaf area index
c) ‘rlais’ : stem leaf area index
d) ‘scveg’ : variation in vegetation fraction
e) ‘rsmin’ : minimum stomatal resistance.

In the Mk3 land surface model, a prescribed seasonally varying stomatal resistance (input via subroutine *datard*) is available. However, in the current version of the model, this is replaced by a computed seasonally varying stomatal resistance that is based upon model parameters and the (annually invariant) minimum stomatal resistance (‘rsmin’) above. The soil layers (6) each have a preset thickness (‘zs_k’); These are given in Table 4 from the surface down. The total soil depth is 4.6 *m*. The fractional composition (of sand, clay and silt) for each of the 9 soil types is shown in Table 5. For soil type 9 (permanent ice – for example the Antarctic plateau) the soil defined in Table 5 is not used, and soil parameters are subsequently replaced by parameters for ice.

	1	2	3	4	5	6
Soil depth	0.022	0.058	0.154	0.409	1.085	2.872

Table 4. Soil layer depths (*m*), 1 = surface layer.

	1	2	3	4	5	6	7	8	9
Sand	0.83	0.37	0.17	0.60	0.52	0.27	0.58	0.13	0.37
Clay	0.09	0.30	0.66	0.20	0.42	0.48	0.27	0.17	0.30
Silt	0.08	0.33	0.17	0.20	0.06	0.25	0.15	0.70	0.33

Table 5. Soil composition per 9 soil types.

The following soil properties (with coding names in quotes and symbolic representations as used in model equations) are used in the model:

a) ‘cnsd’ = k_s soil thermal conductivity (for dry soil)
b) ‘hyds’ = K hydraulic conductivity
c) ‘sucs’ = ψ matrix potential
d) ‘css’ = c_s specific heat capacity
e) ‘rhos’ = ρ_s density (when dry)
f) ‘ssat’ = η_{sat} saturation content
g) ‘swilt’ = η_w wilting content
h) ‘sfc’ = η_{fc} field capacity.

The application of the above soil properties, some of which depend upon soil-layer thicknesses and fractional composition, is explained in more detail in the following sections.

9.1 Soil parameterizations

9.1.1 Soil moisture

Soil is composed of three constituent phases, namely the solid phase, water, and air (Hillel 1982). Water and air compete for the same pore space and continually change their volumetric fractions due to precipitation, snow melt, evapotranspiration and drainage. Soil hydraulic and thermal characteristics depend on soil type and frozen and unfrozen soil moisture content. Soil moisture is assumed to be at the ground temperature, so there is no heat exchange between the moisture and the soil due to the vertical movement of water. Soil moisture is considered in terms of liquid and ice components, $\eta_{sm} = \eta_l + \eta_i$. Each soil type is described by the following hydraulic characteristics: saturation content η_{sat}, wilting content η_w, and field capacity η_{fc}. η_{sat} is equal to the volume of all the soil pores, which can fill with water under extremely wet conditions. Here, an additional variable is used, the so-called actual saturation η_{Asat}, which excludes the pores filled with ice, $\eta_{Asat} = \eta_{sat} - \eta_i$.

The one-dimensional conservation equation for soil moisture in the absence of ice is described by

$$\frac{\partial \eta_{sm}}{\partial t} = -\frac{\partial F}{\partial z} + r_i(z), \qquad 9.1$$

where F is the soil water flux and r_i terms include the runoff, drainage and root extraction for evapotranspiration. Parameterization of transpiration is described by Kowalczyk et al. (1991) and is based on Noilhan and Planton (1989). The water flux, F, in an unsaturated soil is given by Darcy's law

$$F = K\left(-\frac{\partial \psi}{\partial z} + 1\right), \qquad 9.2$$

where K is hydraulic conductivity and ψ is the matrix potential. Combining Equ. (9.1) with (9.2) we obtain the Richard's equation

$$\frac{\partial \eta_{sm}}{\partial t} = -\frac{\partial}{\partial z}\left(K - K\frac{\partial \psi}{\partial z}\right) + r_i(z), \qquad 9.3$$

To solve Equ. (9.3) we need to assume forms for the relationships between the hydraulic conductivity, the matrix potential, and the soil moisture content. The dependencies of Clapp and Hornberger (1978) are used,

$$K = K_s\left(\frac{\eta_l}{\eta_{Asat}}\right)^{2b+3} \qquad 9.4$$

and

$$\psi = \psi_s\left(\frac{\eta_l}{\eta_{Asat}}\right)^{-b} \qquad 9.5$$

where K_s and ψ_s are the values at saturation and b is non-dimensional constant. η_{Asat} is calculated on the assumption that soil ice becomes the part of the solid matrix. Defining a fractional liquid content as a function of actual saturation, $\eta_{lf} = \eta_l / \eta_{Asat}$ and substituting relations (9.4) and (9.5) into Equ. (9.3), we obtain the equation for the liquid water transfer

$$\eta_{Asat} \frac{\partial \eta_{lf}}{\partial t} = \frac{\partial}{\partial z}\left(K_s \psi_s b \eta_{lf}^{b+2} \frac{\partial \eta_{lf}}{\partial z} - K_s \eta_{lf}^{2b+3} \right) + r_i(z). \qquad 9.6$$

The top boundary condition represents the flux infiltrating the surface, which depends on rainfall, snowmelt, evaporation, surface runoff and soil hydrological properties. At the bottom, non-zero gravitational drainage occurs in order to restore the water profile to its field capacity. To resolve the seasonal cycle of soil moisture and temperature as well as their interannual variations, the depth of the total soil layer in Mk3 is $4.6\,m$ (compared to $1.5\,m$ in Mk2) – see Table 4. This will have an impact in the regions with strong seasonal precipitation patterns.

9.1.2 Soil temperature

The equation for the vertical temperature profile is:

$$\rho_s c_s \frac{\partial T_s}{\partial t} = \frac{\partial}{\partial z}\left(k_s \frac{\partial T_s}{\partial z} \right), \qquad 9.7$$

where ρ_s is the density $(kg\ m^{-3})$, c_s is the specific heat $(J\ kg^{-1}\ K^{-1})$ and k_s is the thermal conductivity $(W\ m^{-1}\ K^{-1})$ of the soil. The volumetric heat capacity $(\rho_s c_s)$ is calculated as the weighted sum of the heat capacity of all the constituents; dry soil, liquid water and ice,

$$\rho_s c_s = (1-\eta_{sat})\rho_{soil} c_{soil} + \eta_l \rho_w c_w + \eta_i \rho_{ice} c_{ice}. \qquad 9.8$$

The air heat capacity is neglected as it is three orders of magnitude lower. In most soils the average density of the solid particles such as quartz and minerals is in the range 2.5 to $2.8x10^3\ kg\ m^{-3}$ (Marshall et al. 1979). The dry soil density is estimated using soil porosity and assuming the same unit weight for solid components,

$$\rho_{soil} = (1-\eta_{sat})2700. \qquad 9.9$$

Soil thermal conductivity k_s plays a crucial role in determining the depth of freezing /thawing. It varies by about one order of magnitude as the soil approaches saturation point and increases further due to the ice contents. A method for predicting k_s in both frozen and unfrozen soils is based on Johansen (1975), and was previously discussed by Farouki (1986). k_s is calculated as a combination of dry k_{dry} and saturated k_{sat} conductivities, weighted by a normalized thermal conductivity called the Kersten number,

$$k_s = K_r (k_{sat} - k_{dry}) + k_{dry}, \qquad 9.10$$

where k_{dry} is a function of the dry soil density, k_{sat} depends on the soil porosity η_{sat}, the quartz content, and the liquid and ice volume fraction, whilst the Kersten number K_r is a simple function of saturation. The only new parameter required by the method is a soil quartz content. Peters-Lidard et al. (1998) estimate the quartz content for 13 soil types and assesses the sensitivity of k_s calculations to quartz content. The method has shown to be superior to other methods for predicting thermal conductivity for unfrozen and frozen soil (Peters-Lidard et al. 1998). As soil temperature can be modified by several $°C$ when the value of its thermal properties changes due to water or ice content, the soil thermal properties are recalculated at each time step.

The bottom boundary condition for Equ. (9.7) is zero heat flow. At the top boundary the net heat flux at the surface G is given by the equation

$$G = (1-\alpha_s)S_s^{\downarrow} + R_s^{\downarrow} - \varepsilon_s \sigma T_s^4 - (H_s + E_s)\,. \qquad 9.11$$

(See start of Section 8 for a definition of terms). The fluxes are parameterized following Monin-Obukhov similarity theory, with details given in Section 8 and additional information in Kowalczyk et al. (1991). Implicit time differencing is used and both Equ. (9.6) and (9.7) are solved using a tri-diagonal solver.

Following the solution of Equ. (9.6) and (9.7), the freezing/thawing calculations are performed. If a soil layer cools below freezing point and there is unfrozen soil moisture, ice is formed. The amount of ice formed in a layer of thickness δz is limited by the amount of liquid water and available energy

$$\rho_w \delta z \delta \eta_i = \min\left\{\rho_w \eta_l \delta z\,,\, (T_{frz} - T_s)\rho_s c_s \delta z / L_f\right\} \qquad 9.12$$

where L_f is the latent heat of fusion and T_{frz} is the freezing temperature. During the freezing, latent heat is released warming the soil. The layer temperature drops below freezing after all the water turns into ice. Ice decreases soil porosity η_{Asat}, but the liquid moisture can move through the remaining unfrozen soil pores. The melting process takes place when the temperature of a layer with ice increases to $0°C$. The amount of ice melted is calculated in a similar fashion. In reality, the natural water in the soil and rocks freezes over a range of temperatures below $0°C$.

9.2 Snow model

Snow cover increases the surface albedo, thereby reducing the available energy at the surface. This results in lower surface temperatures and a cooler lower atmosphere. Snow cover also prevents excessive soil heat loss to the atmosphere, allowing the temperature of the underlying soil to remain warmer. The insulating properties of the snow are due to its low thermal conductivity, which for new snow is roughly an order of magnitude lower than that of the soil. A typical temperature profile throughout the early winter snowpack has a strong vertical gradient immediately below the surface and a weak gradient close to the ground (Gray and Male 1981). To adequately represent the energy exchange with the atmosphere, the temperature gradients through the snowpack need to be reproduced. A model with at least three layers is required for

this purpose. The model described here computes the snow density, temperature and thickness of three snowpack layers.

Modelling of snow cover evolution requires representation of the following related processes: snow deposition, snow cover on vegetation, snow albedo, snow accumulation, snow metamorphism and thermal properties, snow melting.

9.2.1 Snow deposition

The amount deposited depends on the snow-rain criterion used by the model. Snow models are sensitive to this criterion as described by Loth et al. (1993) and Yang et al. (1997). The snow/rain partition may vary depending on the site elevation, season and local climate as described by Yang et al. (1997). Here, the information on the liquid/solid precipitation is provided to the surface scheme by the cloud liquid water parameterization included in the GCM (Rotstayn 1997).

9.2.2 Snow cover interaction with vegetation and snow albedo

The interaction of vegetation and snow cover does not involve a direct heat exchange. Snow cover interacts with vegetation in two simple ways. Firstly, it reduces the fractional vegetation cover due to vegetation being partially buried under the snow. The formula for the fraction of vegetation protruding above the snow cover is as follows

$$\sigma'_{veg} = \left(1 - \frac{S_d}{S_d + 2\ zo_{veg}}\right)\sigma_{veg}, \qquad 9.13$$

where S_d is the snow depth in m, zo_{veg} is the roughness length of vegetation and σ_{veg} is the snow-free vegetation cover fraction. Secondly, vegetation presence affects the snow computations by decreasing the overall surface albedo (see subroutine *surfset*),

$$\alpha_s = \sigma'_{veg}\,\alpha_{veg} + (1 - \sigma'_{veg})(\alpha_{bg}(1 - F_{bg}) + \alpha_{sn}F_{bg}), \qquad 9.14$$

where α_{veg}, α_{bg}, and α_{sn} are vegetation, bare ground and snow albedo respectively.

$$F_{bg} = \frac{S_{sn}}{S_{sn} + 2\ zo_{bg}} \qquad 9.15$$

is a fraction of bare ground covered by snow, with $zo_{bg} = 0.01\,m$ being the roughness length. The snow albedo (α_{sn}) calculations are based on Dickinson et al. (1993) as follows: the snow albedo depends on zenith angle (ξ_a) and snow age:

$$\alpha_V = 0.4\,f(\xi_a)\{1 - \alpha_{VD}\} + \alpha_{VD} \qquad 9.16$$

$$\alpha_{IR} = 0.4\,f(\xi_a)\{1 - \alpha_{IRD}\} + \alpha_{IRD}. \qquad 9.17$$

In the Mk3 model, we currently set $\alpha_{sn} = (\alpha_V + \alpha_{IR})$, where α_V = albedo for $\lambda < 0.7\mu m$, α_{IR} = albedo for $\lambda > 0.7\ \mu m$, and the subscript '$_D$' denotes diffuse albedos as given by

$$\alpha_{VD} = [1 - 0.2Fage]\,\alpha_{VO} \qquad 9.18$$

$$\alpha_{IRD} = [1 - 0.5Fage]\,\alpha_{IRO} \qquad 9.19$$

and

α_{VO} = 0.95, the albedo for visible radiation on snow, $\xi_a < 60°$,

α_{IRO} = 0.65, the albedo of new snow for near-infrared solar radiation, $\xi_a < 60°$,

$f(\xi_a)$ = factor (0-1) giving increase in snow albedo for $\xi_a > 60°$,

Fage = a transformed snow age (defined below) and used to give the fractional reduction of snow albedo due to snow ageing (assumed increasing grain size and soot) for $\xi_a < 60°$.

The following parameterization is used (with b = 2.0):

$$f(\xi_a) = \frac{1}{b}\left[\frac{b+1}{1+2b\cos(\xi_a)} - 1\right] \qquad 9.20$$

$$f(\xi_a) = 0 \quad \text{if} \quad \cos(\xi_a) > 0.5$$

Snow albedo decreases with time due to snow ageing and accumulation of dirt/soot. *Fage* is parameterized by

$$Fage = 1 - 1/(1 + SNage) \qquad 9.21$$

where the non-dimensional age of the snow *SNage* is incremented as a model prognostic:

$$SNage(\tau + \Delta t) = (SNage(\tau) + \Delta SNage)(1 - 100\ \Delta NewSnow)\,. \qquad 9.22$$

Here the change in snow age is given by (with $\tau_0^{-1} = 10^{-6}\,s^{-1}$):

$$\Delta SNage = \tau_0^{-1}(\exp(r_1) + r_2 + r_3)\Delta t\,, \qquad 9.23$$

$$r_1 = 5000\left(\frac{1}{273.1} - \frac{1}{T_s}\right), \qquad 9.24$$

$$r_2 = \min(0, 10\ r_1)\,, \qquad 9.25$$

and $r_3 = 0.008$ over permanent ice cover in Antarctica and Greenland, $r_3 = 0.3$ elsewhere. See Dickinson et al. (1993) for an explanation of terms used in $\Delta SNage$. A snowfall (in a given model timestep) of 0.01 *m* of liquid water is assumed to reset the snow age (and thus albedo) to that of new snow. Hence the snow age is reduced by a factor depending on the amount of new snow $\Delta NewSnow$ (in *m*, maximum value 0.01) in Eqn. (9.22).

9.2.3 Snow accumulation

The change in the total snow mass (S_{sn}) is based on the following mass budget

$$\frac{\partial S_{sn}}{\partial t} = (P_{sn} + P_{rain})(1-\sigma'_{veg}) + (P'_{sn}+P'_{rain})\sigma'_{veg} - E_{sn} - S_{melt}, \qquad 9.26$$

where P_{sn} is snowfall rate and P_{rain} is rainfall rate above the bare ground. P'_{sn} and P'_{rain} are the corresponding rates under the canopy. E_{sn} is the rate of sublimation and S_{melt} is snowmelt, all in $kg\ m^{-2}\ s^{-1}$. Rainfall temperature is assumed to equal air temperature. Rain falling on snow freezes at the surface, releasing the latent heat. A separate mass balance equation for the canopy intercepted precipitation is carried out. The discretization of the snowpack depth into layers changes with snowfall and snowmelt, sublimation and changes in density. When the layer thickness changes, the mass and heat content of the layers are redistributed accordingly. The thickness of the layers was chosen to resolve the temperature gradients throughout the pack. The top layer is $Sd_1 = 0.07\ m$ to represent a diurnal range of surface temperature. The thickness of the remaining layers are $Sd_2 = 0.3(Sd_T - 0.07)$ and $Sd_3 = 0.7(Sd_T - 0.07)$, where Sd_T is the total depth of the pack. The minimum thickness of the two lower layers is $0.02\ m$. If the total snow depth becomes less than $0.11\ m$, the snowpack is treated as one layer with all of its properties averaged. In fact, in late winter or early spring, the snow is old and the temperature gradient through the pack is weaker, and the pack may even become isothermal (see Gray and Male 1981).

9.2.4 Snow metamorphism and snow thermal properties

The process taking place within the snow cover changing the shapes of the snow grains is known as metamorphism. Metamorphism includes changes due to water vapour diffusion, heat transfer, liquid water movement, and compaction caused by the overlying snow mass. Here, the snow density was chosen to represent the bulk snow properties and the metamorphism is accounted for through changes in snow density. Snow density affects the temperature of the snow through its effects on the snow thermal conductivity. Snow density is also used for the snow albedo calculations. Physical processes such as water vapour diffusion and liquid water movement are neglected.

The snow density ρ_{sn} increases with time due compaction and settling processes. Each of the processes that increases density (hereafter termed “densification”) is treated sequentially, as shown below. The density of the fresh snow is $100\ kg\ m^{-3}$, however with time the density may increase to $450\ kg\ m^{-3}$. Further densification occurs due to the refreezing of melting water or rain. In the model the changes in density are parameterized using empirical relations from Anderson (1976); they are described in detail by Loth et al. (1993).

Settling occurs in new snow layers, reshaping the needle-like snow crystals to round grains. Mass transfer via vapour phase is the main mechanism here (Gray and Male 1981). The densification due to settling is parameterized as a function of temperature and snow density,

$$\frac{1}{\rho_{sn}}\frac{\partial \rho_{sn}}{\partial t} = c_1 \exp(-c_2(273.15 - T_{sn}) - c_3(\rho_{sn} - \rho_d)), \qquad 9.27$$

where $c_1 = 2.8x10^{-6}\ s^{-1}$, $c_2 = 0.04\ K^{-1}$, $\rho_d = 150\ kg\ m^{-3}$ and c_3 in $m^3\ kg^{-1}$ is given by

$$c_3 = \begin{cases} 0 & if\ \rho_{sn} < \rho_d \\ 4600 & if\ \rho_{sn} \geq \rho_d \end{cases}.$$

Both c_2 and c_3 were obtained from calibrations by Anderson (1976); the coefficient c_1 and density ρ_d were determined on the basis of observations (Williams and Smith 1989).

Having obtained a partially updated snow density (say $\rho_{sn}^{\#}$) from the integration of (9.27) the compaction under the weight of the snowpack is then obtained as a function of the overlying snow weight and the viscosity coefficient π_c:

$$\frac{1}{\rho_{sn}}\frac{\partial \rho_{sn}}{\partial t} = \frac{g}{\pi_c}\int_z^{S_d(t)} \rho_{sn}^{\#}(z', t)\, dz' \qquad 9.28$$

where g is acceleration due to gravity and $S_d(t)$ is snow depth. The viscosity coefficient π_c represents the resistance of the snow to a vertical pressure and is described as

$$\pi_c = \pi_T \exp(b_1 \rho_{sn}), \qquad 9.29$$

where $b_1 = 0.021\ m^3\ kg^{-1}$. This relationship was derived from the observations of Kojima (1967). The viscosity of the snow π_T is given by

$$\pi_T = \pi_0 \exp(b_2(273.15 - T_{sn})), \qquad 9.30$$

where $b_2 = 0.081\ K^{-1}$ and $\pi_0 = 3.7x10^7\ Pa\ s$.

In the case of snowfall, the final density of the first layer is recalculated as the weighted average of the ρ_{sn} and the fresh snow density.

Following the densification calculations, the adjusted layer thicknesses are calculated by taking into account new snowfall, snowmelt, sublimation and densification. Mass and heat content is redistributed and heat conduction is calculated using the equation

$$\rho_{sn} c_{sn} \frac{\partial T_{sn}}{\partial t} = \frac{\partial}{\partial z}\left(k_{sn} \frac{\partial T_{sn}}{\partial z} \right), \qquad 9.31$$

where ρ_{sn} is the density, c_{sn} is the specific heat capacity (taken as $2095\ J\ kg^{-1}\ K^{-1}$) and k_{sn} is the thermal conductivity of the snow layers. Conduction of heat in snow involves the transfer of the heat through ice grains and across air spaces, and radiant energy exchange across the pores (Gray and Male 1981). Due to this complexity, k_{sn} represents an effective conductivity

incorporating all the processes. It is parameterized using the relationship proposed by Anderson (1976)

$$k_{sn} = a_1 + a_2 \rho_{sn}^2, \qquad 9.32$$

where $a_1 = 0.02\, W\, m^{-1}\, K^{-1}$ and $a_2 = 2.5x10^{-6}\, W\, m^5\, K^{-1}\, kg^{-2}$. As snow 'ages', its thermal conductivity increases as its density increases, especially for the lower or melting parts of the snowpack.

At the bottom of the snowpack boundary the energy balance is influenced by the ground heat flux through the soil surface. At the top, the energy balance of the snow cover is influenced by the net heat flux at the surface,

$$G = (1-\alpha_{sn})S_s^{\downarrow} + R_s^{\downarrow} - \varepsilon_{sn}\sigma T_{sn}^4 + R_{rain} - (H_s + E_s) \qquad 9.33$$

where α_{sn} is snow albedo, ε_{sn} is the emissivity of the snow, and R_{rain} is the input due to rain. The rainfall freezes in the first layer releasing the latent heat on contact with the snow. To account for the surface smoothing effect of snow when calculating the surface fluxes, the roughness length varies linearly between $0.01\, m$ for bare ground to $0.0024\, m$ for a water equivalent snow depth of $0.11\, m$ or more.

Equation (9.31) is coupled to T_s calculations and is solved together with Equ. (9.7), using a tri-diagonal solver.

9.2.5 Snow melting

When the temperature of the snow layer exceeds the melting point, a fraction of the snow melts and the temperature is restored to $0°C$. As the liquid water holding capacity of snow is zero, the snowmelt generated in one layer does not flow down to the lower layers, but is released to the soil or runoff. Rain falling on the snow freezes, releasing the latent heat. Rain has the potential to warm the snowpack quite quickly, as opposed to slow heat transfer in dry snow. When the latent heat release causes the temperature to exceed the melting point the draining water is treated as snowmelt.

10 Vertical mixing (*hvertmx*)

Turbulent vertical mixing in the model is parameterized in terms of stability-dependent K theory and follows Blackadar (1962). The diffusion coefficients (K_m and K_h) are expressed in the form

$$K_{m,h} = l_m^2 \left|\frac{\partial V}{\partial z}\right| F_{m,h}(Ri_b) \qquad 10.1$$

with Blackadar's (1962) expression for the mixing length l_m (at height z above the surface):

$$l_m = kz/(1+kz/\lambda_l)\,. \qquad 10.2$$

Here k (= 0.4) is the von Karman constant. The asymptotic mixing length λ_l is an adjustable constant: in Mk3 we use 30 *m* which is the same as that used in the NCAR CCM3 model. The expression for the gradient Richardson number Ri_b (based upon θ_V) is as follows. If the cloud microphysics scheme *is not* in use, then the expression is:

$$Ri_b = g\left\{\frac{1}{\theta}\frac{\partial\theta}{\partial z} + \delta\frac{\partial q}{\partial z}\right\}\Big/\left|\frac{\partial \underline{V}}{\partial z}\right|^2. \qquad 10.3$$

Here θ is a column-wise potential temperature defined by $\theta = T(p_s/p)^{\kappa}$, and $\delta = (1/\varepsilon) - 1 = 0.608$ (using $\varepsilon = 0.622$, the ratio of the molecular weights of water and dry air). A minimum default vertical wind shear of $1\,m\,s^{-1}$ is imposed.

If the cloud microphysics scheme *is* in use (which is standard in Mk3), then the expression for Ri_b is based upon Smith (1990) and is defined by

$$Ri_b = g\left\{\tilde{\beta}_T\frac{\partial\theta_L}{\partial z} + \tilde{\beta}_Q\frac{\partial q_W}{\partial z}\right\}\Big/\left|\frac{\partial \underline{V}}{\partial z}\right|^2. \qquad 10.4$$

Here $\theta_L = T_L(\theta/T)$ and the liquid-frozen water temperature T_L is given by

$$T_L = T - (L_C/C_p)q_L - \{(L_C+L_F)/C_p\}q_F\,, \qquad 10.5$$

and the total water content

$$q_W = q + q_L + q_F = q + q_C\,, \qquad 10.6$$

where L_C is the latent heat of condensation and L_F is the latent heat of fusion. In the following, L will be used to represent L_C or $L_C + L_F$ whichever is appropriate for the state of the cloud water. The buoyancy parameters $\tilde{\beta}_T$ and $\tilde{\beta}_Q$ are given by

$$\tilde{\beta}_T = (\beta_T - \alpha_L\beta_C)(T/\theta)\,, \qquad \tilde{\beta}_Q = \beta_Q + \beta_C \qquad 10.7$$

where

$$\beta_T = \frac{1}{T}, \quad \beta_Q = \frac{\delta}{(1+\delta q - q_C)}, \quad \beta_C = C\,a_L\left[\frac{L}{C_p}\beta_T - \frac{\beta_Q}{(1-\varepsilon)}\right], \qquad 10.8$$

$$\alpha_L = \frac{L_C}{C_p}\frac{\partial q_{sat}}{\partial T}, \qquad a_L = \frac{1}{(1+\alpha_L)} \qquad 10.9$$

and C is the cloud fraction.

The expressions used for F_m and F_h are also based on those given by Smith (1990). For unstable conditions ($Ri_b < 0$):

$$\begin{aligned} F_m &= 1 - 10Ri_b / (1 + 2.5\left|Ri_b\right|^{1/2}) \\ F_h &= 1 - 10Ri_b / (1 + 0.4\left|Ri_b\right|^{1/2}) . \end{aligned} \qquad 10.10$$

For stable conditions ($Ri_b > 0$), $F_h = F_m$ and

$$\begin{aligned} F_m &= (1 - 5.0Ri_b)^2 \qquad \text{for } Ri_b < 0.05 \\ F_m &= 1.6875 / (1 + 40.0Ri_b) \qquad \text{for } Ri_b \geq 0.05 . \end{aligned} \qquad 10.11$$

The diffusion coefficients K_m and K_h are required at the vertical half-levels. Thus in the following sub-sections, z corresponds to a half-level value and Δz is the corresponding distance between the surrounding full-levels.

10.1 Shallow convection

The shallow cumulus convection scheme of Geleyn (1987) is an optional parameterization in the Mk3 model. It is *not* used if the *UKMO* cumulus convection scheme is in operation (which is the standard convection scheme used in the Mk3 model – see Section 14). The shallow convection scheme may be used in conjunction with the Mk1 model mass flux convection scheme or the Kuo convection scheme (see also Section 14). In the implementation of the Geleyn (1987) shallow convection scheme, there is a minor modification in that potential temperature is used rather than static energy. The effect is to modify the vertical mixing as described above by replacing $\partial\theta / \partial z$ in (10.3) or (10.4) for Ri_b by

$$\frac{\partial\theta}{\partial z} + \frac{L}{C_p} \min\left\{0, \frac{\partial q}{\partial z} - \frac{\partial q_{sat}}{\partial z}\right\} \qquad 10.12$$

where q_{sat} is the saturated mixing ratio. As for the usual vertical mixing calculations this provides K_m and K_h at all model half-levels between the bottom and top level. Modification of the fields at the first level due to surface fluxes is obtained by incorporation of those fluxes (in the case of T and q), as previously calculated. An alternative shallow convection scheme following the ideas of Tiedtke (1987) is also available in the model.

10.2 Time integration of vertical mixing

At this stage model fields are available for timesteps (τ - 1) and (τ) and a first approximation to fields at the new timestep is available, denoted by (τ + 1)* say, but where the vertical mixing and gravity wave processes have not yet been carried out. An implicit split calculation is performed for T, q, u, v over the double (leapfrog) timestep interval. T and q are updated at this latest time

interval. However, effective time tendencies are deduced for u and v; these are then used to produce time tendencies for divergence and vorticity which are combined with those from the gravity wave drag parameterization and added in later while proceeding to (τ + 1) values. This procedure avoids an extra grid to spectral transform for the winds. The description here is given for an implicit split calculation over a time interval $2\Delta t$.

The following equations are presented for θ, in the special form defined by Equ. (8.6). The equations for q, u and v follow in a very similar manner. Surface values are denoted by the subscript s. Note that $u_s = v_s = 0$. The split equations to be solved for vertical mixing are

$$\frac{\partial \theta}{\partial t} = -\frac{1}{\rho}\frac{\partial}{\partial z}(\rho\,\overline{\theta' w'}) \qquad 10.13$$

where the fluxes $\overline{\theta' w'}$ are given in terms of the above K_h as

$$\overline{\theta' w'} = -K_h \frac{\partial \theta}{\partial z}. \qquad 10.14$$

It is convenient to define the vertical discretization operator (Δ) as follows:

$$\Delta\phi_k = \phi_{k+0.5} - \phi_{k-0.5} \quad \text{for } k = 1, 1.5, 2, 2.5, \ldots \qquad 10.15$$

where the k = 0.5 level is to be taken as synonymous with the surface. From the hydrostatic equation we have

$$\frac{\partial p}{\partial z} = -g\rho = -\frac{gp}{RT}. \qquad 10.16$$

In hybrid coordinates, with a only a little approximation, this gives

$$\frac{g\rho}{p_s} \cong \frac{g\eta}{RT} \cong -\frac{\Delta\eta}{\Delta z}. \qquad 10.17$$

Performing the vertical differencing and substituting ρ and using $\overline{\theta' w'}$ for the $k = 1$ equation yields

$$\left(\frac{\partial \theta}{\partial t}\right)_k = \left(\left(K_h \frac{\Delta\eta}{\Delta z}\frac{\Delta\theta}{\Delta z}\right)_{k+0.5} - \left(\frac{g\eta}{RT}\,\overline{\theta' w'}\right)_{k-0.5}\right)/\Delta\eta_k \qquad k = 1, 2, 3, .. \qquad 10.18$$

We choose to write the flux at the surface as

$$\overline{\theta' w'} = \varepsilon_X\left(\overline{\theta' w'}\right)_s + (1-\varepsilon_X)C_h\left|\underline{V}_1\right|(\theta_s - \theta_1) \qquad 10.19$$

where either $\varepsilon_X = 1$ for surface heat flux passed through from the surface flux routine (normal option for heat and moisture fluxes) or $\varepsilon_X = 0$ for only the net transfer coefficient precalculated

(normal option for momentum fluxes). $\left(\overline{\theta' w'}\right)_s$ is an alternative notation for $H_s/(\rho C_p)$. Equation (10.18) may then be rewritten as

$$\left(\frac{\partial\theta}{\partial t}\right)_k = \left((G\,\Delta\theta)_{k+0.5} - (G\,\Delta\theta)_{k-0.5}\right)/\Delta\eta_k \qquad k = 2, 3, .. \qquad 10.20$$

and

$$\left(\frac{\partial\theta}{\partial t}\right)_1 = \left((G\,\Delta\theta)_{1.5} - (G\,\Delta\theta)_{0.5} - \frac{\varepsilon_X\, g}{RT_s}\left(\overline{\theta' w'}\right)_s\right)/\Delta\eta_1 \qquad 10.21$$

where

$$G_{k+0.5} = \left(K_h \frac{\Delta\eta}{(\Delta z)^2}\right)_{k+0.5} \qquad \text{for} \quad k = 1, 2, 3, .. \qquad 10.22$$

and

$$G_{0.5} = (1-\varepsilon_X)\frac{g}{RT_0} C_h \left|\underline{V}_1\right|. \qquad 10.23$$

A zero flux condition is enforced at the top of the model by specifying $K_h = 0$ there. These equations are amenable to an implicit tri-diagonal solution. For this they are conveniently rewritten as

$$2\Delta t\left(\frac{\partial\theta}{\partial t}\right)_k = -A_k\theta_{k-1} + (A_k + C_k)\theta_k - C_k\theta_{k+1} - \varepsilon D_k \qquad 10.24$$

where

$$A_k = -2\Delta t \frac{G_{k-0.5}}{\Delta\eta_k} \qquad \text{for} \quad k = 1, 2, 3, .. \qquad 10.25$$

$$C_k = -2\Delta t \frac{G_{k+0.5}}{\Delta\eta_k} \qquad \text{for} \quad k = 1, 2, 3, .. \qquad 10.26$$

$$D_k = 0 \qquad \text{for} \quad k = 2, 3, .. \qquad 10.27$$

$$D_1 = 2\Delta t \frac{g}{RT_s}\frac{(\overline{\theta' w'})_s}{\Delta\eta_1}. \qquad 10.28$$

The final equations, in a form suitable for tri-diagonal implicit solution, are

$$A_k\theta_{k-1}^{\tau+1} + (1 - A_k - C_k)\theta_k^{\tau+1} + C_k\theta_{k+1}^{\tau+1} = \theta_k^{\tau+1^*} - \varepsilon_X \; D_k \,. \qquad 10.29$$

Once $\theta^{\tau+1}$ has been evaluated, $T^{\tau+1}$ is obtained from $\theta = T(p_s / p)^{\kappa}$.

10.3 Time integration of vertical fluxes of moisture

The equations for updating water vapour are very similar to those above. The changes are that only the $\varepsilon_X = 1$ option is available, and θ is replaced by q in all equations. The surface moisture flux $(\overline{q'w'})_s$ is just an alternative notation for E_s / ρ. Vertical mixing is also applied to cloud liquid water and frozen water (q_L and q_F), although in these cases the surface flux term is zero.

11 Gravity wave drag (*gwdrag*)

The inclusion of gravity wave drag parameterization is beneficial to the climate simulations of atmospheric models (Boer et al. 1984; Palmer et al. 1986; McFarlane 1987). This forcing arises when gravity waves are excited at the surface by stable air flowing over irregular terrain; the waves propagate vertically and exert an implicit drag on the large-scale flow. The current version of the Mk3 model uses the gravity wave drag formulation of Chouinard et al. (1986). This drag is dependent on the sub-grid-scale variations in surface topography, and is parameterized by means of a "launching height" (h_e), which is defined to be twice the standard deviation of the surface heights. Following the method used in the parameterization of Palmer et al. (1986), the maximum value of this launching height is limited to 800 *m* in order to prevent two-grid noise near steep mountains. The standard deviations of the sub-grid-scale topography (the variations within a grid square) are shown in Fig. 4. These data were derived from a high-resolution surface height data set.

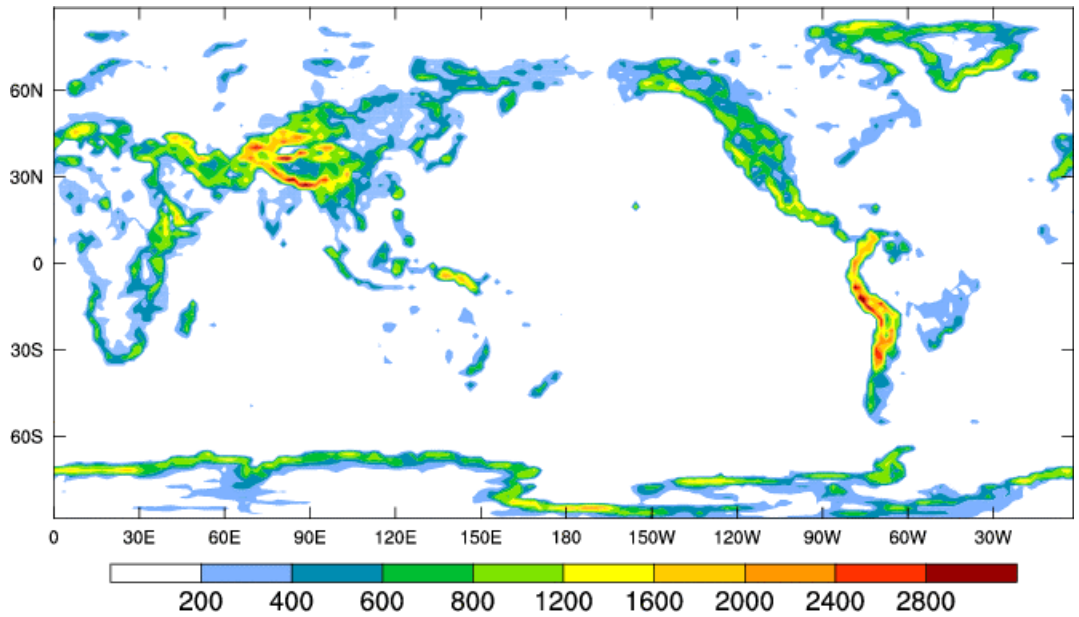

Figure 4. Standard deviations (*m*) of the sub-grid-scale topography.

The gravity wave drag parameterization will be described only briefly. For a full explanation, refer to Chouinard et al. (1986). In this report, the description is given in terms of the hybrid vertical coordinate (η). The gravity wave drag is applied in stable atmospheric conditions ($\partial\theta/\partial z > 0$) only. The momentum flux at the surface (for gravity wave drag) is given by

$$(\underline{\tau}_s)_{gwd} = -\alpha\, h_e\, \rho_s\, N_s\, \underline{V}_s \qquad 11.1$$

where α is a preset constant (0.0075), the subscript s refers to surface values, and N is the Brunt-Vaisala frequency:

$$N = \left(\frac{g}{\theta}\frac{d\theta}{dz}\right)^{1/2}. \qquad 11.2$$

The Froude number is defined by

$$F_r = \frac{N\, h_e}{\mathrm{Y}}\left(\frac{\rho_s}{\rho}\frac{N_s}{N}\frac{\mathrm{Y}_s}{\mathrm{Y}}\right)^{1/2} \qquad 11.3$$

where Y is the projection of the atmospheric velocity on the surface velocity given by

$$\mathrm{Y} = (\underline{V}.\underline{V}_s)/|\underline{V}_s|. \qquad 11.4$$

The frictional change caused by the gravity wave drag is then given by

$$\frac{\partial \underline{V}}{\partial t} = -\lambda_r(\underline{V}_s/|\underline{V}_s|)\,\tilde{\mathrm{Y}}^2 \qquad 11.5$$

where

$$\tilde{\mathrm{Y}}^2 = \mathrm{Y}^2\ \max\{1-\delta\ Fr_c^2/Fr^2,\ 0\}. \qquad 11.6$$

This applies in the region $1 < \eta < \eta_c$ where η_c is a "critical" level, defined as the level at which the wind turning is such that the gravity waves break, and all drag is absorbed at or below that level. Now Y, as defined in (11.4), is positive in the region between the reference level $\eta = 1$ and η_c, but is negative or zero above that level. Fr_c^2 is preset to 0.5. The quantity δ is zero at the top level of the model, and unity below. The parameter λ_r (which has units m^{-1}) is determined by requiring that

$$\int_{z_c}^{z_s} \rho\left(\frac{\partial \underline{V}}{\partial t}\right)_{gwd} dz = -(\underline{\tau}_s)_{gwd} \qquad 11.7$$

where z_s is the surface height. Converting to η coordinates gives

$$\frac{p_s}{g}\int_{\eta_c}^{1}\left(\frac{\partial \underline{V}}{\partial t}\right)_{gwd} d\eta = +(\underline{\tau_s})_{gwd}\ . \qquad 11.8$$

This yields

$$\frac{p_s}{g}\int_{\eta_c}^{1} -\lambda_r\ (\underline{V}_s / |\underline{V}_s|)\ \tilde{\Upsilon}^2\ d\eta = -\alpha\ h_e\ \rho_s\ N_s\ \underline{V}_s \qquad 11.9$$

whence

$$\lambda_r = (g / p_s)\alpha\ h_e\ \rho_s\ N_s\ \underline{V}_s / \int_{\eta_c}^{1} \tilde{\Upsilon}^2\ d\eta\ . \qquad 11.10$$

In order that the above scheme be applied to a flux spectral model, the frictional terms are computed as $\underline{\hat{F}}\cos(\phi)/a$, which for gravity wave drag becomes, using (11.5),

$$p_s \frac{\cos\phi}{a}\left(\frac{\partial \underline{V}}{\partial t}\right)_{gwd} = -\left\{\frac{\lambda_r p_s}{|\underline{V}_s|}\frac{\underline{V}_s \cos\phi}{a}\right\}\tilde{\Upsilon}^2\ . \qquad 11.11$$

Note that the surface velocity component has the requisite spectral weighting, and that the term { .. } is independent of height.

The method of implementing the gravity wave drag is to compute the Υ values, which are prescribed to be zero above the critical level. The θ and $\partial\theta/\partial z$ are used to obtain N and N_s values. From the Froude numbers we obtain

$$Fr_c^2 / Fr^2 = Fr_c^2 / \left(\frac{N^2 h_e^2}{\Upsilon^2}\frac{\rho_s N_s\ \Upsilon_s}{\rho\ N\ \Upsilon}\right) = \left(\frac{Fr_c^2 T_s}{N_s\ \Upsilon_s\ h_e^2}\right)\left(\frac{\Upsilon^3\ \eta^{1-\kappa}}{N\ \theta}\right) \qquad 11.12$$

where $\kappa = R/C_p$. Next the component Υ is computed for all levels, and then the vertical integral of this is computed by

$$\int_{\eta_c}^{1} \tilde{\Upsilon}^2\ d\eta = \int_{0}^{1} \tilde{\Upsilon}^2\ d\eta = \sum \tilde{\Upsilon}_k^2\ \Delta\eta_k \qquad 11.13$$

because $\Upsilon^2 = 0$ for $\eta_c > \eta > 0$. This integral is the denominator for λ_r in (11.10). If there is no generation of gravity wave drag (due to zero h_e value), then this integral is zero and $\lambda_r = 0$.

11.1 Time differencing considerations

The changes to the wind fields due to gravity wave drag are applied similarly to the changes for vertical mixing. That is, new winds are obtained proceeding from timestep $(\tau + 1)^*$ to an actual

($\tau + 1$). This requires an implicit solution of (11.5). Using an effective time interval $2\Delta t$, tendencies are evaluated and actually added in during the calculation of the ($\tau + 2$)* vorticity and divergence.

12 Radiation parameterization (*radfs*)

The radiation code was developed at GFDL (Lacis and Hansen 1974; Fels and Schwarzkopf 1975, 1981; Fels 1985; Schwarzkopf and Fels 1991) and allows for annual and diurnal cycles. The spectrum of radiation is separated into solar (shortwave) and terrestrial (longwave) bands which are treated independently. At each grid-point the code calculates the net radiative heating rate for each atmospheric layer, the radiative energy absorbed by the ground and various shortwave and longwave flux diagnostics, including those determining cloud radiative forcing. These quantities depend on the incoming solar flux at the top of the atmosphere, the atmospheric and surface temperatures, the surface albedo, the cloud layer densities and radiative properties, and the concentrations of water vapour, ozone and carbon dioxide. The cloud cover and the associated cloud optical properties are predicted by the model (see next section).

The incoming solar flux at a grid-point depends on the distance of the earth from the sun and the solar zenith angle. Fixed orbital parameters for the year 1979 are used to avoid any drift in long control experiments. The solar constant is $1367\ W\ m^{-2}$. Ozone concentrations are specified as a function of latitude, pressure and month from the AMIP II recommended dataset (Wang et al. 1995). The ozone is interpolated in time and pressure each radiation step. In experiments that include the effect of secular ozone changes a different input file can be used for each year. In the model control experiments the carbon dioxide concentration is assumed constant at 330 ppmv. Radiative effects of other minor gases such as methane, nitrous oxide and CFCs are not included explicitly. Effects of changes in their concentrations can be included approximately in climate change experiments by means of equivalent CO_2. The other inputs to the radiation code, including the cloud amounts, depend on the atmospheric and surface state.

For both the longwave and shortwave bands the atmosphere is assumed to consist of homogeneous, plane parallel layers with interfaces at the half-levels. The radiative fluxes for both upward and downward directions perpendicular to the layers are calculated for each interface including the ground and the top of the atmosphere. The cooling rate of a layer is the net flux divergence divided by its heat capacity.

12.1 Shortwave code

The shortwave code is based on the Lacis and Hansen (1974) (hereafter L&H) approach. It includes the Ramaswamy and Friedenreich (1992) improvements to the water vapour absorption. A complete calculation of shortwave radiation must consider for each wavelength both the direct solar beam and the diffuse component due to Rayleigh scattering by the air molecules and scattering by the clouds and earth surface. In the model, approximations are made so that only the perpendicular components of the diffuse radiation need be calculated. Furthermore, the shortwave spectrum is divided into twelve bands within which the radiative properties are taken as uniform. The first band covers the ultraviolet and visible wavelengths. The other eleven cover the near infrared. These are derived from an exponential sum fit to the water vapour absorption and so cannot be assigned separate individual wavelengths. The band weights are given in Table 6 (sorted in order of increasing water vapour absorption strength).

Band number	Relative weight
1	0.500000
2	0.121416
3	0.069800
4	0.155800
5	0.063100
6	0.036200
7	0.024300
8	0.015800
9	0.008700
10	0.001467
11	0.002342
12	0.001075

Table 6. Shortwave bands and relative weights

The code first calculates the optical depths for each layer and band, as described below. The transmission and reflection rates or functions for each band are then calculated, using the "adding method" described by L&H. Allowance is made for the effects of the cloud layers and the surface. The relative fluxes at each interface are then determined. These are summed, with the appropriate weights, to give the net fluxes and hence the net heating rates and diagnostics. The heating rates for layers within a "thick" cloud are assumed to be constant.

Ozone is assumed to affect only band 1 which covers the ultraviolet (approximately $0.1\ \mu m$ to $0.4\ \mu m$) and visible ($0.4\ \mu m$ to $0.7\ \mu m$) wavelengths; band 1 contains half the total incoming flux. A weak absorption of the band by H_2O is included but none by CO_2. For band 1 the approximation is made that the atmosphere acts as an absorbing layer on top of a reflecting layer, which is the topmost cloud or the ground in the case of clear skies. Since the wavelength dependence of Rayleigh scattering makes it negligible for the other bands, the calculation of transmission functions of all bands for a cloud-free layer depends only on the optical path of the layer.

The optical path across a layer is the mass of absorbing gas in the layer magnified by a factor. For the downward path for all bands the factor above the top cloud or surface layer is given by Equ. (12) of L&H and accounts for the slant angle and the refraction of the incoming beam. The surface is assumed to be a Lambert reflector so that the upward radiation, except for band 1, is uniformly diffuse. A diffusivity factor of 5/3 is used to scale the absorption path lengths. For band 1 L&H find that the combined effects of Rayleigh scattering and reflection are best accounted for with a factor of 1.9. Below a non-zero cloud layer (regardless of cloud amount) these same factors are used for radiation in both directions.

As a function of the optical path, the ozone absorption in band 1 is twice that given in Equ. (10) of L&H. The doubling is because Equ. (10) refers to the absorption of the total shortwave flux, whereas band 1 accounts for only half the flux but all the ozone absorption. Similarly, the absorption by CO_2 in each of the eleven near-infrared bands is given by twice the net absorption given by Sasamori et al. (1972). The only property varying across the infrared bands is the absorption by H_2O. For each band the absorption for CO_2 is given by $\{1-\exp(-k_a y_p)\}$ where

y_p is the optical path and k_a the constant absorption coefficient for the band. It is assumed that the absorption by two gases is given as the product of the two individual values.

The albedo of the earth surface α_s is the same for each band. It depends on surface type. The surface albedo for land with and without snow cover has been detailed in Section 9 (soil and snow parameterizations). For sea points the albedo depends upon zenith angle ξ_a, and is given by $\alpha_s = 0.05/(0.15 + \cos(\xi_a))$. For sea-ice without snow cover, $\alpha_s = 0.65$, or 0.55 if $T_s > 273\,K$ (melting ice condition). For sea-ice with snow cover, $\alpha_s = 0.80$, or 0.70 if $T_s > 273.15\,K$ (melting snow on ice condition).

The net surface reflectivity for band 1 is given by combining the earth surface value with the reflectivity due to Rayleigh scattering using Equ. (15) of L&H. This scattering depends on the solar zenith angle via Equ. (18) of L&H. Although Equ. (18) of L&H was derived for clear-sky conditions it is also used under cloud in the code.

The direct radiative effect of sulfate aerosol can be included in the model via a perturbation of the surface albedo, following Mitchell et al. (1995). The true vertical profile of the sulfate scattering is replaced by a notional single scattering layer just above the surface. The net albedo of the two surfaces can be simply calculated , including the effect of multiple reflections. The radiation code does not calculate separate direct and diffuse beams so the perturbation is applied to the total flux. The albedo perturbation is

$$\delta\alpha_s = \beta\alpha(1-\alpha_s)^2 S/\cos(\xi_a) \qquad 12.1$$

where S is the vertically integrated sulfate mass (kg/m^2), ξ_a is the solar zenith angle and the parameters $\beta = 0.29$ and $\alpha = 8.00$ are the same as in Mitchell et al. (1995).

12.2 Longwave code

The atmosphere is itself a source of longwave radiation, not just an absorber and scatterer as it is for shortwave. The longwave code is therefore considerably more complicated. The Mk3 atmospheric model uses the longwave radiation parameterization developed by Fels and Schwarzkopf at GFDL. The development of this code is described in Fels and Schwarzkopf (1975, 1981), and Schwarzkopf and Fels (1985, 1991).

The longwave radiation code covers the frequency range $0 - 2200\ cm^{-1}$ (wavelengths longer than $0.45\ \mu m$). The processes included are absorption by the vibrational and rotational lines of water vapour, carbon dioxide and ozone, and the water vapour continuum absorption. The frequency ranges for each of these processes is shown in Table 7. Note that in Table 7, H_2O means water vapor line absorption only. For more details of the band structure used in the radiation code and of the particular approximation used (the "Simplified Exchange Approximation"), see Schwarzkopf and Fels (1991). The remainder of this section describes details of the implementation particular to the CSIRO model only.

Bands (cm^{-1})	Wavelength (μm)	Main absorbers	Minor absorbers
0-400	> 25	H_2O	
400-560	18-25	H_2O	Continuum
560-800	12.5-18	H_2O, CO_2, continuum	O_3
800-990	10.1-12.5	continuum	H_2O
990-1070	9.3-10.1	continuum, O_3	H_2O, CO_2
1070-1200	8.3-9.3	continuum	O_3
1200-2000	5-8.3	H_2O	

Table 7. Bands used in the model for longwave absorption, following Schwarzkopf and Fels (1991).

The CO_2 amount is approximately uniformly distributed in the atmosphere and so detailed pre-computed transmission functions can be used. Transmission coefficients for CO_2 concentrations of 165, 330, 660 and 1320 ppmv of CO_2 were supplied by GFDL for a high resolution vertical grid. For use in the model, these coefficients were interpolated to the model vertical levels. These transmissions are calculated for two surface pressures and three temperature profiles. The interpolation method of Fels and Schwarzkopf (1981) allows calculation of accurate transmission coefficients for the actual temperatures and pressure of each model column. It is also possible to derive transmission coefficients for any desired concentration of CO_2 (Schwarzkopf and Fels 1985) via interpolation, though the standard model runs have used 330 ppmv.

The distributions of both ozone and water vapour vary in both space and time (though the variation of ozone is prescribed as noted earlier) and this pre-computation is not possible. For these gases a random band model is used. This calculation includes the temperature variation of the absorption.

12.3 Clouds

The radiation code allows for any number of cloud layers, and the cloud top and bottom for each layer can be specified separately. This allows thick clouds that fill more than one model layer or single layer clouds (by setting the top and bottom to be equal). However, cloud top and base must each correspond to a model level and cannot be set to an arbitrary pressure. The current cloud scheme allows for clouds at any level, except for the level adjacent to the ground (the model does not allow for fog). The separate cloud layers are assumed to be randomly overlapped. For single-level clouds, the cloud top and bottom temperatures are both equal to the temperature at the model level. In a multi-level cloud the heating rate is calculated from the fluxes at the cloud top and bottom and is constant through the depth of the cloud.

12.4 Modifications to the radiation code

A full radiation calculation is done every 2 hours (8 model timesteps at T63 resolution), with the atmospheric heating rates held constant between these times. There is consequently a jump in the heating rate whenever a full radiation calculation is done, primarily due to the diurnal variation of solar radiation at the top of the atmosphere. This causes no problems in the free atmosphere but the surface energy balance is rather more sensitive. There are two additional steps taken at

the surface to smooth the diurnal cycle of net radiation. The downward longwave flux at the surface is held constant over the 2 hours but the upward longwave flux (the T_s^4 term) varies with the surface temperature each step. The solar radiation incident at the surface is smoothed by interpolating the variation of the solar zenith angle, assuming that the sun angle is the only quantity varying. This process does not affect the time-integrated radiation.

The original GFDL code assumed that the model half-levels (or layer interfaces) were midway between the levels. In the CSIRO atmospheric spectral models the reverse is true and the calculation of the temperature and pressure at the half-levels was changed appropriately.

In order to obtain cloud forcing diagnostics, the longwave code was modified to do a clear sky calculation along with the usual calculation. This gives the so-called method II cloud radiative forcing (Cess and Potter 1987) at little extra cost (approximately 2%). The effect of clouds is not as easily separated in the shortwave code and so this code must be repeated with the cloud set to zero for the diagnostics. However, the cloud free calculation takes only about half the time of a typical cloudy calculation. Overall the diagnostic cloud forcing calculation (optional) adds about 20% to the cost of the radiation calculation.

13 Stratiform cloud and precipitation

A detailed description of the stratiform cloud scheme and its evaluation has been given by Rotstayn (1997, 1998) and Rotstayn et al. (2000). Here, we give an overview of each routine, and give details of aspects that differ from the original implementation as described in the above papers. Note that the convection scheme (see Section 14) generates convective (cumulus) cloud amounts, and the convection scheme also generates detrained liquid water that is used subsequently by the stratiform cloud scheme described here.

13.1 Interface (*progcld*)

Before the cloud microphysical routines are called from *progcld*, the temperature and moisture values are calculated for the part of each grid box that lies outside the convective cloud that has previously been diagnosed by the convection scheme. This is to avoid "double counting" of convective cloud as stratiform cloud in *newcloud*. The cloud fractions generated by the stratiform-cloud and convection schemes are combined together for passing to the radiation scheme. A weighted average is taken of the cloud water contents to give an overall value appropriate to the grid box as a whole. Distributions of cloud-droplet number concentration are also set up, using relation D from Boucher and Lohmann (1995), which takes as input the sulfate distributions generated by the GRANTOUR model (Penner et al. 1994). These are used in the calculation of stratiform rainfall by autoconversion, and in the calculation of droplet effective radius that is used by the radiation scheme.

Figure 5 gives an overview of the microphysical processes that are treated by the cloud scheme. The three prognostic variables are water vapour mixing ration (q_V), cloud liquid water mixing ratio (q_L) and cloud ice mixing ratio (q_I), shown in the upper part of the figure. Other processes not shown in the figure are transport by semi-Lagrangian advection and convective and turbulent mixing, and the interactive calculation of cloud radiative properties.

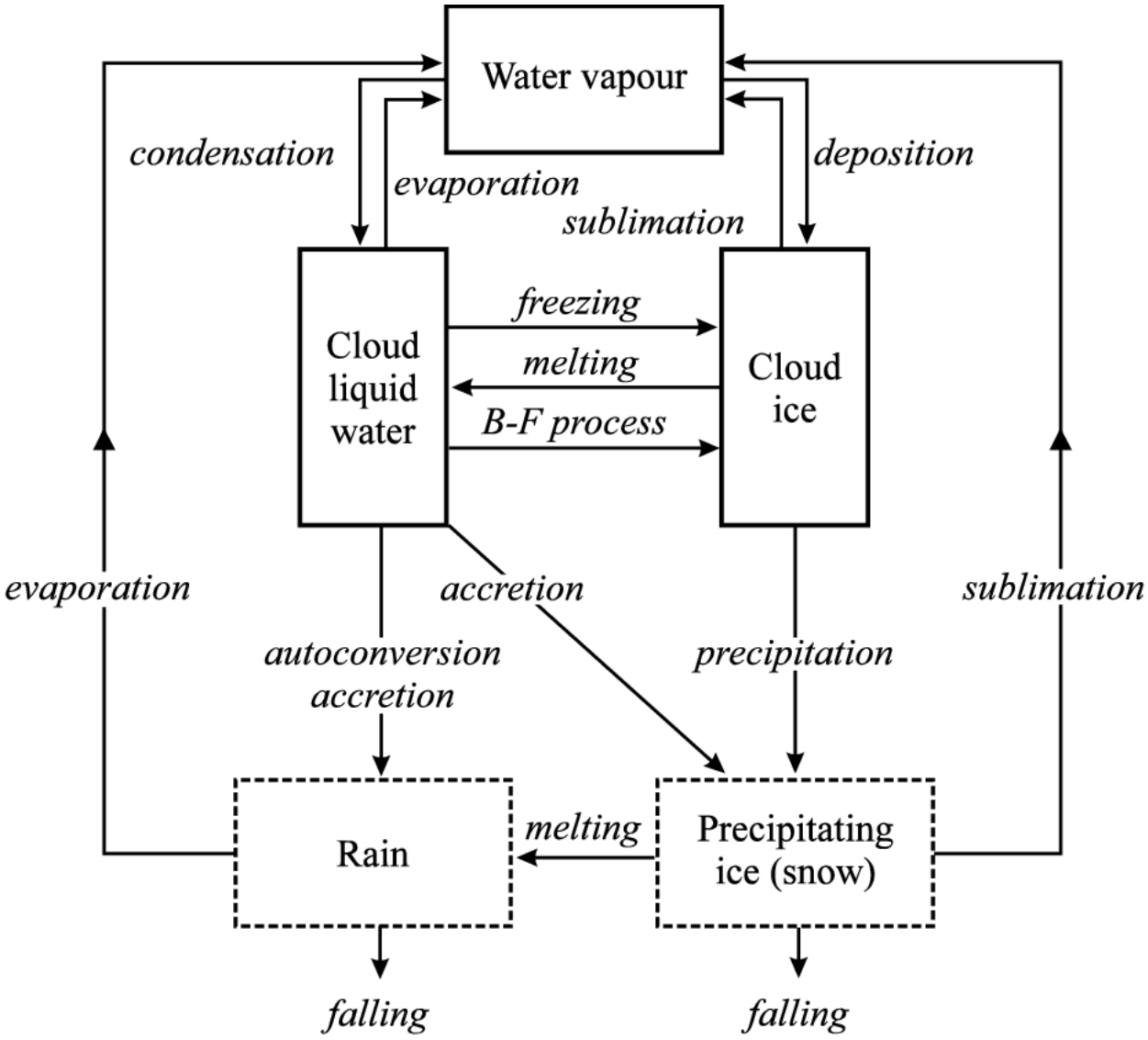

Figure 5: Overview of the microphysical processes treated by the stratiform cloud scheme.

13.2 Cloud formation and mixed-phase clouds (*newcloud*)

The conversion terms between the three prognostic variables (shown in the upper part of Fig. 5) may be loosely described as "cloud formation and dissipation". These are handled by a condensation scheme that uses an assumed sub-grid distribution for the total moisture in each grid box, and calculates as output the cloud fraction and cloud water mixing ratio ($q_C = q_L + q_I$). Details are as given by Smith (1990). In practice, the cloud amounts generated by the scheme are rather sensitive to the critical relative humidities that control the onset of cloud formation. Above the lowest two layers, the model currently uses critical relative humidities of 85% over ocean and 75% over land, with smaller values in columns in which moist convection occurs. In layers 1 and 2, the critical relative humidities are 99% and 95% respectively. One goal of current research in cloud parameterization is to replace these parameters with more physically based treatments of sub-grid moisture variability (e.g., Cusack et al. 1999).

The "B-F process" in the center of the figure refers to the model's calculation of the liquid fraction in mixed-phase clouds, i.e., the breakdown of q_C into q_L and q_I. Most earlier cloud schemes in GCMs have simply prescribed this fraction as a function of temperature, but this means that models are unable to capture the temporal evolution of cloud systems, because condensation occurs initially as liquid water, which then evaporates as ice crystals grow at their expense by vapour deposition. The updated treatment of mixed-phase clouds described by Rotstayn et al. (2000) treats this process explicitly, by assuming that condensation that occurs initially as liquid water is replaced by ice crystals that grow at the expense of the water droplets, at temperatures between $0°C$ and $-40°C$. Conversion rates appropriate to different ice crystal habits can be used by the scheme, with the standard version following the assumption of spherical ice crystals, as given by Equ. (17) of Rotstayn et al. (2000).

13.3 Precipitation (*newrain* and *icefall*)

During the development of the scheme, considerable care was taken to include physically based treatments of these processes as far as possible. A detailed derivation and discussion of the parameterizations is given by Rotstayn (1997). The sub-grid nature of precipitation is accounted for, based on the assumption that clouds are randomly overlapped in the vertical. Autoconversion refers to the growth of cloud droplets into precipitating drops by collision and coalescence. Precipitation of liquid water occurs by autoconversion, and accretion by falling rain and snow. These three processes are handled by Equ. (15), (22) and (29) of Rotstayn (1997). Evaporation of falling rain generates water vapour, as does sublimation of falling snow. These are handled by Equ. (23) and (30) of Rotstayn (1997). Precipitation of cloud ice to form falling ice (loosely, snow) is calculated from the flux divergence of an empirically based fall speed for ice crystals V_I, as given by Equ. (25) of Rotstayn (1997). The original scheme used a fall speed based on observations from Heymsfield (1977), whereas in the Mk3 model, the fall speed relation is based on data from Wu et al. (1999), namely

$$V_I = 2.05 + 0.35 \log 10(q_I / C_I) \qquad 13.1$$

where q_I / C_I gives the in-cloud mixing ratio of cloud ice. A minimum fall speed of $0.1\, m\, s^{-1}$ is imposed. The scheme from Wu et al. (1999) gives somewhat smaller fall speeds, and hence larger high cloud amounts, compared to the scheme from Heymsfield (1977).

13.4 Cloud radiative properties (*cloud2*)

The model's radiation scheme is configured for fixed, height-dependent radiative properties, but for consistency with the updated cloud treatment it is desirable to use variable radiative properties, as in other modern GCMs. The treatment of cloud radiative properties (previously calculated in *cloud* for fixed cloud properties) was therefore modified (*cloud2*) to take the cloud liquid water and cloud ice mixing ratios from the cloud microphysical scheme as input. The *cloud2* routine now calculates the shortwave reflectivities and absorptivities and the longwave emissivities interactively. In a more modern radiation code, the radiation scheme would normally take the cloud optical depth, single scatter albedo and asymmetry parameter as input, and calculate the cloud radiative properties within the radiation scheme itself, so the current treatment is best regarded as an interim measure.

The shortwave properties are calculated following Slingo (1989) for liquid-water clouds, and a similar scheme for ice clouds (Francis et al. 1994). Both schemes use the delta-Eddington approximation to calculate the shortwave properties for four bands, which are then averaged to give the properties for the two broad bands in which the model's shortwave cloud radiative properties are specified. These two broad bands cover the 12 shortwave bands referred to in Section 12.1. Both schemes require as input parameters the liquid (or ice) water path and the effective radius R_e. The liquid and ice water paths are provided by the cloud scheme; the values passed to the radiation scheme are taken as averages of those generated by the cloud scheme before and after the calculation of precipitation, and are also averaged over several model timesteps, since the radiation scheme is called just once every two model hours. For liquid-water clouds, R_e is specified as a function of liquid water content and droplet concentration following Martin et al. (1994). As in the autoconversion scheme, the droplet concentration is estimated empirically from sulfate distributions generated by the model of Penner et al. (1994). To account for sub-grid variability of cloud properties, the cloud optical depth is reduced relative to its plane-parallel value as described by Rotstayn (1997).

The longwave emissivities for ice and liquid-water clouds are calculated following the method described in Rotstayn (1997), which has been modified for the Mk3 model to include the emissivity formulation due to Sun and Shine (1994). To help ameliorate an upper tropospheric cold bias in the tropics in the model, a minimum emissivity of 0.7 is applied, though this should again be regarded as an interim measure.

14 Cumulus convection (*convukmo, cvmix*)

The cumulus convection parameterization in the standard version of the Mk3 model is based on that used in the Hadley Centre model, and is described in Gregory and Rowntree (1990). The convection code was kindly supplied by the U.K. Meteorological Office. This convection scheme (denoted now by *UKMO*) generates updraughts and downdraughts, with entrainment and detrainment of cloud/environment air. It also provides convective cloud amount, and the liquid water amount within the convective clouds. There is cloud top detrainment of liquid water and/or ice from the cumulus convection, and these are subsequently used by the cloud microphysics scheme (Section 13). There is an interface subroutine *convukmo* to the *UKMO* package of subroutines (contained in *ukall.f*), which contains a tree structure for the *UKMO* convection scheme.

In addition to the *UKMO* convection, the Mk3 model also has two alternative convection schemes. These are the modified Arakawa (1972) "soft" moist adjustment scheme (subroutine *conv*) as described in McGregor et al. (1993) and the Kuo (1974) convection scheme (subroutine *hkuo*). However, the Mk3 model has been developed so as to make use of the *UKMO* convection scheme generating liquid water amounts, which ties in with the cloud microphysics scheme. This is not readily done with the alternative convection schemes in which the implied convective cloud liquid water amount has to be prescribed. These schemes have remained as optional components of the Mk3 code for comparison of model results using alternative convection schemes. (The model coding allows only one convection scheme to operate at one time.)

Before the use of the *UKMO* convection, the atmosphere is adjusted for any dry instability. (This adjustment is also required to be carried out before the use of the Arakawa mass flux scheme for numerical stability reasons). However, the boundary layer in the atmosphere is often observed to

be in a state of having some dry instability present (as happens in the model following vertical mixing, which does not entirely remove dry instability). Thus the removal of any dry instability is only carried out before the convection parameterization step (for numerical stability), and the original amount of dry instability is *reinstated* following the convection step.

The presence of dry instability is determined through the dry static energy (S) defined by

$$S = C_p T + \phi \qquad 14.1$$

where $\phi = gz$ is the geopotential height. The atmosphere is deemed dry unstable if $\partial S / \partial p > 0$, i.e. if $(S_k - S_{k+1}) / C_p > 0$. To derive the latter, we require $(\phi_k - \phi_{k+1})$, which is obtained from the hydrostatic equation in the form $\partial \phi / \partial \ln(p) = -RT$. The atmosphere is adjusted to just above neutral conditions, while maintaining conservation of energy.

The convection parameterization (*UKMO* or Arakawa mass flux) generates a convective mass flux M_p. See Gregory and Rowntree (1990) for the derivation of M_p in the *UKMO* scheme, which is the standard convection parameterization for the Mk3 model. (The derivation for the Arakawa mass flux convection as used in the Mk2 model is given in McGregor et al. (1993)). The convective mass flux allows for the inclusion of convective mixing of momentum (subroutine *cvmix*). The mass flux M_p (generated at model full levels) is used in an adjacent-level mixing process. The convective momentum mixing may be parameterized in the form:

$$\left(\frac{\partial \underline{V}}{\partial t}\right)_k^{conv} = (M_p)_k \left(\frac{\partial \underline{V}}{\partial \eta}\right)_k . \qquad 14.2$$

However, for stability the convective momentum mixing is implemented in the Mk3 model by means of an implicit method, which uses a tri-diagonal solver in a manner similar to that used for turbulent vertical mixing. The turbulent vertical mixing (see Section 10) is carried out using an equation of the form

$$2\Delta t \left(\frac{\partial \underline{V}}{\partial t}\right)_k = -A_k (\underline{V}_{k-1} - \underline{V}_k) + C_k (\underline{V}_k - \underline{V}_{k+1}) . \qquad 14.3$$

For convection mixing using an implicit method we thus define

$$A_k = -f_{k-1,k} / (2\Delta \eta_k) \qquad 14.4$$

$$C_k = -f_{k,k+1} / (2\Delta \eta_k) \qquad 14.5$$

where

$$f_{k,k+1} = -(2\Delta t)[(M_p)_k + (M_p)_{k+1}] / 2 . \qquad 14.6$$

In modelling terms, the vertical mixing is not applied directly to the velocity fields, but is computed as part of the stress tendencies. Momentum is conserved by the formulation, whilst kinetic energy is reduced.

15 Frictional heating

In order for the climate model to conserve energy, the dissipation (frictional/turbulent) of kinetic energy in the model must be fully accounted for. This energy loss is converted to a heating source term, and is applied as an adjustment to the temperature during the evaluation of the physical processes. The kinetic energy (KE) change is computed from

$$\frac{\partial KE}{\partial t} = u\left(\frac{\partial u}{\partial t}\right)_{fr} + v\left(\frac{\partial v}{\partial t}\right)_{fr} \qquad 15.1$$

where the subscript " *fr* " denotes the combined dissipation effects, which include horizontal diffusion, vertical mixing (including convective mixing), surface drag, and gravity wave drag.

As mentioned earlier, the model retains the time tendencies for the vorticity and divergence equations due to the inclusion of spectral horizontal diffusion (see Section 17 for horizontal diffusion details). From these we can calculate the equivalent tendencies for U and V. This is because it is straightforward in spectral models to derive the spectral components of the U and V fields from the vorticity ξ and velocity potential χ. Thus the same method can be used to derive the diffusive tendencies of U and V from the diffusive tendencies of ξ and χ. These spectral diffusion components are stored, and transformed during the subsequent timestep onto the "physics" grid, and then added to the other frictional stresses mentioned above. The complete frictional dissipation of energy can be calculated and added as part of the thermodynamic heating. For the 18 level, T63 AGCM the global mean frictional heating is about 1.1, 0.3, and 0.15 $W\,m^{-2}$ for model levels 1, 2, and 3 respectively (see Table 1), and less than 0.1 $W\,m^{-2}$ for other model levels.

16 Non-linear dynamics (*dynm, dynmnl, dynmst, dynmvo*)

Following the Physics transform loop, the Dynamics loop is used to spectrally synthesize the non-linear advection tendencies (see model flow diagram in Fig. 1). The grid-point values transformed from spectral space are: the vorticity ($\hat{\xi}$), the divergence ($\hat{D}$), the temperature ($\hat{T}$), and the gradients of surface pressure. The physically adjusted water vapour mixing ratio (q) is already available in grid form, and the values of $\hat{U}, \hat{V}$, p_s have been held in grid form from the Physics loop. The standard spectral methods for evaluating the gradients of products are used.

Details are given in Appendix B on the methods used to form the "*dynamical core*" of the atmospheric model equations. The equations are now formulated using a hybrid vertical coordinate. The main temperature prognostic variable now incorporates a pressure dependency, and the temperature/geopotential terms common to the momentum equation and the temperature equation use virtual temperature. It is essential that the principle of conservation of energy be adhered to in climate-length integrations, and it can be shown that the flux form of the spectral equations formally conserves both energy and mass. When applying these equations in the

discrete form, care must be taken to ensure that total energy is conserved exactly. Details of these requirements have been given in McGregor at al. (1993).

Briefly, it can be shown that for energy to be conserved, the half level values of $U_{k\pm0.5}$, $V_{k\pm0.5}$ must be taken as the average of the adjacent full-level values regardless of the thickness of the model η levels. On the other hand, the temperature and moisture equations have no such restriction on half-level values used in the $\eta\dot{}$ vertical motion terms. Thus the T and q half-level values are derived by η level interpolation. The geopotential heights also require appropriate treatment. The hydrostatic equation (from Appendix B, Equ. (26.31)) has the form

$$\tilde{\phi} = \int_{p}^{p_s} \frac{R\tilde{T}}{p}\, dp = \int_{\eta}^{1} R\tilde{T}\, \frac{\mu\eta}{p}\, d(\ln\eta) = \int_{\eta}^{1} R\tilde{T}_N \; d(\ln\eta)\,. \qquad 16.1$$

The vertical profile of the temperature variable $\tilde{T}_N = \tilde{T}\,\frac{\mu\eta}{p}$ (in which $\mu\eta / p \approx 1$) is assumed to be of the form

$$\tilde{T}_N = \alpha + \beta \ln(\eta)\,. \qquad 16.2$$

The hydrostatic equation is integrated from the surface up, as a function of $\ln(\eta)$, using the piecewise log-linear expression, Equ. (16.2), to give the half-level values of ϕ. For the top level, the actual integrated value of ϕ is used. For all lower levels these half-level values are then averaged to derive the necessary full-level values by means of

$$\phi_k = (\phi_{k-0.5} + \phi_{k+0.5})/2\,. \qquad 16.3$$

Note that these ϕ_k values (derived by averaging half-level values) must be used if energy conservation is to be guaranteed for heights derived from a $\ln(\eta)$ temperature profile. Whilst the heights are very similar to the full-level values that would be obtained directly by piecewise integration, in general they are not identical.

During the Dynamics loop, some grid-point forcing terms computed during the Physics loop are added to the non-linear dynamical terms for spectral synthesis. This method avoids having additional synthesis during the Physics loop. The terms so added are the atmospheric stresses that have been computed as tendencies for the divergence and vorticity equations. For stability, these terms are backward in time, and are obtained from storage arrays by rotation of indices. The spectral fields evaluated during the Dynamics loop are the non-linear part of the time tendencies for temperature, vorticity, and divergence. The kinetic energy based term $\hat{E}$, as defined in Appendix B, is also evaluated spectrally so that $\nabla^2\hat{E}$ can be added later to the divergence tendency (*linear*).

There is an optional implicit treatment of the spectral vorticity available (subroutine *dynmvo*). This is incorporated to help ensure numerical stability in the model for high wind speeds. Details about the application to the spectral equations are available in Appendix B. It is a standard option for the Mk3 atmospheric model, and is formulated to apply in the model stratosphere only.

Statistics about the behaviour of the model dynamical fields are collected during the Dynamics loop (*dynmst*). These statistics are gathered on preset pressure levels. Now the atmospheric model vertical coordinate is a terrain following coordinate, and is dependent upon surface pressure. Thus in order to generate statistics at a given pressure level (e.g. temperature at 500 *hPa*) requires that there be vertical interpolation. This is computationally somewhat expensive, and is carried out about every ¼ day. The sampling is such that over the course of a model month, all times of the day are included in the statistics. Due to the fact that the statistics are on preset pressure levels in the vertical, there will be data voids for pressure levels that lie inside mountains.

17 Time integration and temporal smoothing (*semii, assel, jmcgslt*)

This section outlines the time integration of the main atmospheric variables. These are the spectral temperature, divergence, vorticity and surface pressure fields, and the grid-point moisture field. The other variables associated with the surface processes that require time integration have already been described in previous sections.

A leapfrog time integration scheme is used for the main atmospheric fields. Thus two time levels of the main prognostic variables are retained. The divergence, temperature, and surface pressure equations are coupled linearly by gravity wave generation terms. A semi-implicit treatment of the gravity wave terms is used, to enable the model to utilize long timesteps (15 minutes at resolution T63). It is facilitated by the fact that the ∇^2 terms in the divergence equation have a simple solution when converted to spectral form (e.g. $\nabla^2 p_s$ becomes $-l(l+1)(p_s)_l^m / a^2$ in spectral form). Full details of the derivation of the set of coupled equations are given by Gordon (1981). The general method for such a treatment can be found in Bourke (1974). The remaining prognostic variables of vorticity (spectral) and moisture (grid-point) do not entail a semi-implicit time algorithm.

Because of the use of a leapfrog time integration scheme, the solution will tend to become de-coupled at odd and even timesteps. To help prevent this, a weak time filter of the Robert (1966) type is applied to temperature, vorticity, divergence, moisture, and surface pressure. The form of this filter for a variable, say μ, is

$$\mu(\tau)' = (1-2F)\mu(\tau) + F(\mu(\tau+1) + \mu(\tau-1)) \qquad 17.1$$

where $\mu(\tau)'$ is now the smoothed value at timestep τ, performed after τ+1 fields have been evaluated. The value of F is set at 0.05 .

In the case of the temperature and moisture fields this time filter is applied in two stages. This is due to the fact that the predicted values of moisture and temperature at timestep (τ + 1) are not yet adjusted for the effects of rainfall, latent heat release etc., whereas the (τ) and (τ - 1) components are fully adjusted. Thus a partial correction is first made to these fields following time integration by excluding the (τ + 1) component. This missing part is added later during the next timestep following all physical adjustments to these fields (subroutine *assel*).

18 Horizontal diffusion (*diffn*)

Horizontal diffusion is necessary in climate models to prevent an unrealistic build-up of amplitude of the highest wavenumber coefficients. It is included as a crude representation of the effects of sub-grid-scale motions. Horizontal diffusion is only applied to the temperature, vorticity and divergence. The surface pressure (p_s) is not diffused. The moisture fields (grid point) do not have horizontal diffusion applied directly because of the use of the semi-Lagrangian transport (SLT) method for horizontal advection. (SLT uses cubic splines to evaluate departure points which have some implied diffusion of high wavenumbers.) The spectral diffusion is applied directly in a simplified form as part of a split time integration scheme; it is applied as an adjustment following the main time integration.

For the temperature, T, the method for implementing horizontal diffusion is derived in Appendix B (Section 26.5). Some simplifications are incorporated that allow for ease of application in spectral terms, and the final system is represented by

$$\frac{\partial \hat{T}}{\partial t} = \sim + K_H \nabla_\eta^2 \hat{T} - K_H Fn(\overline{T}) \nabla_\eta^2 p_s \qquad 18.1$$

where $Fn(\overline{T})$ is used to denote a function of global mean temperatures (see Equ. (26.82) in Appendix B).

This may be compared to the form as used in earlier versions of the CSIRO atmospheric model (see McGregor et al. 1993) in which the model temperature variable was given by $\hat{T} = p_s(T - T_0)$ and the model had $\sigma = p / p_s$ as the vertical coordinate. In that case, the diffusion equation was given by:

$$\frac{\partial \hat{T}}{\partial t} = \sim + K_H \nabla_\sigma^2 \hat{T} - K_H \left\{ (\overline{T} - T_0) + \frac{\partial \overline{T}}{\partial \ln(\sigma)} \right\} \nabla_\sigma^2 p_s \,. \qquad 18.2$$

Upon inspection of (typical) model values, it is found that the coefficient multiplying $\nabla^2 p_s$ in Equ. (18.1) is zero for the top two model levels, and is considerably smaller than the coefficient in Equ. (18.2) for other model levels. Thus the latter term involving $\nabla^2 p_s$ has been made optional in the Mk3 model, and is currently *excluded* in the Mk3 code when using the Simmons-Chen temperature variable. Note that the expression for diffusion can be applied directly in spectral form because of the simple ∇^2 conversion (see previous section).

The temperature diffusion is evaluated as part of a split time scheme. First, the component involving p_s (if not excluded) is added as an adjustment to the current value of $\hat{T}$. Secondly, the $\nabla^2 \hat{T}$ term is applied as a forward implicit adjustment for stability. This diffusion is only applied to a selected part of the spectrum. The particular part of the spectrum depends upon the model resolution. For the R21 model it is the upper half of the rhomboid. For the T63 model it is the upper part of the triangle defined as follows. The T63 model wave resolution is 0:63 (i.e. $MW = 63$ where MW stands for the total meridional wave number). In spectral terms the variables are denoted by e.g. $\hat{T}_l^m$ with $\{ m = (0, MW);\ l = (m, MW) \}$. The diffusion is then

applied to the "upper 1/8" of the triangle. We define $MW8 = \{MW - (MW+1)/8\}$, and thus incorporate diffusion in the region defined by $\{ m = (0, MW);\ l = (\max(0, MW8 - m), MW) \}$. The diffusion coefficient is $K_H = 2.5x10^5\ m^2\ s^{-1}$.

The diffusion of vorticity $\hat{\xi}$ and divergence $\hat{D}$ assumes the standard form (see, for example, Bourke 1974) and (for ease of application) is applied directly to the pressure weighted stream function $\hat{\psi}$ and velocity potential $\hat{\chi}$ values on η surfaces without attempting to correct for any μ (or p_s) weighting effects. Again, the diffusion affects only parts of the spectrum depending upon resolution (see above), and is also evaluated as an implicit forward adjustment for stability. In order to maintain realistic stratospheric wind speeds, and to assist with computational stability, especially when the stratospheric jet stream attains its peak value in winter in the SH, the application of $(\hat{\xi}, \hat{D})$ diffusion is modified as follows. For the Mk3 atmospheric model with 18 vertical levels, the top two levels (k = 17 and k = 18) have increased K_H, with factors of 1.25 and 2.5 respectively. In addition, for these top two levels, the $(\hat{\xi}, \hat{D})$ diffusion is allowed to operate over the entire spectrum.

The implied time tendencies for the stream function and velocity potential are evaluated and retained, and are used later to obtain the equivalent tendencies for the U and V components. These latter values are used during the physical adjustments as a source of frictional heating to the atmosphere.

18.1 Alternative horizontal diffusion operator

There is an alternative method for the application of diffusion in the Mk3 model. This is based on the horizontal eddy diffusion parameterization of Frederiksen and Davies (1997; hereafter FD), which was determined self-consistently from barotropic closure theory for observed atmospheric spectra. Full details of the implementation within the Mk 2 AGCM are given in the report by Frederiksen et al. (2000). Briefly, the FD-parameterization replaces the spectral form of the Laplacian dissipation operator by a function $MW(MW+1)\,G^+\{ l / MW \}$ where G^+ is the positive part of the net dissipation function in Fig. 1a of Frederiksen et al. (2000). Their dissipation function is slightly negative at low and particularly intermediate wavenumbers and then rises rapidly to a positive cusp at the highest wavenumber. They found that including or excluding the small negative part made little difference in their simulations. The diffusion coefficient is given by $K_H = 4.92x10^5\ m^2\ s^{-1}$ for the FD-diffusion parameterization.

19 Sea-ice model

The sea-ice model in the Mk3 model contains both ice dynamics and ice thermodynamics. The model grid points with sea-ice are also allowed to have part ice cover and part open water (i.e. leads/polynyas), with the ratio changing according to local conditions. The inclusion of leads is very important because it allows a better representation of the turbulent heat fluxes from the ocean to the atmosphere. The turbulent fluxes decrease rapidly in magnitude when only a thin ice cover is present, and when the ice cover is greater than $1\,m$ thick, almost all the heat exchange is through the leads. Hence even a small fraction (less than 5%, say) of open water can dramatically alter the heat exchange with the atmosphere and increase the surface air temperatures (Maykut

1986). The inclusion of an open water fraction also allows for a better representation of the mixed albedo of the surface.

An additional benefit arising from the inclusion of leads is related to the response of the combined atmosphere-ocean-ice model under changing climate conditions (for example enhanced greenhouse warming). The polar research community has suggested that the inclusion of leads would reduce the (expected) greenhouse signal at high latitudes. This follows from the decreased contrast between the combined ice-ocean water surface and the air temperature in the control simulation, and the increased likelihood of ice cover being retained under warmer conditions, although with reduced concentration (Walsh 1991).

The inclusion of ice dynamics in an ice model allows the ice concentration to be determined by the advection of the ice where the ice velocity is derived from the momentum balance which includes the stresses on the ice from the prevailing winds and ocean currents. The lateral movement of ice also represents a transport of heat and salt, which impacts on the ocean in a coupled model. Ice formed in one area with a given internal thermodynamic structure and carrying a source of salt deficit (despite the internal brine pockets) is then transported and melts in another region. The inclusion of ice transport allows for a better representation of areas where there is a large change in seasonal ice coverage such as the Southern Ocean and the marginal ice zones of the shelf seas of the NH.

Internal ice resistance that prevents ice from continually building up has been parameterized in a number of ways in various ice models. These range from a simple ice viscosity term (Semtner 1987) to a viscous-plastic term, (Hibler 1979), cavitating fluid rheology, (Flato and Hibler 1990, 1992), or an elastic viscous plastic rheology (Hunke and Dukovwicz 1997).

A comparison by Flato and Hibler (1992) of the cavitating fluid rheology with other rheologies (full viscous plastic, incompressible, Mohr-Coulomb) has shown that it gives a reasonable representation of the ice thickness distribution in the Arctic with the maximum near the Canadian Archipelago. The direction and magnitude of the ice velocities are also comparable with those from buoy observations, though not as close as seen with the viscous-plastic case. Studies by SIMIP (Sea-ice Model Inter-comparison Project) also showed that the more computationally expensive viscous-plastic model gave the most realistic representation of the ice motion in the Arctic using a number of criteria with cavitating fluid giving a better representation than the incompressible and free drift cases (Kreyscher et al. 2000). The CSIRO model employs the cavitating fluid rheology as described by O'Farrell (1998).

The ice model described below has been used extensively in coupled model control and transient CO_2 increase simulations (e.g. Gordon and O'Farrell 1997) of the Mk 2 coupled model at R21 resolution. The ice model results have been stable and well behaved through multi-century and multi-millennial simulations.

19.1 Inclusion of leads in the atmospheric model

Within ice-covered areas the surface characteristics of each grid square are partitioned between a homogeneous ice surface (no account of variable ice roughness) and an open water section. The atmospheric model physics (clouds, radiation, moisture budget, heating of the air column, etc.) are then calculated separately over ice and open water and then combined with a weighted average at the end of each time step before dynamical calculations (such as horizontal advection

and mixing) occur. The advantage of this approach is that it more correctly represents the mixture of ice/water surface albedos and the differential heat fluxes.

Other modelling groups have instead used the simplification of area-weighted surface temperatures and albedos for their atmospheric models (Simmonds and Budd 1990). They justify such simplifications by the assuming that open water fraction is small compared to the overall horizontal mixing length scale. Details of the way in which the ice is distributed within the grid cell do not appear to have a major impact on how the profile in the atmosphere evolves according to results from limited area studies (H. Schlunzen, personal communication, 1994).

Compared to the "no-leads" results, the impact of the increased moisture transfer permitted through the open water allowed the development of more cloud over the Arctic and provided better agreement with observations in this region. This increased cloud cover decreased the shortwave radiation, but the outgoing longwave also decreased so that the overall effect on temperature is not clear-cut.

The most relevant input from the atmosphere to the ice model is the way the atmospheric model calculates surface stresses and heat fluxes. The variable surface drag and heat/moisture exchange coefficients are calculated by assuming a stability dependent boundary layer (Louis 1979).

19.2 Thermodynamic ice model

The thermodynamic component of the ice model is the three-layer model of Semtner (1976) which splits the ice mass into three layers, one for snow and two for ice. By calculating two internal ice temperatures, the model is able to better reflect the temperature profile that can exist within the ice, particularly in winter when a strong thermal gradient is imposed across the medium. The modeled ice retains an internal heat source that represents the heat trapped within the ice structure in brine pockets. This heat is replenished with 35% of the incoming solar radiation when the surface is snow free, and the heat stored is used up in the autumn, delaying slightly the cooling phase. If the snow cover becomes so great that it can depress the ice floe beneath the surface, then white ice is formed (Ledley 1985) by converting the volume of snow in excess of that which the ice floe can carry to ice as seawater rushes in to fill the voids. A maximum ice thickness has been set at $5\,m$, which is only invoked with ice that is trapped in embayments where grid resolution inhibits the calculation of ice velocities.

The energy budget equation of the ice, from which surface temperature is derived, is solved using an implicit technique similar to that used for the land and snow surfaces. Heat is assumed to penetrate over a few tens of mm depth, with heat capacity γ_i. The full equation is given by

$$\gamma_i \frac{dT_s}{dt} = (1-\alpha_s)S_s^{\downarrow} + R_s^{\downarrow} - \varepsilon_s \sigma T_s^4 - (H_s + E_s) \qquad 19.1$$

where $S_s^{\downarrow}$, $R_s^{\downarrow}$, E_s, and H_s represent the net downward solar radiation, net downward longwave radiation, and the (upward) latent and sensible heat terms, respectively. Internal temperatures are solved for in a similar manner to Semtner (1976) with the assumption that the equations are solved in $°C$ so that they can be linearized about $0°C$.

The albedos of snow and ice (α_s) are reduced from 0.8 to 0.7 and from 0.65 to 0.55 when the snow/ice surface temperature is at the melting point. The values have been chosen to represent area averaged values of melting snow and ice for a grid box of 200 *km* x 200 *km* from satellite measurements, rather than the minimum values that are measured in situ which would over represent the effect of melt ponds.

19.3 Ice Dynamics

The major dynamical balance on the ice is between the forcing of the ice from the atmospheric surface stresses and the ocean stresses represented in (19.2) by $\underline{\tau}_a$ and $\underline{\tau}_w$, respectively,

$$\frac{D\underline{V}_i}{Dt} = \Omega\, \underline{k}x\underline{V}_i + \underline{\tau}_a + \underline{\tau}_w - mg\underline{\nabla}H + \underline{F} \qquad 19.2$$

where $\underline{V}_i$ is the ice velocity, *m* is the total mass and Ω is the angular velocity of the Earth. The ocean stress is a linear function of the relative velocity of the ice and upper ocean currents, which are obtained from the ocean model in coupled simulation, and a climatology of an ocean-only simulation for the ice-atmosphere model. The geostrophic ocean flow is represented by the sea surface slope term $\underline{\nabla}H$ calculated from the same ocean simulation. The internal ice stress term is represented by the term $\underline{F}$. When neglecting nonlinear and acceleration terms, the equations can be rewritten in the form

$$-A\,u + B\,v + X = \frac{\partial p}{\partial x} \qquad 19.3$$

$$-A\,v - B\,u + Y = \frac{\partial p}{\partial y} \qquad 19.4$$

where u and v are the ice velocity components, and $A = C_w \cos(\theta)$, $B = mf + C_w \sin(\theta)$, C_w is the drag coefficient, θ the turning angle between the ice and ocean, and f is the Coriolis parameter. X and Y are all the terms in the equation independent of u and v, and p is the internal ice pressure. The gradients of p represent the internal stress in the cavitating fluid model (see Rothrock 1975, and Flato and Hibler 1990).

In the first instance, Equ. (19.3) and (19.4) are solved with the pressure term set to zero to give a free drift solution under the imposed external forcing. The cavitating fluid approximation then adjusts this solution at the grid points where ice is converging but introduces no change in divergent grid points. As the iteration evolves some of the points where ice was divergent will become convergent. The solution is iterated until it converges with a root mean square velocity difference between iterations less than a set criterion, which occurs satisfactorily at most time steps. A maximum number of iterations is imposed to cover the occurrences when convergence to the set velocity criterion is not reached.

During the iterations, the pressure term is incremented at each grid box in proportion to the velocity adjustment. This velocity adjustment is calculated by reducing the inward velocities to the cell and increasing the outward velocities to reduce convergence but conserve momentum

hence the velocity correction is proportional to the convergence rate. The pressure required to remove the remaining convergence is compared to the maximum allowed pressure. If the new increment in pressure required leaves the total sum larger than $P_{\max}$ then the velocity correction is reduced proportional to ($P_{\max} - P_{current}$). $P_{\max}$ is the ice strength, which is a function of both ice thickness and exponential function of ice concentration of the form

$$P_{\max} = 2.5x10^4 \; h^2 \; e^{-20(1-C)} \qquad 19.5$$

where h is the ice thickness and C is the ice concentration.

In order to help convergence of the iterative scheme some additional techniques have been tested to accelerate convergence of the scheme over the larger T63 grid point array. In the operational code the only one in use is to weight the velocity solution with 70% current solution and 30% previous solution to prevent time splitting to two solutions.

The approach to advection is to use an upstream scheme formulated in terms of the divergence field using the velocity field which is the solution to Equ. (19.3) and (19.4). The ice concentration is advected first, and then the ice volume from which the ice thickness is recovered after advection. The ice mass is conserved if the advection process allows the concentration to reach 100% and new leads are opened in the next thermodynamic step. The heat content, and brine content and snow layer volume are also all advected in this manner with temperatures, and thickness recovered after the advection step.

19.4 Lateral ice growth and ocean mixed layer parameterization

Ice-edge advance is controlled by the energy budget in the grid square adjacent to the ice edge, assuming a mixed layer depth of $100\ m$. The temperature for this ocean water mass (T_s) is calculated using the heat flux terms and a weak relaxation to the prescribed sea surface temperature (SST, T_{SST}) as follows:

$$\gamma_0 \frac{dT_s}{dt} = (1-\alpha_s)S_s^{\downarrow} + R_s^{\downarrow} - \varepsilon_s \sigma T_s^4 - (H_s + E_s) + \lambda_C (T_{SST} - T_s)\,. \qquad 19.6$$

Here γ_0 represents the heat capacity of a $100\ m$ deep water column and λ_C is the time constant for the relaxation set at $(23\ days)^{-1}$. Once this water column reaches the freezing point, new ice can form over a small percentage (4%) of the grid. If ice advects outside the existing ice area and the adjacent mixed layer is close to the freezing point, then the ice is allowed to remain and the grid point starts operating as an ice point with the parameterization of the heat reservoir in the mixed layer that is described below.

Ice compactness/concentration is calculated using a scheme based on the effect of the heat budget on an area covered with a mixture of open water and ice. This approach to the thermodynamics differs from the widely followed approach suggested by Semtner (1976) where the water column remains at the freezing point until all the ice has melted away. At the ice margin, ice is found to occur at least $2°C$ above the freezing point while gradually melting.

The equation used to calculate the temperature of water within a grid square with fractional ice cover is

$$\gamma_0 \frac{dT_s}{dt} = (1-\alpha_s)S_s^{\downarrow} + R_s^{\downarrow} - \varepsilon_s \sigma T_s^4 - (H_s + E_s) + F_i \qquad 19.7$$

where the oceanic heat flux term F_i is given by a fixed geographic fraction and a variable component dependent on the difference between the SST climatology and the freezing point T_f. The flux F_i represents the heat entrained across the ocean thermocline and applies equally to the mixed layer and to the ice:

$$F_i = k_{frz}\ \rho_w c_w dz(T_{SST} - T_f)/(dz/2)^2 + F_{geog} \qquad 19.8$$

where $k_{frz} = 0.15x10^{-4}\ s^{-1}$ is the heat transfer coefficient, dz is the thickness of upper ocean layer, ρ_w and c_w are the density and heat capacities of the ocean. F_{geog} is set to $15\,W\ m^{-2}$ in the Antarctic and $4\,W\ m^{-2}$ in the Arctic. In the coupled model, the SST climatology T_{SST} is replaced by the ocean temperature T_{OC}.

If the upper ocean temperature in the coupled model (T_{OC}) falls below freezing point, an additional term is added to the oceanic heat flux to enhance ice growth, and the model itself adjusts so that the mixed layer temperature in the leads rarely falls below $-2.0°C$. The additional ice-ocean heat flux in this situation has the form

$$F_{frz} = k_{frz}\ \rho_w c_w dz(T_{OC} - T_f)/(dz/2)^2 \qquad 19.9$$

where k_{frz} is increased to $6.0x10^{-4}\ s^{-1}$ to stimulate the formation of ice in sub-freezing waters. The temperature may occasionally drop to below freezing at some individual interior ocean grid points as a result of numerical noise. In such cases, the surface ocean temperature (in the ocean model) is set back to $-1.85°C$ and a temperature adjustment is made at neighbouring points to conserve heat.

19.5 Lateral ice growth scheme

There are two branches to this scheme: one for cooling of the ocean mixed layer and one for warming. If the system is cooling, the mixed layer is allowed to cool down until it reaches the freezing point. When the mixed layer is at the freezing point, a thin layer of new ice is allowed to grow over the open water area. If the ice is less than 0.25 *m* thick (a typical thickness for pancake ice), the volume of new ice is added to the base of the ice. (This addition of new ice growth to the base is realistic as ice in calm conditions can grow in columnar crystals to this depth, but also has been employed for numerical purposes to prevent a 200 *km* x 200 *km* grid square being covered by, say, 0.01 *m* thick ice). If the ice is thicker than 0.25 *m* then the new ice volume is added to the side of the floes. This represents a lateral growth in ice that occurs when small floes coalesce and when pancake ice is crushed against floe sides as ice interacts and as new leads open up for new ice production. A minimum direct interaction between the atmosphere and ocean always occurs. If the ice concentration is calculated to be greater than 98% in the

Antarctic, or 99.5% in the Arctic, any additional ice growth is added to the base of the existing ice.

If the mixed layer warms, its temperature is allowed to be greater than the freezing point (set at $271.3\,K, -1.85°C$), reflecting the fact that when ice freezes, the salinity lies between 30 ppt (parts per thousand) and 35 ppt. Brine is then rejected from the ice and the salinity decreases in first-year ice to about 10 ppt which allows the ice to have a higher melting point. Hence the mixed layer acts as a heat buffer. When the calculated temperature lies between $-1.85°C$ and $-1.5°C$, no lateral melting occurs. Surface melting can occur depending on the one-dimensional thermodynamic calculation (Semtner 1976) and from basal melt with the warmer ocean water.

Once the mixed layer temperature is above $-1.5°C$ any additional heating is partitioned equally between further warming of the mixed layer and lateral ice melt. Lateral ice melt plays a major role in the decay of an ice cover, particularly from the undercutting of an ice floe from below the water line. As the concentration drops, the wave field becomes more active (Wadhams 1991) and floes get washed over by warm water, another form of lateral melt. If the temperature is greater than $-1.0°C$, then all additional heat goes into lateral melting.

The mixed layer depth has been set at $100\,m$ depth which is sufficient to prevent a too early seasonal retreat of the ice in both hemispheres, particularly in the Arctic. Observations suggest that $100\,m$ is a reasonable value for the depth of stratification for most of the Southern Ocean. For the shelf seas, where the water column is also mixed tidally from below, the upper isothermal layer is about $50\,m$ in depth. In the Arctic, there is strong salinity stratification, and so the actual mixed layer is quite shallow. However, the water column is isothermal well below this depth at least to $100\,m$ throughout most of the year, and it is the heat capacity of the upper ocean that is employed in the lateral melt parameterization outlined above.

20 Oceanic component model

The oceanic component of the CSIRO Mk 3 model is based on the code of the GFDL Modular Ocean Model (MOM), Version 2.2 (Pacanowski 1996). It supersedes the oceanic code in the CSIRO Mk 2 model, which was based on the earlier GFDL Bryan-Cox code (Cox 1984). The decision to upgrade to MOM 2.2 was made because the structure of the earlier code was becoming increasingly out of date, and because there were several major improvements in the model physics and numerics which were available in the newer code. At the time of inception of the work towards Mk 3, MOM 2.2 was chosen as the most recent of the GFDL codes available. Since then, GFDL has released MOM 3, which includes additional features and code refinements, and is currently being examined for suitability as the oceanic component of future versions of the Mk 3 model. The work on MOM 3 will be reported elsewhere.

20.1 Resolution

The oceanic component has horizontal resolution matching that of the atmospheric model's (T63) physics grid in the east-west direction, and twice that in the north-south direction. Thus the grid spacing is 1.875° longitude by 0.93° latitude (approximately; latitude is on a Gaussian grid). The horizontal grid boxes (for the AGCM) are shown in Fig.2, in Section 7. The ocean grid boxes have the same horizontal layout, but with two ocean model grid boxes per AGCM grid

box meridionally. There are 31 levels in the vertical, with the spacing of the levels gradually increasing with depth, from 10 *m* at the surface to 400 *m* in the deep ocean. These are given in Table. 7.

Model level k	Depth of layer (*m*)	Layer thickness (*m*)
1	5.00	10.00
2	15.00	11.62
3	28.25	13.51
4	42.02	15.71
5	59.66	18.26
6	78.54	21.22
7	102.11	24.67
8	127.88	28.68
9	159.47	33.34
10	194.56	38.75
11	236.97	45.04
12	284.65	52.36
13	341.69	60.87
14	406.38	70.75
15	483.19	82.24
16	570.87	95.83
17	674.86	111.45
18	793.76	129.61
19	934.08	150.73
20	1095.21	175.29
21	1284.65	203.85
22	1502.91	237.06
23	1758.77	275.69
24	2054.29	320.61
25	2400.00	372.85
26	2800.00	400.00
27	3200.00	400.00
28	3600.00	400.00
29	4000.00	400.00
30	4400.00	400.00
31	4800.00	400.00

Table 7. Level structure of the Mk3 OGCM and level depths.

20.2 Domain and bathymetry

The domain is global, as per the atmospheric model. The bathymetry is set firstly by an averaging of the ETOPO5 5’ by 5’ data (NOAA 1988) onto the model grid, secondly by modifications of the coastline to ensure consistency between oceanic and atmospheric land-sea grids, thirdly by light smoothing in places of highly complex topography to reduce the risk of numerical noise, and finally by modification where necessary to ensure that important sill depths are correctly represented. Water exchange between inland seas (Baltic, Hudson Bay, Persian

Gulf, Red Sea, together with coastal indentations that are only one grid point wide) and the nearby open ocean is set to occur at fixed rates to parameterize the actual exchanges through unresolved straits. The Strait of Gibraltar is marginally resolved in the model.

20.3 Numerical choices

The grid of MOM 2.2 is that of the "Arakawa B grid", whereby the velocity points are located at the corners of grid boxes centered on the temperature/salinity (T/S) points, or vice versa. If the grid is non-uniform (e.g., a latitude/longitude grid on the globe), then a choice must be made between having the T/S or the velocity points located at the centers of grid boxes. In the present model, T/S points are located at the centers of grid boxes in the horizontal, because this conforms with the physics grid structure of the atmospheric model and ensures flux conservation in the coupled model. A similar choice of grid box centering needs to be made independently in the vertical, where vertical velocity points are offset in the vertical relative to T/S points. Here, vertical velocity points are located at the centers of grid boxes, as this has been shown to yield slightly more accurate numerics (Pacanowski 1996).

The present model uses the "quicker" scheme for tracer (T/S) advection, which is a modification of the Leonard (1979) "quick" scheme as described in Pacanowski (1996). The scheme is of third-order accuracy and weakly diffusive. This scheme is being used in an increasing number of numerical ocean models, in preference to the older second-order centered-difference scheme, because of the much reduced levels of numerical dispersion generated in the tracer fields. In some earlier versions of the model, which used centered-differencing, this dispersion was found to be sufficiently severe to cause spurious dense bottom water formation at the southern boundary of Drake Passage. In the present model, use of the "quicker" scheme largely mitigates this problem. There is no evidence of serious deleterious effects on the oceanic solution resulting from the residual numerical diffusion associated with this scheme, though further diagnosis (e.g., of the large-scale dianeutral motion field) is desirable to better quantify any impact of this scheme's diffusive aspects.

Standard choices are made for the numerical representation of the momentum equations. Momentum advection is represented by centered finite differences and a uniform horizontal viscosity, of $A_m = 3\times10^4\ m^2\ s^{-1}$, is applied. A background minimum default vertical viscosity of $\mu = 2\times10^{-3}\ m^2\ s^{-1}$ is also applied. The standard choices made for the momentum equations contrast with the careful treatment of the tracer (T/S) advection equations ("quicker" higher order scheme and zero horizontal diffusion). This is because of the differences in the balance of terms in the prognostic equations for momentum and tracers in the ocean. Tracer advection is a dominant term so needs to be represented accurately while momentum advection in a model of the present resolution is almost everywhere negligible. Further, preservation of advected water properties is crucial in an ocean simulation, as dianeutral mixing of tracers in the interior ocean is observed to be mostly extremely weak (e.g., Ledwell et al. 1999), a situation which is violated by the specification of a horizontal diffusivity (e.g, Hirst and McDougall 1998). In contrast, the dominant momentum balance over most of the ocean away from the coast (and the equatorial undercurrent) is one of geostrophy, and this is maintained regardless of the presence or absence of a viscosity of similar order to that here. Near the coast, the specified viscosity must be large enough to spread the boundary currents over the width of at least one grid box, and the value of A_m chosen here is close to the minimum required to satisfy this criterion.

20.4 Choice for representing the external barotropic mode

The present model uses the traditional rigid-lid assumption (i.e., that the surface vertical velocity is zero) to allow the oceanic barotropic motion to be represented by a streamfunction. This has the advantage of allowing relatively large model time steps, but the disadvantage that the freshwater flux from the atmospheric model needs to be converted into an equivalent salt flux, which is inherently less accurate than would be forcing by the direct freshwater flux. Very recently, efficient codes have been developed (for MOM 3) which overcome the problems associated with the free surface representation, but these codes were not available for MOM 2.2. Therefore, we retain the traditional rigid-lid method for the interim.

20.5 Sub-grid-scale mixing and stirring of tracers in the ocean interior

Isoneutral mixing of tracers is performed by the code of Griffies et al. (1998). The small angle assumption is adopted to simplify the diffusion rotation tensor, as recommended for general oceanic applications by Gent and McWilliams (1990) and Griffies et al. (1998). The isoneutral tracer diffusivity A_I is set to 1000 $m^2\ s^{-1}$, except in regions of steeply sloping neutral surfaces, where the diffusivity is reduced via the Gerdes et al. (1991) taper to avoid numerical instability.

Adiabatic eddy-induced transport is included via the Griffies (1998) implementation of the Gent and McWilliams (1990) scheme. The value of the isopycnal thickness diffusivity κ is 100 $m^2\ s^{-1}$. Here also κ is reduced according to the Gerdes et al. (1991) taper in regions of steeply sloping neutral surfaces. This value of κ is near the smaller end of the range used in large scale ocean models. North Atlantic overturning is found to be better simulated in the present model when such a relatively small value of κ is adopted. Past experience has shown that numerical dispersion problems tend to increase as κ is decreased (e.g., Hirst and McDougall 1996). So far, no serious numerical dispersion problems have been found in the solutions of the present stand-alone oceanic and coupled models for integrations of order a century in length, but further examination of this issue involving longer integrations is desirable.

Vertical mixing of tracers in the ocean interior is performed via a vertical diffusivity, A_V, whose value is a function of depth, following a modified form of the widely-used Bryan and Lewis (1979) profile at depths below 350 *m*. This profile prescribes a value of approximately 1.3×10^{-4} $m^2\ s^{-1}$ in the deepest ocean, grading to about 0.3×10^{-4} $m^2\ s^{-1}$ above 1000 *m* depth. This is shown in Fig. 6. In the present model, A_V is used in regions poleward of 30°S and 30°N. For tropical regions (15°S to 15°N), this profile is modified by use of the profile A_{VT} (see Fig. 6). This lower value is helpful in achieving a realistically sharp thermocline in the tropics, which is in turn important in the simulation of ENSO in the coupled model. The two profiles are blended smoothly in the latitudinal regions 15° to 30° in both hemispheres.

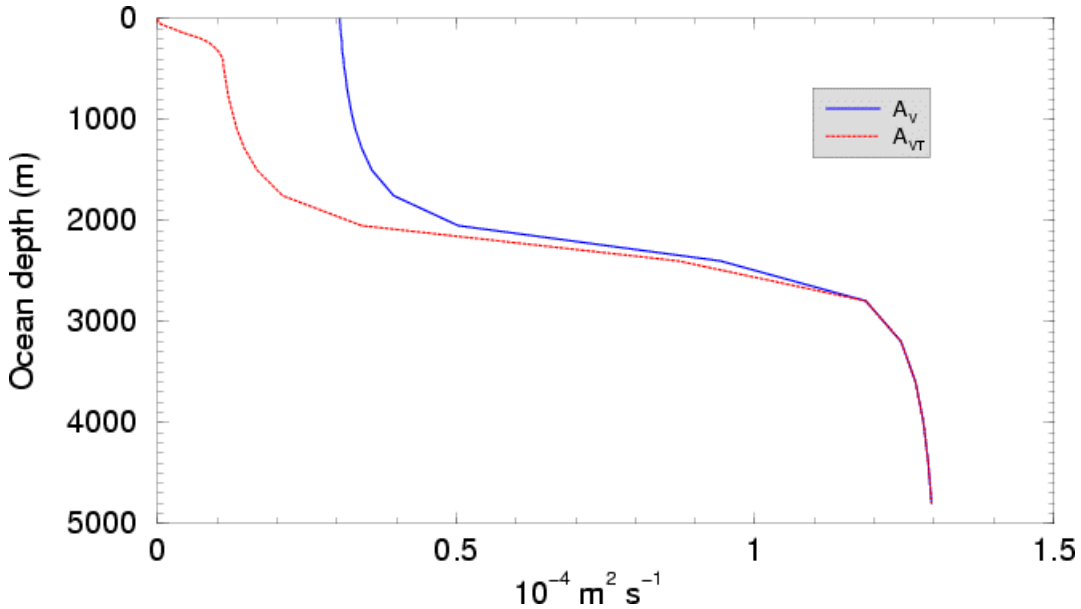

Figure 6: Vertical diffusivity as a function of ocean depth.

20.6 Near surface and shear mixing

Near surface mixing is achieved by a hybrid mixing scheme involving (1) a component for the effect penetrating solar radiation, (2) a bulk Richardson number component, and (3) a gradient Richardson number component. The penetrating solar radiation and the bulk Richardson number components are described below, while the gradient Richardson number component is described in the following section.

It is well established that penetration of solar radiation destabilizes the water column and enhances vertical mixing (Chen et al. 1994; Schneider et al. 1996). To include this effect, we use the dual exponential formulation of Paulson and Simpson (1977), where a portion of the net solar radiation is set to be absorbed with a very small *e*-folding depth (typically less than a metre) and the remainder is set to be absorbed with a much larger *e*-folding depth (tens of metres for clear water). The coefficients of the Paulson and Simpson (1977) scheme depend on the turbidity of the water, and are specified in terms of Jerlov (1977) water types. Global fields of Jerlov water types are constructed by using the water transparency data of Simonot and Le Treut (1986), together with their formulae for converting their Secchi-depth data to Jerlov water types. Our use of spatially varying Jerlov water types contrasts with many other coupled models, where the clearest of the Jerlov types is assumed to apply over the entire globe.

The Richardson number schemes simulate the effect of mixing resulting from vertical shear in the water column. The bulk Richardson number component is specifically designed for near-surface mixing. It is based on the formulation of Price et al. (1986), where a bulk Richardson number

$$Ri_b = gz\Delta\sigma_\theta / \rho_0 /(\Delta U^2 + \Delta V^2) \qquad 20.1$$

is calculated progressively down from the surface until stability is reached. Here $\Delta\sigma_\theta$, ΔU and ΔV indicate the difference between the potential density, and zonal and meridional velocities at the surface and at depth z, respectively, and ρ_0 is a reference density. The stability criterion is

set at Ri_b value of 0.65. The water column is then mixed down to the depth where Ri_b first exceeds the critical value.

Model experiments have demonstrated that the above hybrid scheme (solar penetration plus bulk Richardson number plus gradient Richardson number) does not adequately simulate the effect of mixing associated with wind-generated turbulence at the ocean surface. The effect of this omission is strongest at mid-to-high latitudes, where summer mixed layer depths are typically too shallow, which resulted in excessive summer warmth of the ocean surface in a preliminary version of the coupled model. An interim ad-hoc mixing scheme was implemented to allow for more realistic levels of near-surface mixing. In the subsequent version of the Mk3 model (Mk3.1), which is currently under testing, the Kraus-Turner scheme is implemented in place of the bulk Richardson number scheme to allow for a more complete treatment of wind forced mixing effects.

20.7 Integer Power Vertical Mixing Scheme

Coupled general circulation models have tended to have weak ENSO variability that arises, at least in part, from the diffuse equatorial thermocline that has been common in ocean GCMs (Cane 1992; Meehl et al. 2001). In the present coupled model the Integer Power vertical mixing scheme (Wilson 2000, 2002) is used to achieve a "sharp" thermocline in the equatorial Pacific Ocean and so promote strong ENSO variability.

The Integer Power scheme is based on the widely used Pacanowski and Philander (1981) scheme but with mixing profiles based on an integer power approximation to the Peters et al. (1988) (hereafter PGT) observational data. PGT provide fractional exponent relationships, based on their observations, for calculating vertical eddy coefficients for momentum, K_m, and heat and salinity, K_h, as a function of the gradient Richardson number,

$$Ri_g = \alpha g T_z / (U_z^2 + V_z^2) \qquad 20.2$$

where α is the coefficient of thermal expansion of water, g is the acceleration due to gravity, T is the ocean temperature, T_z is the first derivative of temperature with respect to depth, z, U and V are the horizontal velocity components in the zonal and meridional directions respectively, and U_z and V_z are the first derivatives of U and V with respect to depth, z.

However, the PGT fractional exponents unnecessarily add to the complexity of the vertical mixing formulation and slow the computation. Therefore, instead of the PGT *fractional* exponent relationships, the Integer Power vertical mixing profiles use an *integer* power fit to the PGT hourly data:

$$K_m = \min(K_{m,\max}, aRi_g^{-8} + \frac{b}{(1+5Ri_g)^2}) + K_{m,b} \qquad 20.3$$

where $a = 6.7490 \times 10^{-8}\ m^2\ s^{-1}$, $b = 8.612 \times 10^{-4}\ m^2\ s^{-1}$, and

$$K_h = \min(K_{h,\max}, cRi_g^{-10} + \frac{d}{(1+5Ri_g)^3}) + K_{h,b} \qquad 20.4$$

where $c = 2.027\times10^{-9}\ m^2\ s^{-1}$, $d = 8.480\times10^{-4}\ m^2\ s^{-1}$, and where $K_{m,b} = 2\times10^{-5}\ m^2\ s^{-1}$ and $K_{h,b} = 1\times10^{-6}\ m^2\ s^{-1}$ are background mixing coefficients that are independent of Ri_g.

The maximum vertical mixing eddy coefficients calculated with these equations are limited by the min function to $K_{m,\max} = 265\times10^{-4}\ m^2\ s^{-1}$, and $K_{h,\max} = 199\times10^{-4}\ m^2\ s^{-1}$. Because these limits are based on the PGT hourly data, rather than their 4.5 day mean data, the Integer Power scheme's mixing coefficients at low Richardson number are an order of magnitude higher than those for conventional PGT formulations (see, for example Schneider and Müller 1994; Yu and Schopf 1997) that are based on PGT's 4.5 day mean data. Wilson (2002) has shown that, for the Pacific Ocean, these high mixing coefficients at *low* Ri_g give an equatorial upwelling pattern that differs from conventional patterns by having its maximum at a more easterly location, having a lower and longitudinally-broader maximum of value order $1.5\times10^{-5}\ m\ s^{-1}$, and having decreasing values west of 150°W. Each of these differences improve agreement with the limited upwelling observations, and help to reduce, but by no means eliminate, the common coupled model problem of the equatorial SST "cold tongue" extending too far into the west Pacific Ocean.

The Integer Power scheme employs very low background mixing coefficients at *high* Ri_g. These low background mixing coefficients are also based on the PGT data and similar low values had previously been tried in various PGT-based vertical mixing schemes without achieving a sharp thermocline (Kattenburg and Allart, in Stockdale et al. 1993; Schneider and Müller 1994; Syu et al. 1995; and Yu and Schopf 1997), possibly because of warm surface water accumulation problems. Wilson (2002) has demonstrated that these low background-mixing coefficients are in fact required to achieve a sharp equatorial thermocline. In the present model they also strengthen the equatorial under-current in the east Pacific.

20.8 Oceanic Convection

Subsequent to the above mixing and advection processes, the oceanic solution is scanned for static instability. Any statically unstable water columns are subject to convective mixing according to the algorithm of Rahmstorf (1993), that mixes a statically unstable water column to produce a neutral profile in a single pass.

20.9 Filtering

Model fields are subject to Fourier filtering at latitudes north from latitude 80°N, to prevent CFL numerical instability which would otherwise result from the narrow zonal grid spacing at extreme high latitudes. No Fourier filtering is applied in the southern hemisphere.

20.10 Parallelisation on NEC and Cray computers

The oceanic component runs efficiently on up to four processors on NEC (SX4 or 5) machines. In coupled mode, it is always set to run over four processors. Considerable effort was required to parallelise the code for efficient running over four processors, since MOM 2.2 did not come with

a working parallelisation option. The details of this work are available from one of the authors (L. J. Waterman, *unpublished manuscript*, ljw@uvic.ca). The code has also been enabled to run in parallel on Cray computers.

20.11 Oceanic component spin-up

Prior to initiation of coupled model integrations, the oceanic component is spun up for the order of 500-1000 years in a configuration identical to that to be employed in the coupled model integration. This spin-up is initiated from one of a selection of restart files from previous long oceanic component integrations, the case selected being the one which is likely to yield the smallest drifts in the deep ocean fields during the spin-up. This is done in order to obtain an oceanic solution as close as possible to thermohaline equilibrium prior to coupling, given bounds on computational time available for the spin-up. The spin-up uses the technique of asynchronous time stepping (Bryan 1984), where tracer time steps are much larger (0.5 day) than momentum time steps (15 minutes). Modest discrepancies may occur in the seasonal cycling of the ocean under this time-step regime (Bryan 1984). Hence an additional several years of integration are conducted as a final stage of the oceanic spin-up, where the time steps are set to be 15 minutes for all prognostic model variables, which is the same as that used in the coupled model integration.

In spin-up, the oceanic component is forced by wind stress from the stand-alone atmospheric model, and by restoration of surface temperature and salinity to observed climatology. Future spin-up integrations may use a combined forcing by surface tracer restoration to observed climatology plus heat and freshwater fluxes taken from either the stand alone atmospheric integration or from a suitable previous coupled model integration. Such an approach is expected to result in reduced oceanic adjustment upon coupling, by forcing the ocean in a manner more consistent with that likely to be experienced after the initiation of coupling.

21 The coupled model

There are many ways of preparing (i.e. spinning up) the AGCM and OGCM components of a coupled model prior to coupling, and also different ways of implementing the coupling process. For example, some models use a combination of AGCM and observed surface forcing to spin up the OGCM prior to full coupling. There are many variants, and some information about different strategies are given on the PCMDI web site for models taking part in the CMIP1 coupled model intercomparison http://www-pcmdi.llnl.gov/modeldoc/cmip1/table2.html . There is also a review of various coupling strategies by Stouffer and Dixon (1997) which is available from http://www.gfdl.gov/~rjs/cpld_init/coupled.initialization.html . The method used for the Mk3 coupled model essentially follows that for the Mk2 model (Gordon and O'Farrell 1997), except that flux adjustments are not included.

The AGCM, which consists of atmospheric, land-surface, and sea-ice components, is spun up during the development phases, and there is a 10-year run prior to coupling. The AGCM is forced by the annual cycle of observed SSTs, and the ice model is dynamically driven from below by an annual cycle of ocean currents taken from the ocean model spin up. The AGCM timestep during spin up is 15 minutes. The OGCM (see previous section) is spun up from previous developmental phases, as described in Section 20.

The coupled model is generated by combining both models, and by using the master routine (*main*) to control the sequence of events. Both AGCM and OGCM are first initialized (*atstart* and *mom2start*). The coupled model timestep then has the following sequence (see Appendix C):

a) Prepare the OGCM fields (SST, surface U,V) for the AGCM (*mom2_to_agcm*)
b) Do the AGCM timestep (*atstep*)
c) Prepare the AGCM fields (stresses, heat fluxes, water flux) for the OGCM (*atmos*)
d) Do the OGCM timestep (*mom2step*).

Because of the above sequencing, and in order to start up (or restart) the coupled model, there must be an additional coupled "restart file" containing the SST and surface U, V (for the ice model) from the last timestep of the coupled OGCM. Thus the AGCM relies on the OGCM to provide SSTs and surface ocean currents. In turn, the OGCM requires the AGCM to deliver surface stresses, surface heat fluxes, and a surface fresh water flux. The latter are generated through the AGCM routines *ocntau* (stresses) and *ocforce* (heat and water flux) by using data gathered during the execution of the physical parameterizations.

The surface stresses for the ocean are taken directly from the ocean-atmosphere surface stress over the open ocean, but in the case of grid points that have ice present, then the fractional ice cover has to be accounted for. The total stress on the ocean is then made up of part stress between ice and the underlying ocean, and part stress between the leads-atmosphere.

The heat flux *into* the ocean (with surface temperature T_{OC}) is obtained from the surface energy balance G where

$$G = (1-\alpha_s)S_s^{\downarrow} + R_s^{\downarrow} - \varepsilon_s \sigma T_{OC}^4 - (H_s + E_s)\,. \qquad 21.1$$

(See start of Section 8 for a definition of terms). For parts of the ocean covered by ice, the heat flux is computed from the transfer of heat between the ocean and the ice (see Section 19). As for the stresses, the fractional cover of ice has to be accounted for. In the case of the solar input, this is allowed to penetrate into the ocean, depending upon the turbidity of the ocean water (see Section 20).

The freshwater flux into the oceans can be made up of several parts. For the open oceans, this is given by the precipitation less evaporation (P – E). At coastal points, there can be runoff from the land. In the current version of the Mk3 model, runoff at inland grid points is taken by downslope flow to the appropriate coastal ocean grid point, with runoff transported immediately to the ocean grid point. (There has been a subsequent enhancement to this scheme whereby the runoff is transported from grid point to adjacent grid points (i.e. river flow) with appropriate downslope flow rates. This allows for a considerable time delay in some cases, e.g. Amazon flow, between the time that the runoff occurs and the time that it arrives at the river mouth. This method will become operational in the next development phase of the Mk3 model.)

The formation and melting of sea-ice also implies changes to the freshwater flux into the ocean. When ice is formed, there is brine rejection. On the other hand, when ice melts (the sea-ice in the model has a fixed salinity of 10 ppt), there is an implied injection of fresh water into the oceans. The horizontal advection of the ice means that there may be more brine rejection is some areas, and more ice melting (freshwater input) in other areas. The melting of snow on ice is also

accounted for as a freshwater input. If there is sublimation from bare ice, then there is an implied brine rejection into the oceans. Again, as for the stresses, the partial cover of ice at a grid point is accounted for in the computation of these components of the freshwater flux.

The above components of the salinity forcing may be written as follows. Let the freshwater flux into the oceans (excluding sea-ice melting/freezing) be denoted by δ_{FW}. Denoting land runoff by R_{off}, this is given by

$$\delta_{FW} = (P - E) + R_{off} + (\textit{snow melt on sea ice}) \qquad 21.2$$

where all units are in metres of water per model timestep (Δt). We denote the ocean salinity by S_{OC}, and sea-ice is taken to have a fixed salinity $S_{ICE} = 0.01$. Let the change of depth of sea-ice (taking into account the fractional cover of sea-ice per grid point) be given by δ_{IS}, and any sublimation from bare ice given by δ_{SB}. The rate of change of salinity (sec^{-1}) generated by the above components may then be written as

$$\frac{\delta S}{\delta t} = \{\delta_{IS}(S_{ICE} - S_{OC}) + \delta_{SB} S_{ICE} - \delta_{FW} S_{OC}\}/(\Delta t\ dz_1) \qquad 21.3$$

where Δt is the timestep (in seconds), and dz_1 is the depth of the first ocean level (in metres). The salinity of the ocean (S_{OC}) in this computation is not taken from the ocean model, but is given a constant (global mean) values of 35 ppt (i.e. $S_{OC} = 0.035$). This is done to ensure that there will be conservation of fresh water in the coupled model simulation. Equation (21.3) is then converted to an equivalent P - E flux (as required by the MOM2 ocean model) by

$$\frac{\delta S}{\delta t} = \{-\delta''_{FW} S_{OC}\}/(\Delta t\ dz_1) \qquad 21.4$$

where δ''_{FW} gives the "P - E" flux taking into account land runoff, snow melt on ice, and ice brine rejection components.

In order to initialize the Mk3 coupled model, the AGCM and OGCM components were simply combined, and the coupled model started from the final restart files of the spin-up AGCM and OGCM runs. Clearly, there was no feedback between ocean and atmosphere during these spin ups, and it is to be expected that the coupled model will experience some initial adjustment phase, and some climate drift, as the various feedbacks between ocean and atmosphere come into play.

22 Coupled model climatology

The two major components of the coupled model, the AGCM (= Atmosphere + Land + Ice) and the OGCM, were spun-up prior to coupling, and the climatologies of these stand-alone components will be reported elsewhere. In fact, there are so many parts to a coupled climate model that it in order to do justice to each of the four basic components (atmosphere, land, ice,

and oceans) would require a separate report detailing their behaviour in both non-coupled and coupled modes. The main aim of this report is to give technical details about the four sub-components of the coupled model, and including detailed climatologies about each is clearly beyond the scope of this report. However, in order to give an indication of the current status of the Mk3 coupled model, a brief outline of the climatology obtained during the first part of a long period integration of the coupled model will be presented. Here we will concentrate on the first 80 years of a longer period control integration (which is now being extended).

The Mk3 coupled model was initialized by simply combining previously spun up components of the AGCM and OGCM. There will clearly be some “shock” to the climate system following coupling as the various feedbacks between atmosphere and ocean that were missing before now come into play. After the Mk3 coupled model was started, the model components did exhibit some adjustment, and there was some climate drift (a cooling). This is illustrated by the change in the global mean SST (Fig. 7).

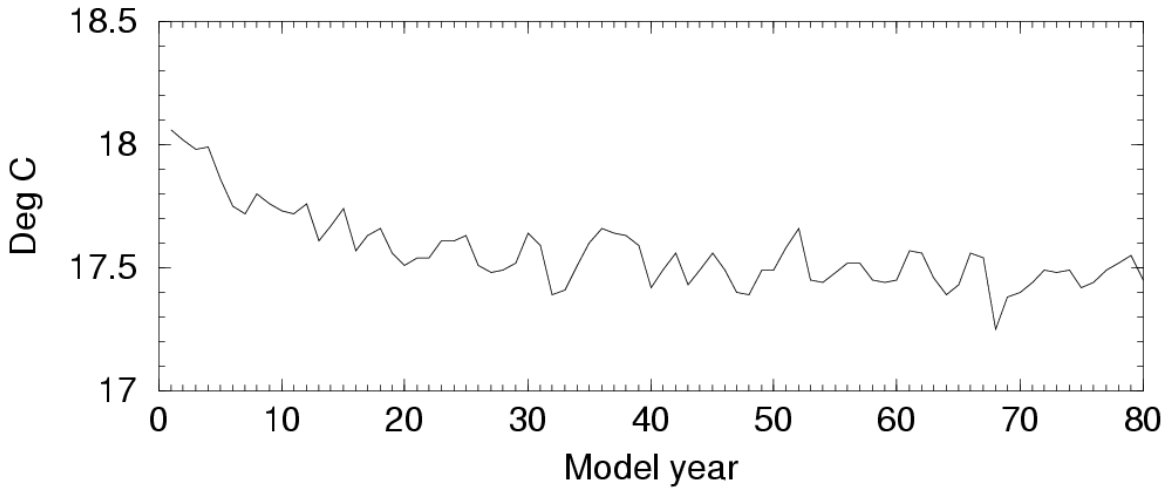

Figure 7. Global mean SST.

The change in global mean SST is about 0.5°*C* over the 80-year period. Reasons for this drift are currently under investigation. The global distribution of this change is shown in Fig. 8 in which is displayed the difference between the average of the coupled model SST (years 71 to 80) and the observed SST.

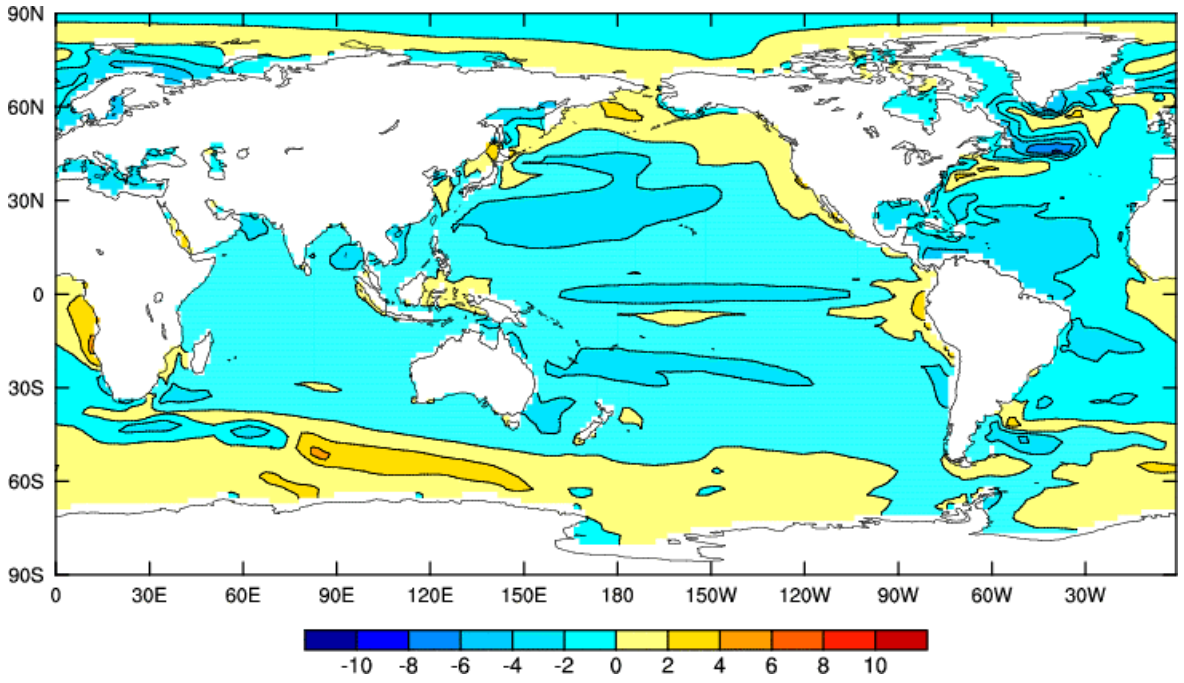

Figure 8. Annual mean SST difference (°*C*): Coupled minus observations.

During spin-up, the OGCM is constrained by the restoration condition at the surface (restoration to Levitus based observations). Upon coupling, the ocean surface responds to the heat flux supplied by the AGCM, and some noticeable differences between the modelled SST and the observed climatology become apparent. In the tropical Pacific, there is an over representation of the “cold-tongue”. This cold-tongue is too prominent in the OGCM spin-up (not shown), and is made a little worse following coupling. This cold-tongue problem is common to many coupled models (Mechoso et al. 1995; Meehl et al. 2001), and even in some quite high resolution (equatorial) coupled models (Pontaud et al. 2000). Another problem area for moderate resolution global coupled models is the positioning of the Gulf Stream and the Kuroshio Current. In the Mk3 coupled model, the Gulf Stream does not extend far enough northward near Newfoundland, as illustrated by a strong cold patch in that region in Fig. 8. There are several regions (North Pacific, the western tropical Atlantic, around the STCZ, and off Argentina) that have cold anomalies in excess of 2°*C*.

On the other hand there are some areas of warming. A large part of the Southern Ocean shows some warming, and there are also areas such as to the west of southern Africa (the Benguela Current) that show warming. Overall, there is rather more total area with cooling than warming, and hence the decrease in global mean SST over the 80-year period. It is worth noting that the SST difference shown in Fig.8 is between the coupled model SST and the observed SST, and if the difference had instead been taken between the coupled model SST and the OGCM spin-up SST then the apparent coupled model SST errors are somewhat reduced. This is because the SST climatology of the OGCM has some inherent deficiencies relative to the observed SST climatology, and these will not necessarily be improved by coupling. The same applies to sea surface salinity errors (Fig. 10).

In the Southern Ocean, the region around Kerguelen shows a cool area to the northwest and a warm area to the southeast, which extends into the Antarctic Circumpolar Current down towards Antarctica. An inspection of the coupled model SSTs in that region (Fig. 9) show that the

coupled model is unable to reproduce the observations (not shown) that reveal a much more zonally uniform structure in the vicinity of Kerguelen. Also shown in Fig. 9 is the model topography. This has been plotted by reference to the model levels. (There are 31 levels in the model, with 31 being at 4800 *m*. Some of the depths of other levels are level 6 = 78 *m*, level 12 = 285 *m*, level 18 = 794 *m*, and level 24 = 2054 *m*). The topography associated with Kerguelen plateau in the presence of the strong Antarctic Circumpolar Current leads to the development of a Rossby lee-wave. This feature has been discussed by Hughes and O'Farrell (1999) for the lower resolution Mk2 ocean where a theoretical model is also provided.

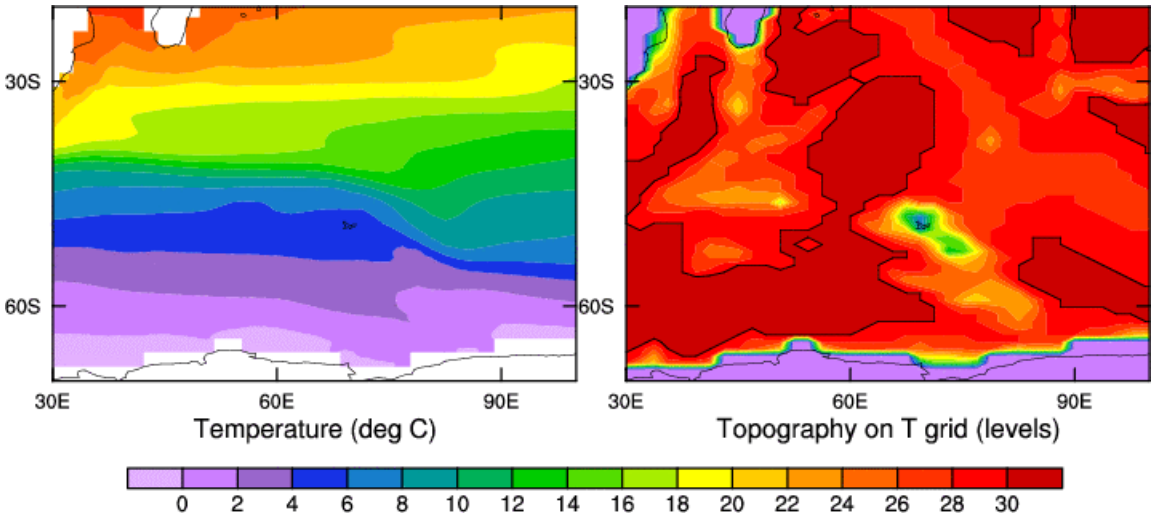

Figure 9. Coupled model annual mean SST (left) and ocean topography as indicated by T-grid levels (right) around Kerguelen in the Southern Ocean..

The change in the global distribution of sea surface salinity (SSS) is shown in Fig. 10. Here the units are ppt (parts per thousand). As for Fig. 8, this is the difference between the average of the coupled model SSS (years 71 to 80) and the observed SSS. The most prominent changes in the surface salinity are in the Arctic region. Here there has been a freshening in the Barents Sea and an increase in salinity in the East Siberian Sea which extends across to the Beaufort Sea. Some increase in salinity is present in the North Pacific. The Hudson Bay has also become fresher, due to the river inflow into this region, and possibly insufficient exchange of seawater between Hudson Bay and the North Atlantic. In the tropics between 10°N and 35°S there has been a general freshening. It is most prominent in the Atlantic, and the source of this freshening appears to be in the vicinity of the Congo River outflow. There has been some increase in salinity near Antarctica. With reference to the discussion of the coupled SST distribution in the vicinity of Kerguelen, the SSS also has a similar structure (i.e. error distribution compared to the observations). The scale used in Fig. 10 is such that this feature is not as prominently displayed as for the SST.

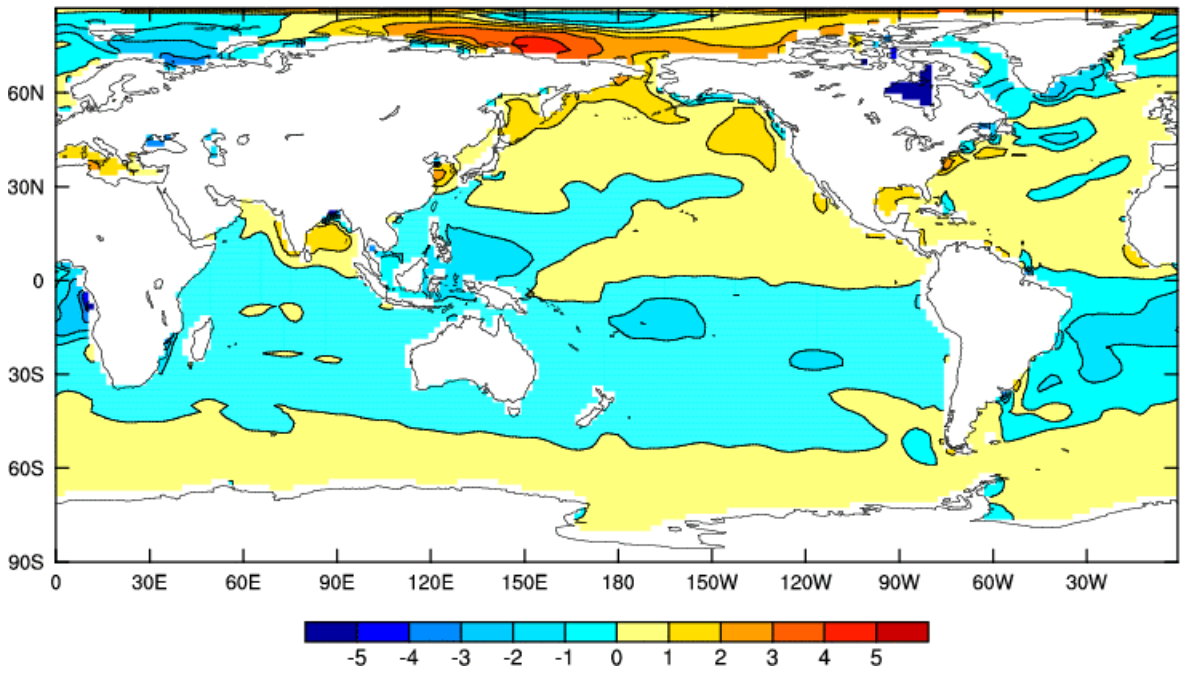

Figure 10. Annual mean SSS (ppt) difference: Coupled minus observations.

During the course of the coupled model run from year 1 to 80, the ocean is no longer under spin-up conditions. During the spin-up, the ocean had restoration conditions for temperature and salinity at the surface (annual cycle). Upon going to coupled conditions, the ocean is subject to freshwater fluxes that contain the following three components: (a) precipitation minus evaporation, (b) river runoff, and (c) freshwater changes associated with ice formation (brine rejection) or ice melting (freshwater input). The heat flux is also subject to feedback processes that were absent before. It is thus to be expected that there will be some change in the overall circulation of the ocean. To illustrate this change, the mean meridional overturning in the ocean in now shown. In Fig. 11, the annual mean overturning in the NH is shown for spin-up conditions (average over last 10 years) and at the end of the 80 year coupled period (average over years 71-80). It is seen that the North Atlantic cell of North Atlantic Deep Water (NADW) has achieved a more realistic amplitude with sinking at 55°N increasing to 15Sv though NADW still does not penetrate deep enough into the ocean in the North Atlantic basin.

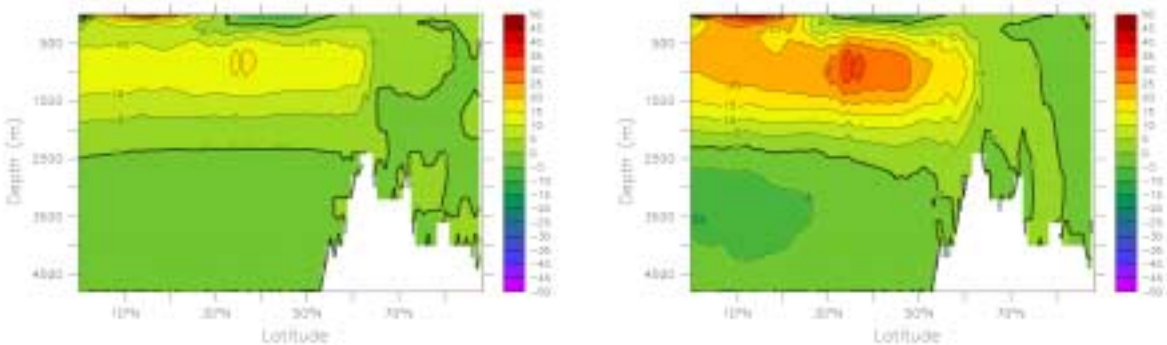

Figure 11. The NH vertical-meridional streamfunction (Sverdrups) for spin-up (left) and coupled (right)

The overturning in the Southern Hemisphere is shown in Fig. 12. Here the influence of the ice processes around Antarctica is readily apparent in the coupled model relative to the spin-up. The streamfunction at 70°S has increased from a weak value of less than 5 Sv in the spin-up to about 15 Sv in coupled mode. This increase in the thermohaline circulation in the coupled model is again viewed as more realistic than the spin up case, with bottom water forming in some locations on the Antarctic shelves. The increased circulation in the diagram is due to greater convection driven by brine released from the sea-ice.

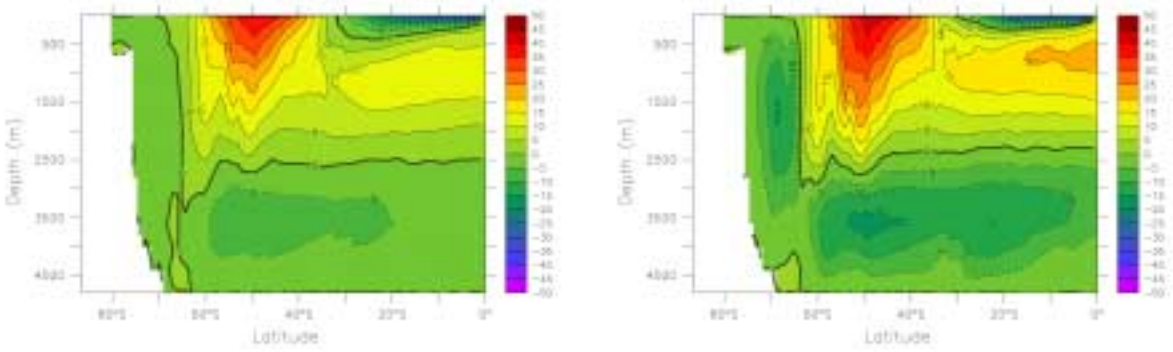

Figure 12. The SH vertical-meridional streamfunction (Sverdrups) for spin-up (left) and coupled (right)

The model showed some cooling over the 80-year period, and there was some change in the ice cover and total ice volume. The ice volume for the Arctic region in particular showed a significant increase (Fig. 13). The full mechanism of this increase is still being investigated but as the climate has cooled there is less melting in summer, and with the same ice growth in winter the model will find a new equilibrium for the ice thickness distribution. In the SH, the ice cover initially retreated as the convection mentioned above brought warmer water to the surface, the system then cooled and the ice amount recovered.

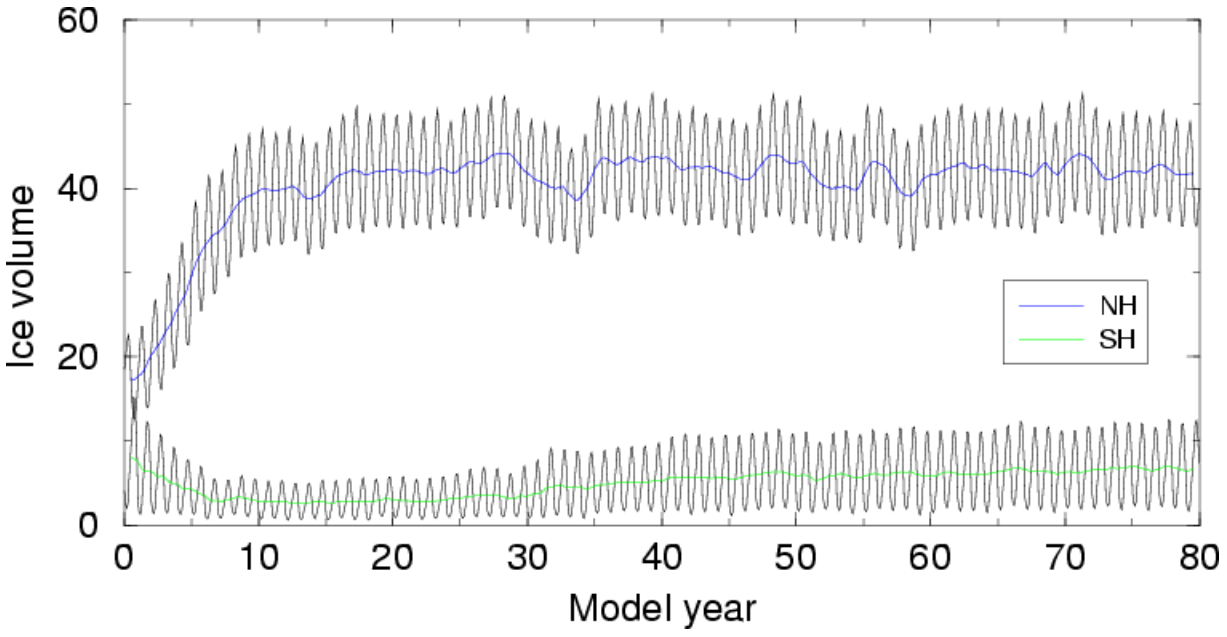

Figure 13. The coupled model NH and SH ice volume (10^3 km^3)

As shown in Figs. 14 and 15, the horizontal extent of the ice coverage and seasonal cycle of ice cover did not alter a great deal between uncoupled and coupled conditions in the either hemisphere. The ice cover during the AGCM control run (uncoupled) is shown in Fig. 14. Here the April and September ice extent is shown for the NH, and September and February for the SH which represent the seasons of maximum and minimum extent.

In the SH the seasonal ice extent and thickness patterns are very similar in both simulations with maximum ice thickness on the western coasts of the Weddell and Ross Seas. The ice has retreated a little in the sectors South of Africa to South of Australia where the surface ocean has warmed in the simulation compared to observations (Fig. 8). Both model climatologies are a realistic compared to observations.

In the NH as noted above the ice thickness has increased in the coupled model. The seasonal ice extent is similar in the North Pacific sector but slightly more extensive in the Greenland and Barents seas in both seasons as the thicker ice takes longer to melt as it is advected south to warmer waters. This increased ice cover is consistent with the cooling shown in both these regions in Fig. 8. The observed pattern of ice thickness (not shown) is derived from submarine data and indicates a maximum to the north of Greenland and along the Canadian Archipelago. Neither the ice-atmosphere model spin up nor the coupled model match this distribution satisfactorily. A possible cause may be that the atmospheric model winter wind stress climatology is not realistic. A realistic maximum ice volume is of the order of 30×10^3 km^3, and so in the coupled model the ice volume is somewhat too large, but as the NH has cooled this is not an unexpected response.

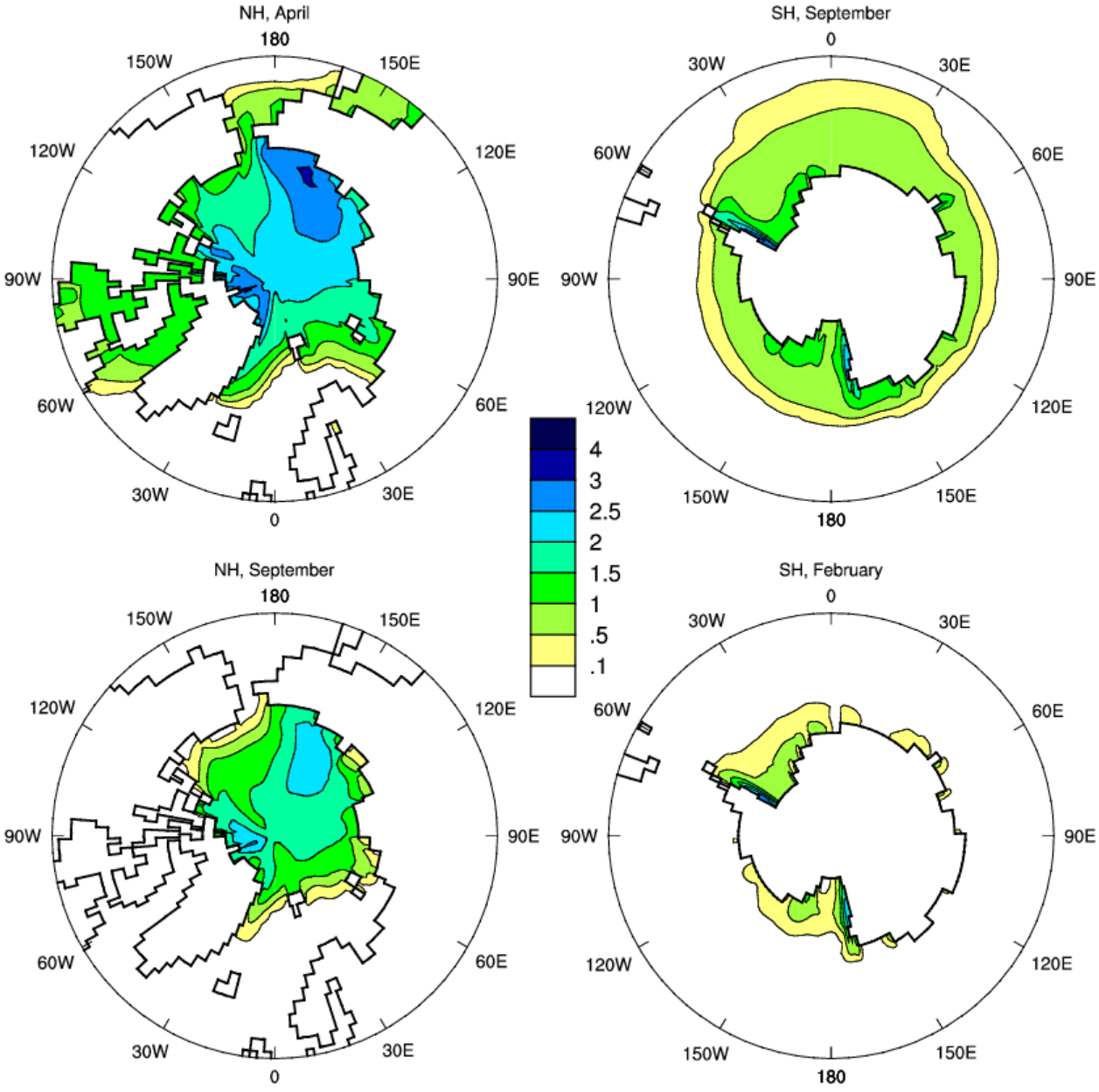

Figure 14. The ice thickness (*m*) for the AGCM spin-up

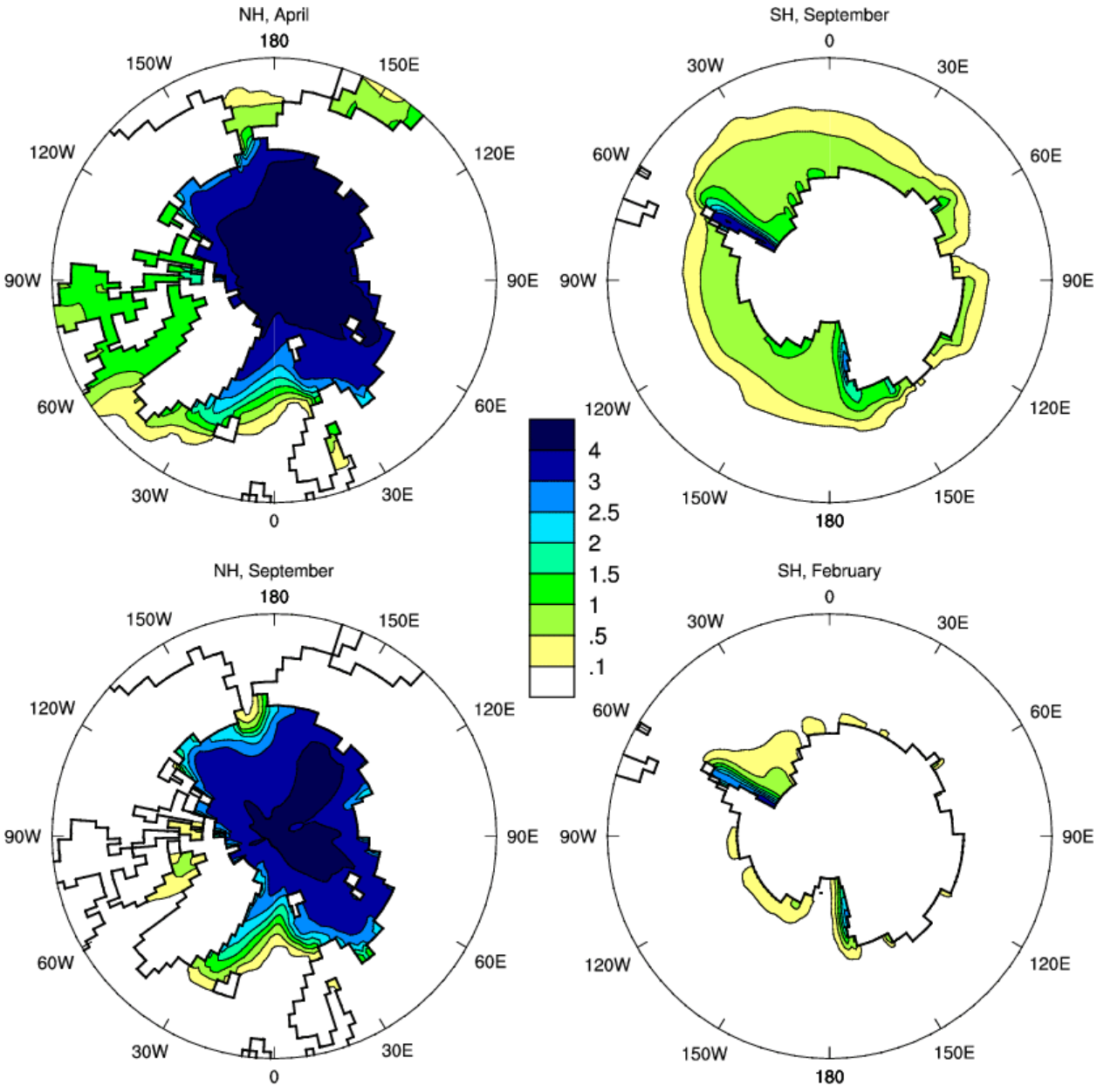

Figure 15. The ice thickness (*m*) for the Coupled model (years 71-80)

Some of the coupled model responses at the surface discussed above (ice behaviour, sea surface salinity changes) may be linked to the precipitation (rainfall and snowfall) patterns in the model. For example, the precipitation over land leads to runoff which feeds directly into the oceans. The modelled precipitation pattern is shown in Fig. 16 for the seasons of Dec-Feb, and Jul-Aug. For comparison, the observed precipitation (Xie and Arkin 1997) is also shown in Fig. 16. (The gridded data for this observational data set is available by anonymous ftp from ftp.ncep.noaa.gov and is in the directory /pub/precip/cmap/).

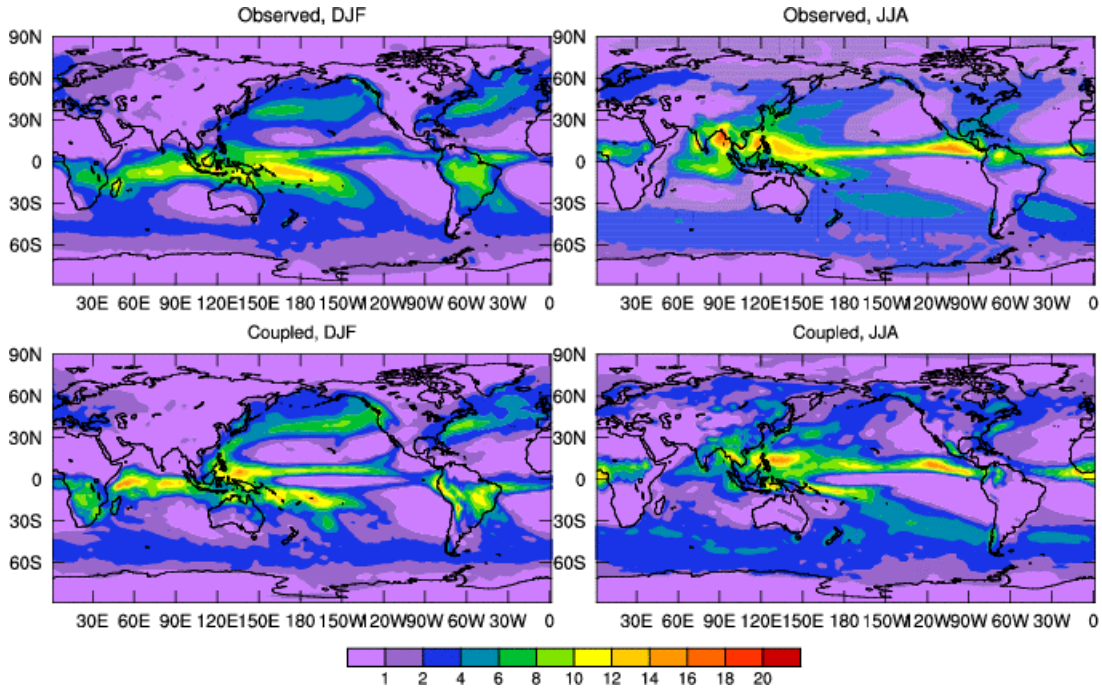

Figure 16. Rainfall (mm/day): Observations (Xie and Arkin 1997) and coupled model (years 71-80); December-February on left and June-August on right.

In both seasons (DJF and JJA), the coupled model reproduces the observed rainfall pattern with a considerable degree of realism. However, there are some noteworthy differences. In DJF, in the tropical Pacific the coupled model has double, rather than a single ITCZ. This appears to be a common problem with coupled models which have a too pronounced cold tongue in the tropical SSTs. The colder water along the equator, with warmer water to either side causes the tropical convection centers to be moved over these warmer waters. Over South America, there is a tendency for the rainfall to be too strongly centered over the higher topography regions. There also appears to be too much rainfall in the India Ocean. In JJA, the Indian monsoon is not strong enough, although in the uncoupled AGCM, the Indian monsoon is much closer to the observed pattern (not shown). Thus the coupled model JJA SST pattern may be having some adverse effect on the monsoon. The summer rainfall over the USA is also too weak, which in turn leads to the Mississippi River outflow being too weak.

Over Australia, the modelled rainfall is quite good. The rainfall pattern for Australia in DJF is shown in greater detail in Fig. 17. This is for the model period years 71-80. The pattern of the rainfall is in broad agreement with the observations, and the Australian monsoon is well represented. However, the model does tend to produce too much rainfall in DJF over the southern part of the continent. In order to show the seasonal behaviour of the modelled rainfall,

the monthly climatology of northeast Australian rainfall is shown in Fig. 18. The observed seasonal rainfall is also shown, and it is clear that the Mk3 coupled model is well able to not only capture the correct seasonality, but also the correct amounts for this region.

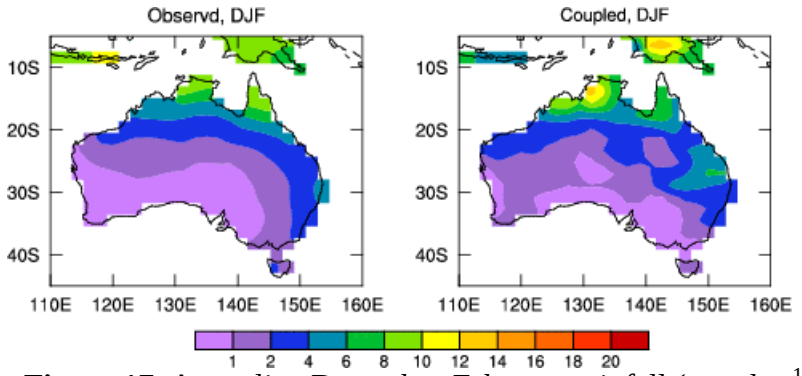

Figure 17. Australian December-February rainfall (*mm day*$^{-1}$). Observations (left) and coupled model (right).

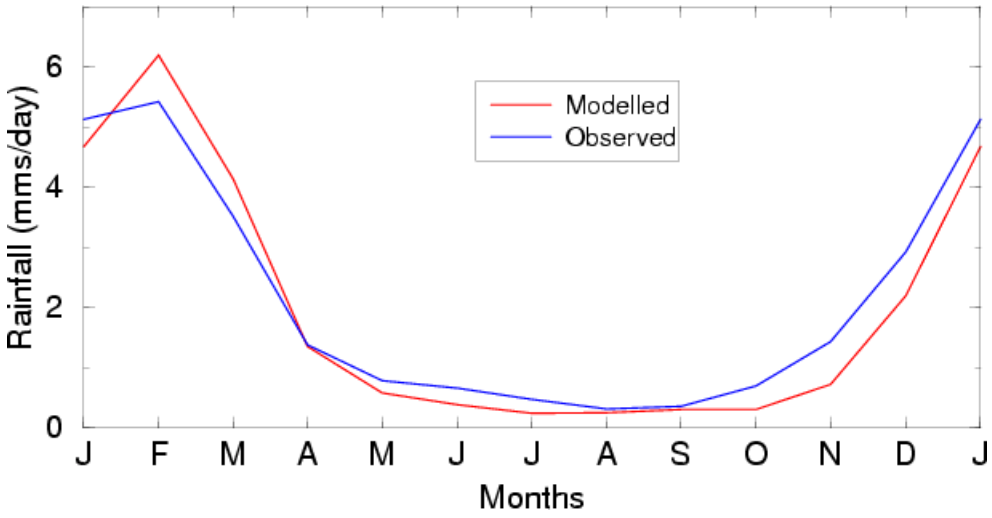

Figure 18. Monthly climatology of northeast Australian rainfall (*mm day*$^{-1}$).

The climatological rainfall values are the long-term average of interannual rainfall fluctuations, which for the northeast Australian region is strongly influenced by ENSO teleconnections. The realistic simulation of the climatologies indicates that the ENSO teleconnections over the region are reasonably simulated. To demonstrate the ENSO behaviour in the coupled model, the tropical Pacific SST anomalies (4°S to 4°N) are shown in Fig. 19. These monthly anomalies are relative to the average monthly SSTs over the 80-year model control run. There are three panels, with years 20-40, 40-60, and 60-80 being shown as Hovmoller plots. There are a considerable number of events (El Niño and La Niña type) throughout the period. At years 66 and 67 there is a pair of events which show much stronger anomalies than usual. Overall the magnitudes of the El Niño events are of comparable magnitude to, or even slightly stronger than the observed events.

The Southern Oscillation Index (SOI) is defined, following Troup (1965), as the standardized anomaly of mean sea level pressure difference between Tahiti and Darwin. The Niño3.4 SST (average over 170°-120°W, 5°S-5°N) index is an oceanic surrogate of the SOI. The modelled

and the observed indices are plotted in Fig. 20. The observed are based on the Global Ice and Sea Surface Temperature (GISST) data set where the monthly climatology is obtained by averaging the 48 monthly mean fields for each month over the period 1950-1997. The standard deviation of the modelled Niño3.4 over the 80 years is 0.95°*C*, and for the observed over the period 1920-2000 is 0.76°*C*. Thus in terms of the Niño3.4 index, the model ENSOs have amplitudes that tend to be larger than the observed.

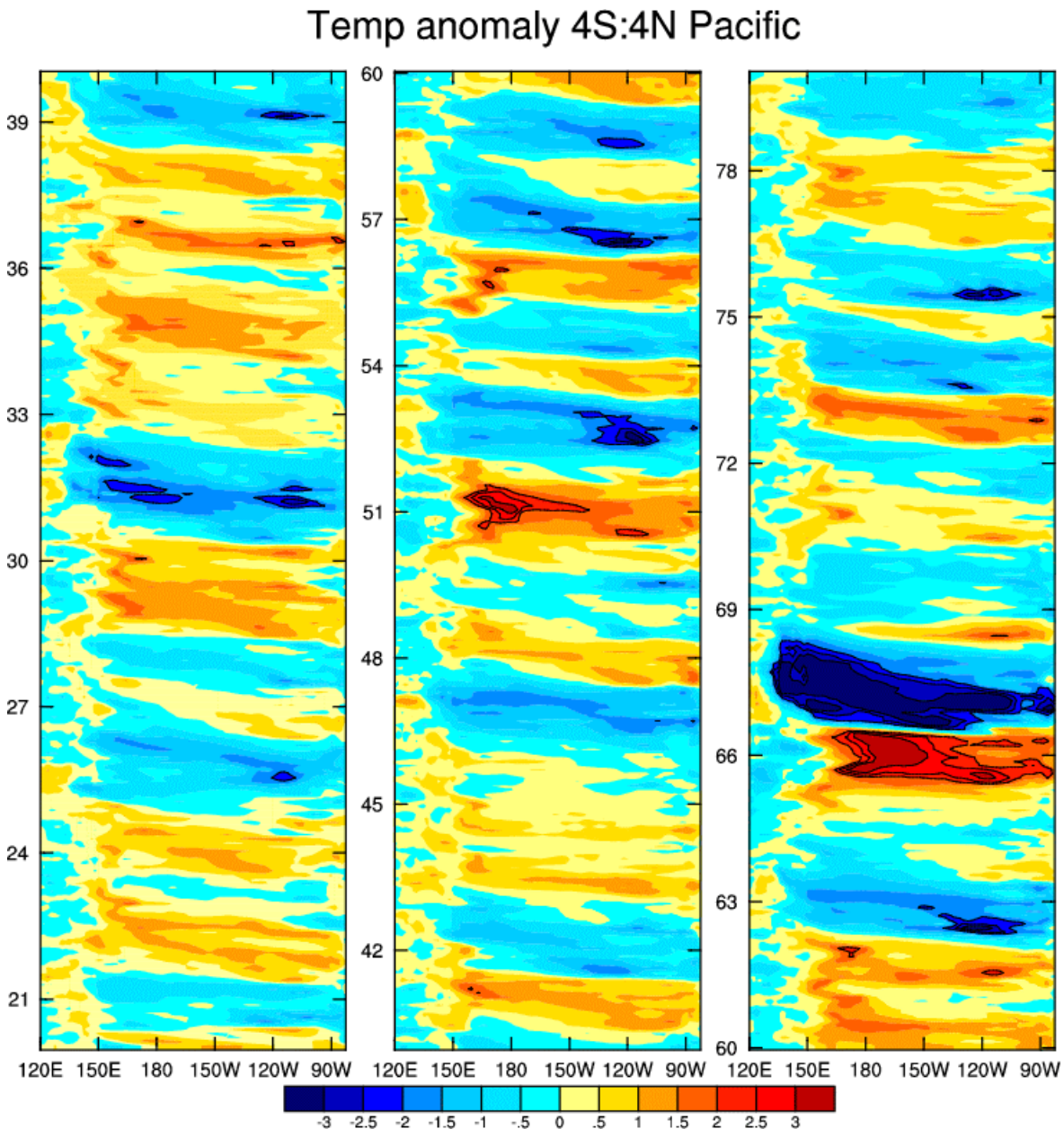

Figure 19. Evolution of temperature anomalies (°*C*) across the Pacific for the coupled model: Years 20-40 (left), 40-60 (middle), 60-80 (right).

The strong El Niño event at around year 67 is clear in the index. The positive Niño3.4 index exceeds 3°*C*, which is a value comparable to a value reached by recent El Niño events, for example, the 1983 and 1997 episodes. The strong El Niño event is followed by a strong La Niña event. The La Niña event has a larger anomaly amplitude than the El Niño event preceding it.

The physical mechanism leading to the occurrence of this so-called “super-ENSO pair” has been investigated, and a full analysis has been undertaken (W.J. Cai, M.A. Collier, H.B. Gordon and L.J. Waterman, 2002: “Strong ENSO variability and a super-ENSO pair in a coupled climate model” - submitted for publication.)

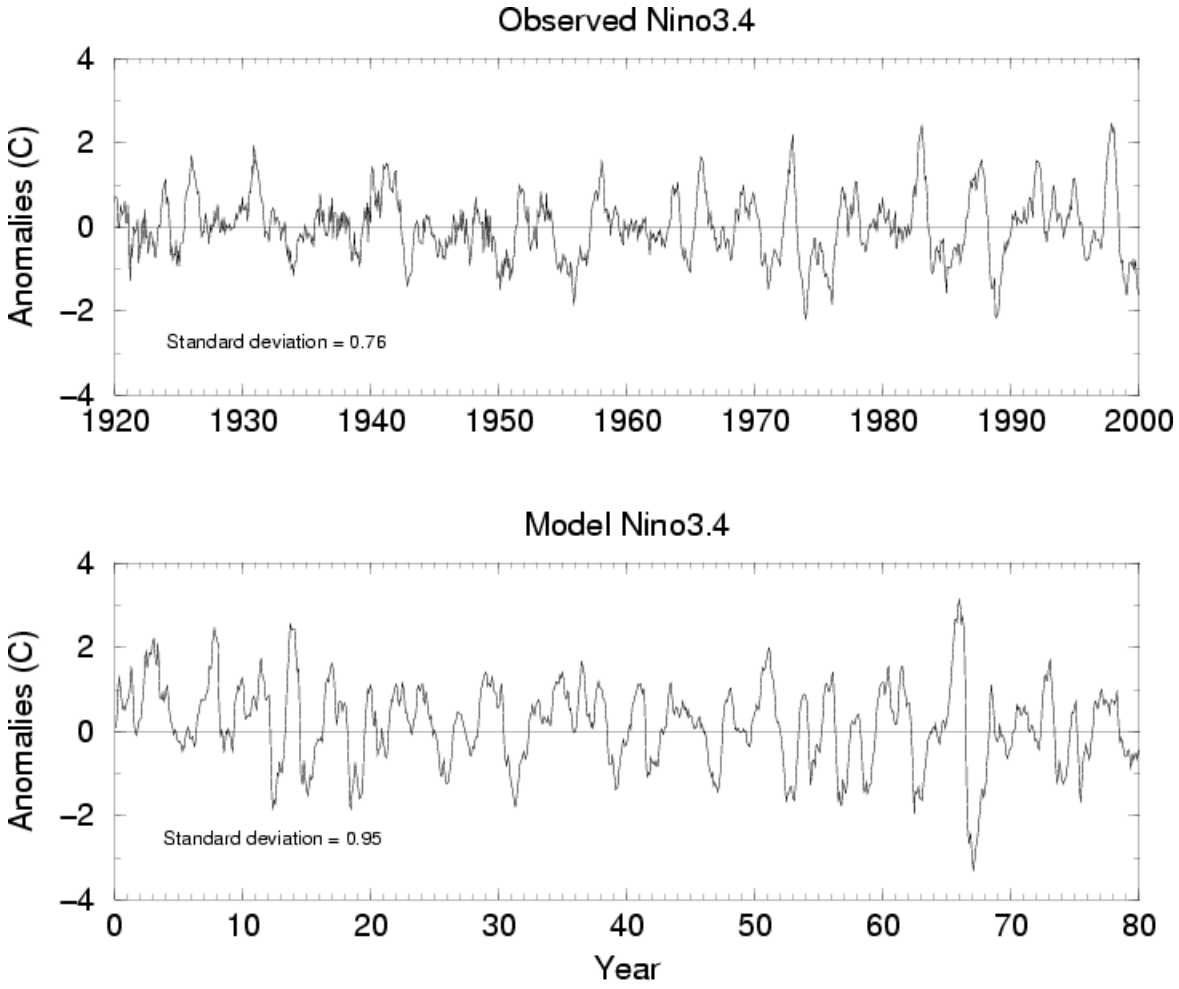

Figure 20. Time series of observed (top) and modelled (bottom) Niño3.4 index (°*C*).

Overall, the coupled model behaviour is quite similar to the behaviour of the separate AGCM and OGCM stand alone components. Apart from the small cooling trend over the 80-year period, the model appears to be quite stable under coupled conditions, and the absence of any flux adjustments (which could have been applied) is well justified. The sea-ice component of the coupled model is a sensitive indicator of the performance of the coupled system, and any serious deficiencies in the model soon become apparent in the polar regions. The Mk3 model control run reported here has shown that the current coupled model is well behaved, although it could be made better by a reduction in the model drift (cooling). Every effort is now being made to determine the cause of this drift, and a subsequent version of the Mk3 model now under development is expected to largely eliminate this drift

23 Transient model response to global atmospheric change

In this section we examine the transient behaviour of the Mk3 coupled model under an IPCC scenario of atmospheric composition change, and compare the response in key climate variables to corresponding periods from the control experiment. In the transient experiment, the atmospheric concentrations of greenhouse gases (expressed as an equivalent CO_2 concentration) and stratospheric ozone, and the direct effect of sulfate aerosols, are varied according to the A2 SRES scenario (see Fig. 5(b), Climate Change 2001), starting 1961 and ending at 2100 (see Fig. 21). The climate change experiment commenced at the end of year 120 of the control integration. Computational time constraints meant that our initial climate change experiment was not able to be integrated from pre-industrial conditions, and therefore a "cold-start" problem occurs, where the integrated effect of varying atmospheric conditions prior to 1961 is not included in the thermal response. Our most recent transient experiment (to be reported elsewhere) starts from 1871, thereby circumventing the cold start problem.

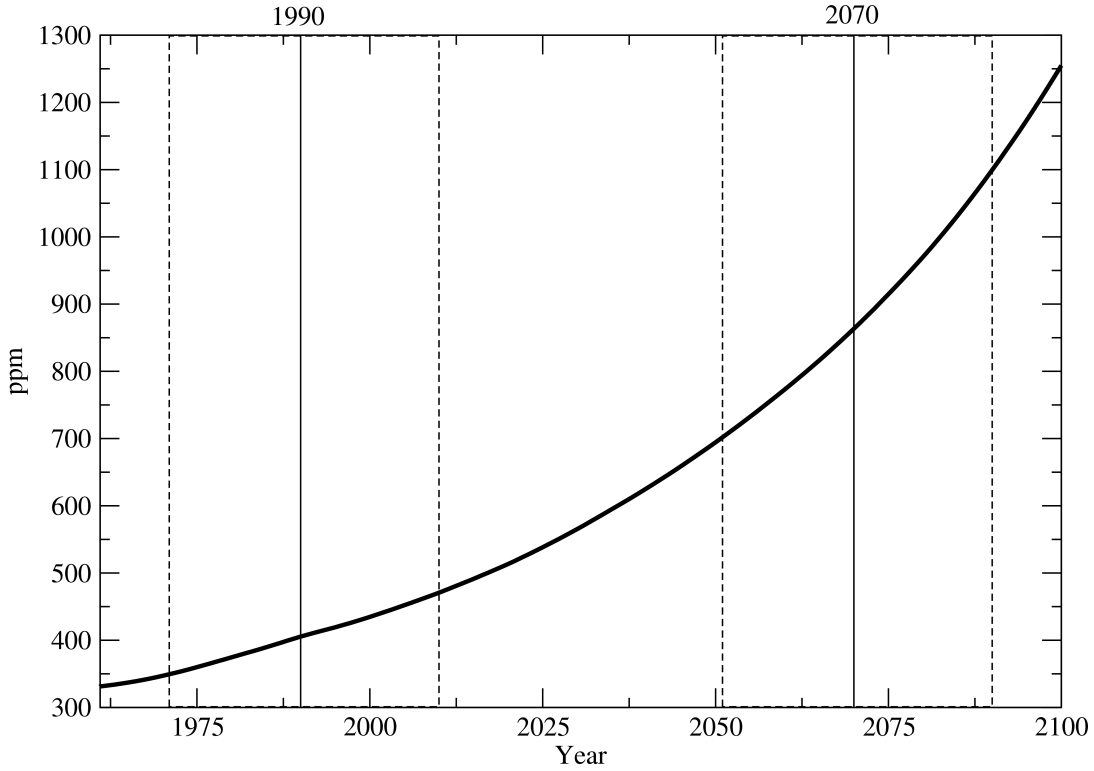

Figure 21. Equivalent CO_2 concentration scenario (SRES A2) used in transient experiment between 1961 and 2100 (ppm). The dashed boxes and vertical lines are shown here for convenience as the 40-year periods which they represent will be discussed later in this section.

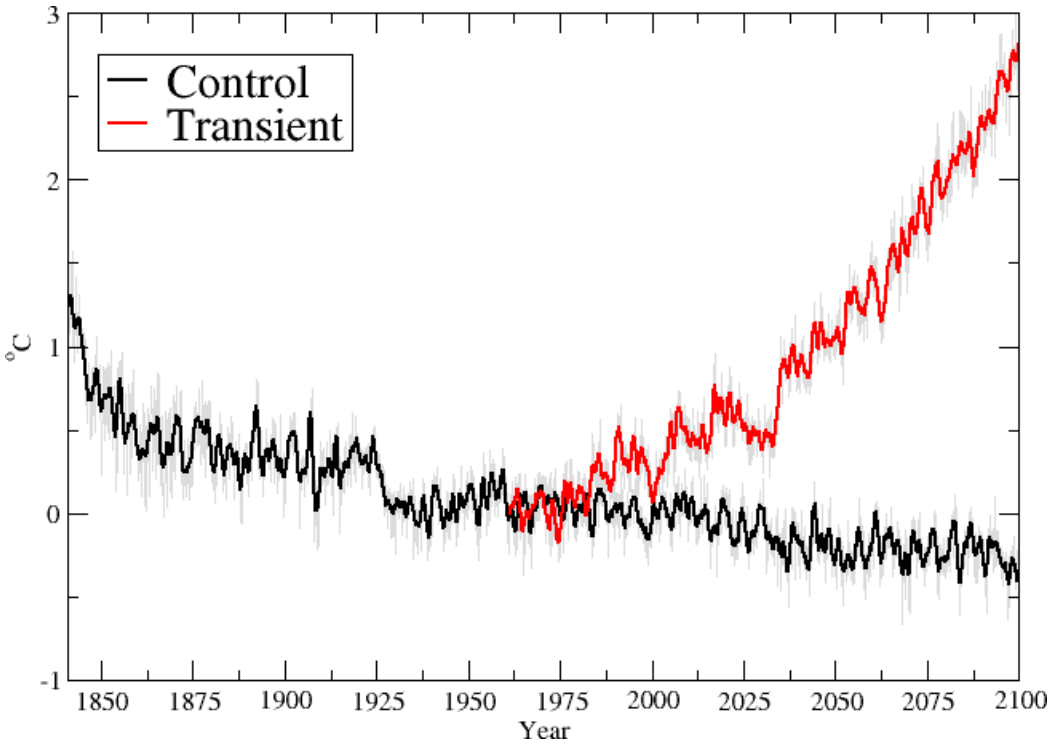

Figure 22. Time series of globally averaged anomalies for surface screen temperature for control and transient experiments. Anomalies are relative to the period 1980-2020 of the control integration. Shown in the light curves are monthly anomalies, and in thick coloured lines 12-month running means.

Figure 22 shows the monthly globally averaged (over all surface types including vegetated land, ocean and ice) surface screen temperature anomalies for both the control and transient experiment. First note that although a calendar year time-axis has been attached to the control experiment results, it is only for the convenience of comparison with results from the transient experiment. In all monthly anomalies present in this section, we have used a base climate generated from years 1981-2020 of the control integration (i.e., model years 141-180). In all, the control experiment has been run for 260 years. By the year 2100 of the transient experiment the warming is about 2.8°*C*. The control integration exhibits a 0.25°*C* cooling drift from 1961-2100, so, allowing for this, the effective warming of the transient integration to 2100 is a little over 3°*C*. The extent of this warming lies within the range of the IPCC A2 ensemble of model results, though is modestly less than the ensemble mean of about 3.8°*C* (see Fig. 5(d), IPCC SPM 2001). However, note that there is substantial interannual variability exhibited by this model about the long-term warming trend.

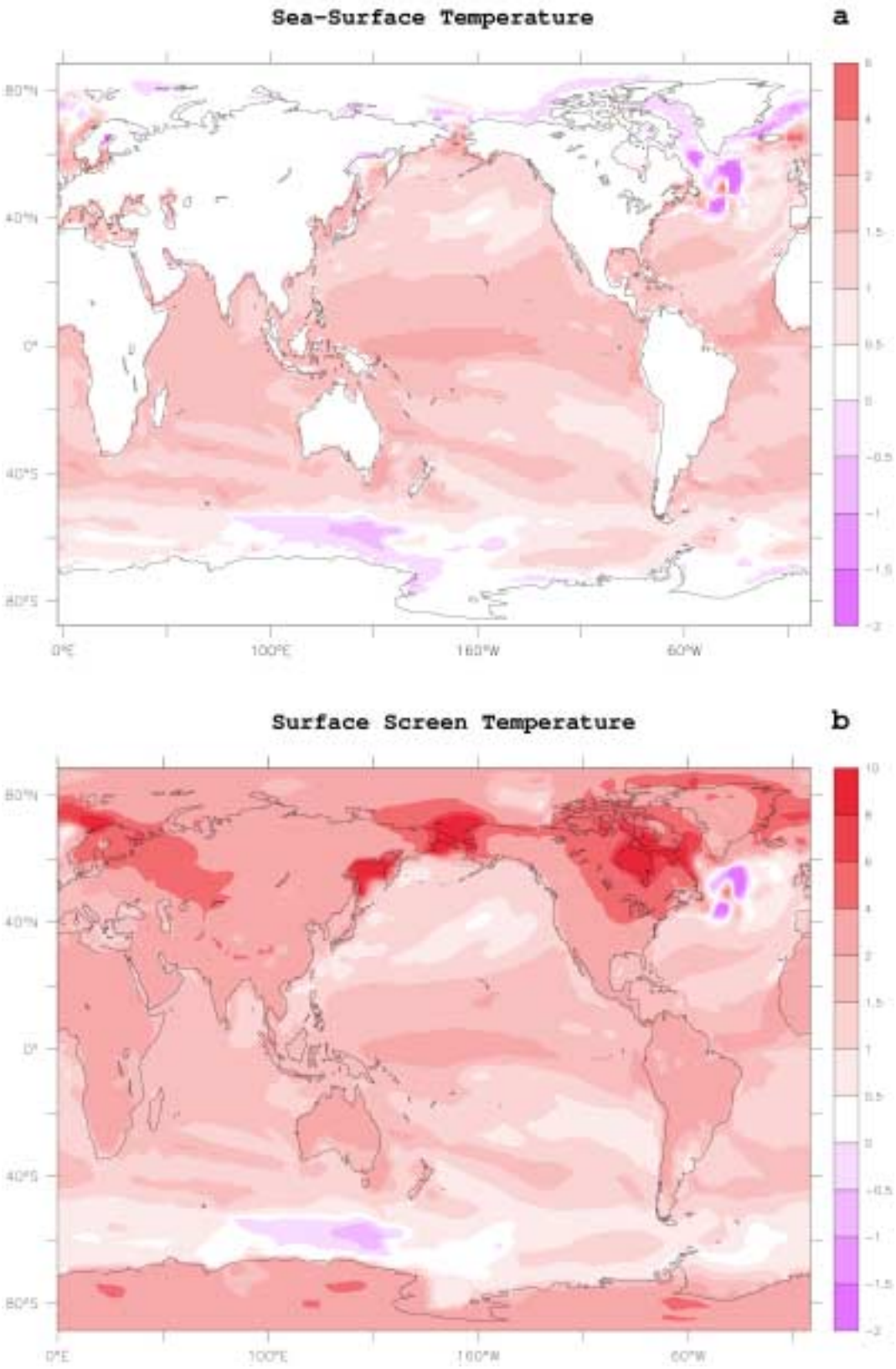

Figure 25. Annually averaged sea-surface temperature (a) and surface screen temperature (b) difference between 40-year climatology centered at year 2070 for transient and control experiments (°*C*). Note that the colour palette has been chosen to be the same for the contour intervals between –2 and 6°*C* in both (a) and (b).

Fig. 25 shows the difference in (a) global sea-surface temperature and (b) surface screen temperature between the transient and control experiments for the 40-year period centered on the year 2070. Over the oceans, the patterns of difference for the sea-surface and surface air temperatures are quantitatively similar. The largest warming occurs at high northern latitudes, however surface air temperatures over Antarctica and the Ross and Weddel Seas also increase significantly in this model. Large changes in surface air temperature over the oceans at high latitudes partly reflect reduction in sea-ice coverage. The equatorial regions show significant warming, typically of around 1.5°*C*, and slightly higher in parts of the Pacific and Atlantic basins. The regions of the large subtropical gyres show relatively weak warming. The least warming (even some limited cooling) is found in parts of the high latitude Southern Ocean and North Atlantic ocean. The warming due to radiative forcing change is mitigated in these latter regions by changes in the large-scale currents and stratification which reduce the oceanic transfer of heat to the ocean surface layers.

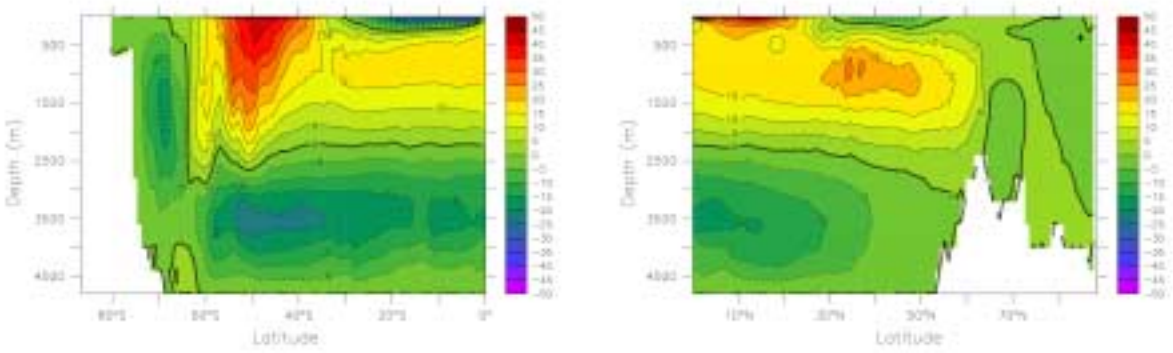

Figure 26. The SH/NH vertical-meridional streamfunction for the control experiment (Year 2091-2100 average, Sverdrups).

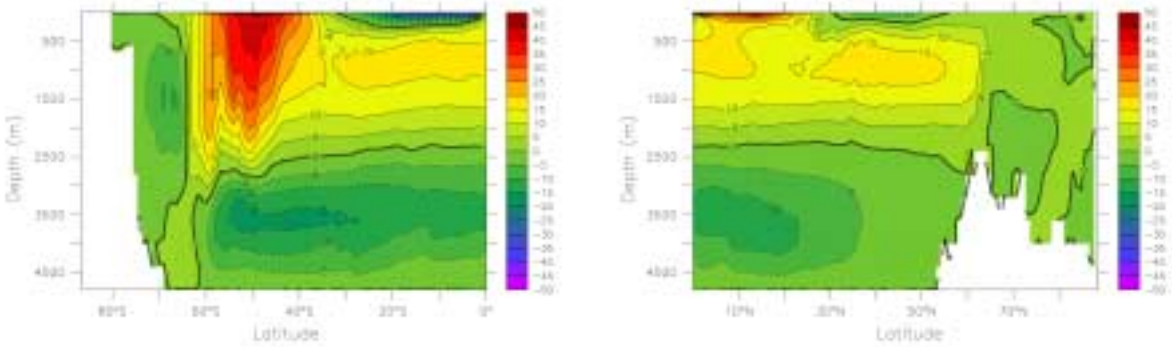

Figure 27. The SH and NH vertical-meridional streamfunction for transient experiment (Year 2091-2100 average, Sverdrups).

Now we turn our attention to the meridional overturning in the global ocean. Shown in Fig. 26 and Fig. 27 is the overturning circulation for the SH and NH averaged over the period 2091-2100 in the control and transient experiments, respectively. Fig. 26 can be compared with the results for an earlier period of the control experiment (Fig. 11b and Fig. 12b), where the main changes are some weakening of the North Atlantic overturning circulation and some strengthening of the

deep circulation cell (centered near 3500 *m* depth), associated with slow adjustment of the ocean to the coupled model surface boundary conditions. The strength of the Antarctic overturning cell (centered near 68°S) remains largely unchanged. The result for the same period (2091-2100) for the transient experiment is shown in Fig. 27. There is a clear reduction in each of the abovementioned overturning cells. The weakening of the North Atlantic and Antarctic overturning circulations indicates a marked reduction in deep and bottom water formation, which plays a vital role in ventilating the deep ocean. Interestingly, the shallow (upper 200 *m*) wind-driven circulation in the SH tropics/subtropics is essentially unchanged, however the corresponding circulation in the NH is weakened by about 5 Sverdrups, predominantly because of changes in the larger scale North Atlantic overturning. The geographical extent of all major cells is essentially unchanged. Further investigation is required to understand the processes which bring about these changes in the world's oceans, and some caution is required in the interpretation of these results given the significant drift and vacillations that exist in some of the overturning circulations.

Figure 28 depicts Australian average temperature, precipitation and precipitation-minus-evaporation anomalies for the control and transient runs. The calculation here includes Australian land points only (c.f. Fig. 22). The overall warming for the period from 1961 to 2100 is about 3.4°*C*. The drift in the control simulation is 0.25°*C* from 1961-2100 and must be subtracted when estimating the overall warming, giving a net warming of about 3.6°*C*. The Australian average precipitation and precipitation-minus-evaporation (net moisture from the atmosphere to the land surface) exhibit no significant trend throughout the transient experiment, either in absolute value or in the range of variability. The lack of trend in the latter variable implies that there is no substantial trend in the net runoff from the Australian continent. However, regional and seasonal trends may be significant.

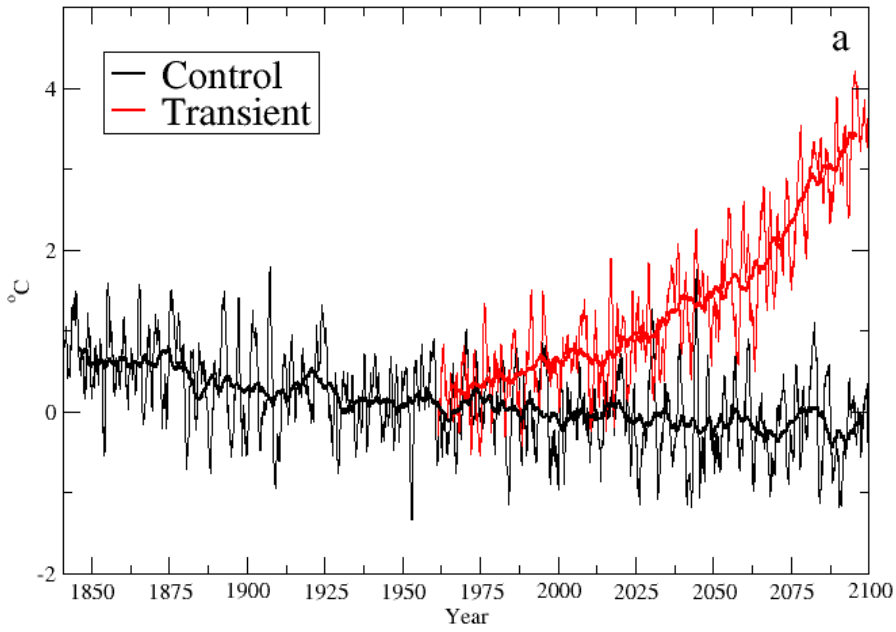

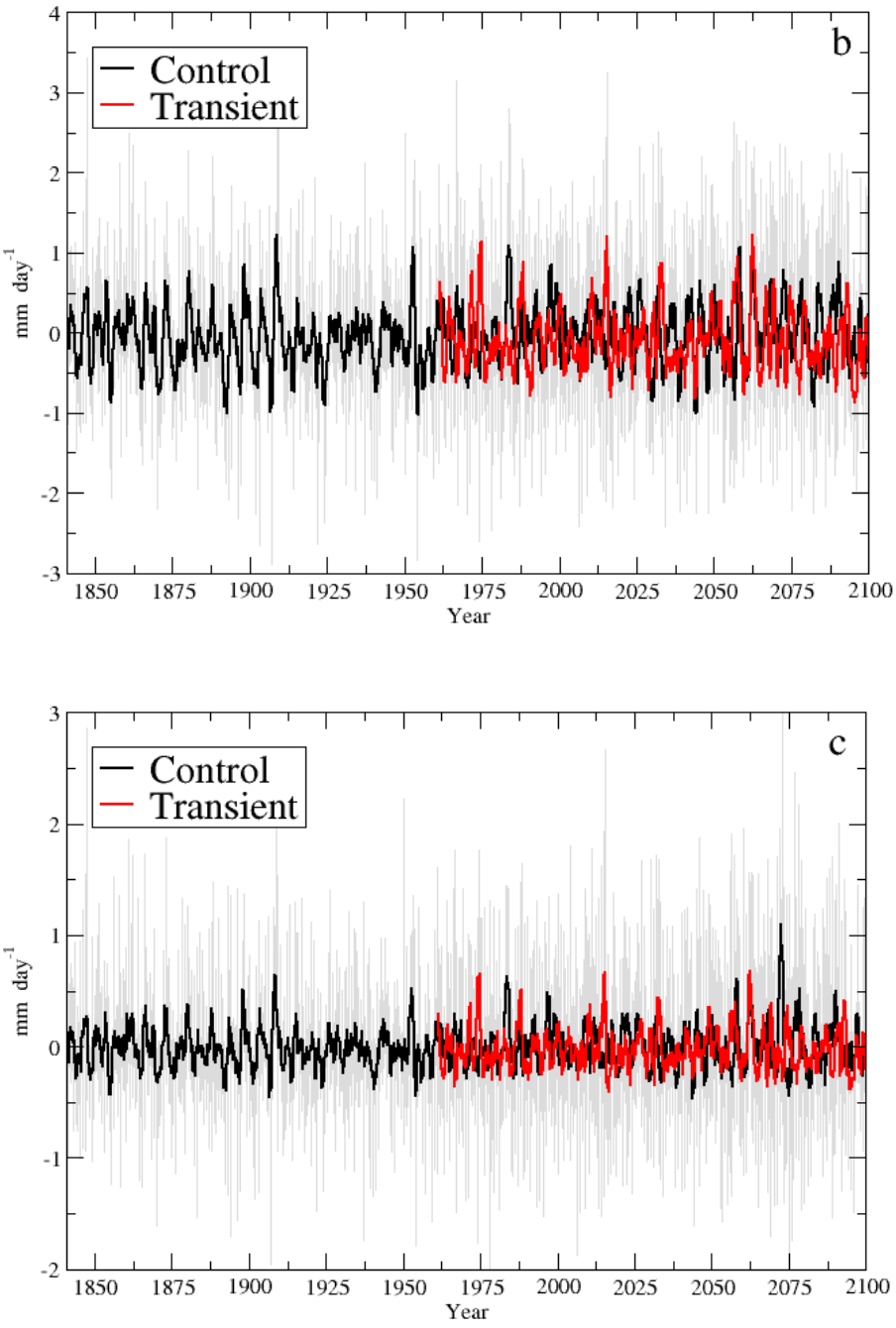

Figure 28. Time series of Australian (land-only) averaged anomalies of (a) surface screen temperature, (b) precipitation and (c) precipitation-minus-evaporation for control and transient integrations. The temperature is sampled with a 12- and 120-month running mean, to emphasise interannual and interdecadal variations (no monthly anomalies shown). Rainfall and precipitation-minus-evaporation plots have monthly anomalies and data sampled with a 12-month running mean to emphasise interannual variations.

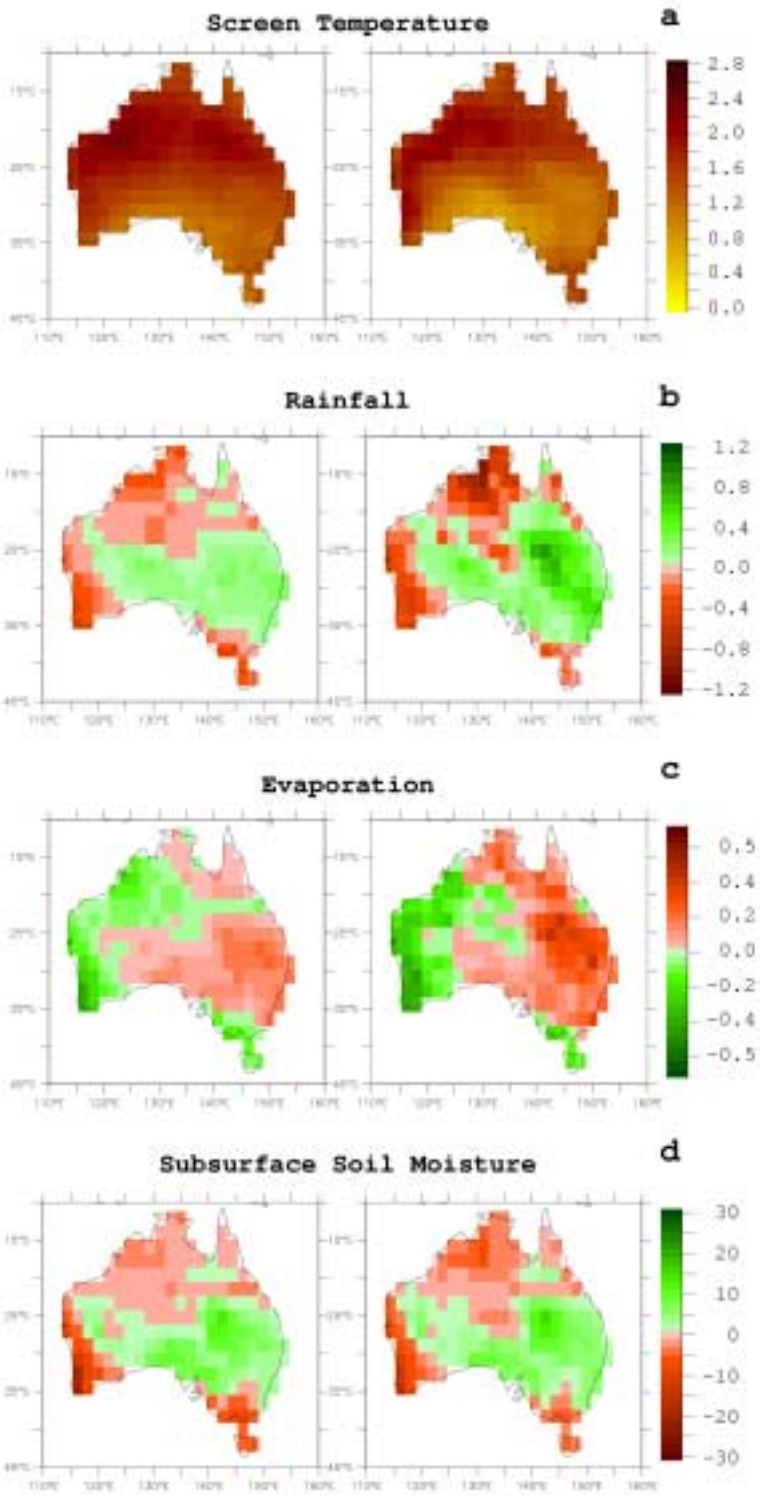

Figure 29. Difference maps over Australia of (a) surface screen temperature, (b) rainfall, (c) surface evaporation and (d) deep soil moisture (°*C*, *mm day*$^{-1}$, *mm day*$^{-1}$ and dimensionless respectively) for annual averaged (left panels) and summer time conditions (December-January-February average, right panels), between 40-year climatologies centered on year 2070 and 1990.

Changes in surface screen temperature, rainfall, evaporation and soil moisture for annual and summer (December-January-February average) conditions over Australia are given in Fig. 29. These are difference maps of 40-year climatologies centered at 2070 and 1990 in the transient experiment. These time periods are schematically shown by dashed rectangles in Fig. 21, and are centered on the solid vertical lines as shown. Fig. 24a shows warming over the entire continent, with changes in excess of 2°*C* to the north and west of Australia. In the summer season the warming is reduced in most southern regions when compared with the annual average difference. The rainfall difference pattern (b) is more complicated. The largest annual reductions are found in the Northern Territory and South-Western Western Australia, and some increase is seen over northern New South Wales (NSW) and central Queensland (Qld). The summer pattern signals a substantial reduction in rainfall in the top-end region. The net moisture to the land-surface is given by precipitation minus evaporation, and is given by figures (c). Note that the colour bar is reversed compared to the rainfall colour bar. This is because rainfall and evaporation operate in the opposite sense, and to indicate drying (brown colours) or moistening (green colours) in the difference plot. Clearly, we see that rainfall and evaporation are nearly always positively correlated. That is, when the climatological rainfall at the surface is large, we observe a large evaporation in the negative sense. To a large degree the pattern of rainfall minus evaporation (and rainfall itself) change is also evident in the soil moisture changes for the deep soil (d). Like the rainfall and evaporation difference distribution for Australia, the soil moisture distribution is quite similar between the annual and summer periods. In addition to the net flux of water at the land surface, the soil type, which varies dramatically across Australia, also plays a major role in the retention of water, and the climatological soil moisture. For the annual and summer periods, the biggest reductions are seen to the north and west of the continent, and the biggest enhancements in northern NSW and central Qld. An ensemble of experiments is required to test the robustness of the regional changes shown here.

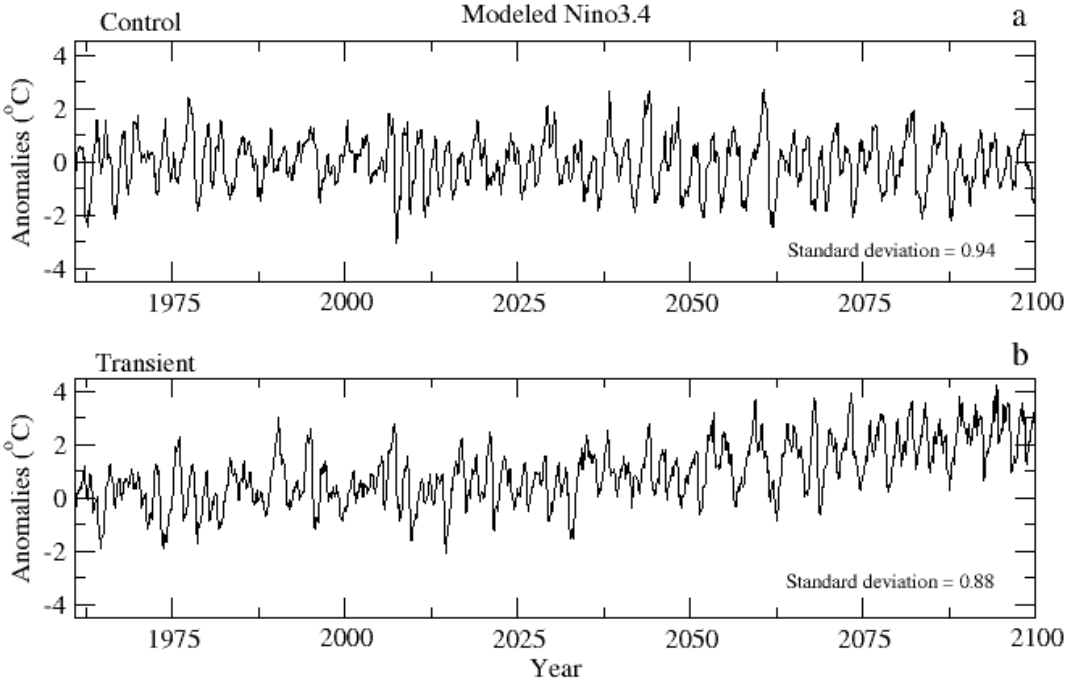

Figure 30. Time series of control (top) and transient (bottom) Niño3.4 index (°*C*).

Finally, in our comparison between the control and transient experiments, we briefly examine the behaviour of ENSO via the Niño3.4 index, which is defined as the area average of the monthly anomaly of SST over the geographical box defined by 5°S-5°N and 150°W-90°W. The control (a) and transient (b) results are shown in Fig. 30. Before we calculate the standard deviation for both of these series we have removed the overall trends. The control Niño3.4 time-series is for the last 140 years of the experiment, as for other figures shown in this section. The control standard deviation is 0.94, and the overall character is similar to that shown in Fig.20, with some interesting new features including a transitory phase of strong biennial oscillations starting around year 2006. In the transient Niño3.4 time-series the warming trend is evident and the standard deviation is slightly less than that for the control at 0.88. Further investigation is required to examine if there are any significant behavioural changes in ENSO under warming conditions in the Mk3 model, however, at this stage any changes appear to be small. The new transient experiment integrated from 1871-2100 may shed further light on whether changes under enhanced greenhouse conditions are significantly different to present conditions. However, to fully test the significance and robustness of climate projections a larger ensemble of experiments should be undertaken.

24 Acknowledgements

We would like to thank other members of the Earth Systems Modelling Program (part of CSIRO Atmospheric Research) who have contributed in various ways (including analysis of model results and data preparation) to the development of the Mk3 climate system model. The support and encouragement of Barrie Hunt (Climate Modelling Program Leader) and Graeme Pearman (Chief of CSIRO Atmospheric Research) in the development of the Mk3 climate model is particularly acknowledged. We also thank Drs. Stuart Godfrey and Trevor McDougall of CSIRO Marine Research for their suggestions and encouragement regarding parameterizations used in the Mk3 oceanic component. Helpful comments on the manuscript were provided by Bob Cechet, Barrie Hunt, and John Garratt. The computations and analysis were performed on the NEC SX-5 and Cray J90 computers at the CSIRO/Bureau of Meteorology Joint High Performance Computing and Communications Centre (Melbourne, Australia). The development of the Mk3 climate system model forms part of the CSIRO Climate Change Research Program, and has been funded in part by the Australian Greenhouse Office.

25 References

Anderson, E.A., 1976: A point energy and mass balance model of snow cover. Office of Hydrology, NOAA Tech. Rep. NWS 19, Washington, D. C., 150 pp.

Akima, H., 1970: A new method of interpolation and smooth curve fitting based on local procedures. *J. Assoc. Comput. Mach.*, **17**, 589-602.

Arakawa, A., 1972: *Design of the UCLA general circulation model. Numerical Simulation of Weather and Climate*. Technical Report No. 7., Dept. of Meteorology, University of California, Los Angeles.

Barnett, T.P., 1999: Comparison of near-surface air temperature variability in 11 coupled global climate models. *J Climate*, **12**, 511-518.

Bi, D., W.F. Budd, A.C. Hirst and X. Wu, 2001: Collapse and reorganisation of the Southern Ocean overturning under global warming in a coupled model. *Geophys. Res. Lett*., **28**, 3927-3930.

Blackadar, A.K., 1962: The vertical distribution of wind and turbulent exchange in a neutral atmosphere. *J. Geophys. Res*., 67, 3095-3102.

Boer, G.J., N.A. McFarlane, R. Laprise, J.D Henderson and J.-P. Blanchet, 1984: The Canadian climate center spectral atmospheric general circulation model. *Atmos. Ocean*, **22**, 397-429.

Boucher, O., and U. Lohmann, 1995: The sulfate-CCN-cloud albedo effect. A sensitivity study with two general circulation models. *Tellus*, **47B**, 281-300.

Bourke, W., 1974: A multi-level spectral model. I. Formulation and hemispheric integrations. *Mon. Wea. Rev*., **102**, 687-701.

Bryan, K., and L.J. Lewis, 1979: A water mass model of the world ocean. *J. Geophys. Res*., **84**, 347-376.

Bryan, K., 1984: Accelerating the convergence to equilibrium of ocean-climate models. *J. Phys. Oceanogr.*, **14**, 666-673.

Bunker, A.F., 1976: Computations of surface energy flux and annual air-sea interaction cycles of the north Atlantic ocean. *Mon. Wea. Rev*., **104**, 1122-1140.

Cai, W.J., J.I. Syktus, H.B. Gordon and S.P. O'Farrell, 1997: Response of a global coupled-atmosphere-sea ice climate model to an imposed North Atlantic high-latitude freshening. *J. Climate*, **10**, 929-948.

Cai, W.J., and H.B. Gordon, 1998: Transient responses of the CSIRO climate model to two different rates of CO_2 increase. *Climate Dynamics*, **14**, 503-516.

Cai, W.J., P.G. Baines and H.B. Gordon, 1999: Southern mid- to high-latitude variability, a zonal wavenumber-3 pattern, and the Antarctic Circumpolar Wave in the CSIRO coupled model. *J. Climate*, **12,** 3087-3104.

Cai, W.J., and H.B. Gordon, 1999: Southern high-latitude drift in a coupled model. *J. Climate*, **12**, 132-146.

Cai, W.J., and P.H. Whetton, 2000: Evidence for a time-varying pattern of greenhouse warming in the Pacific Ocean. *Geophys. Res. Lett*., **27**, 2577-2580.

Cane, M.A., 1992: Tropical Pacific ENSO models: ENSO as a mode of the coupled system, in climate system modeling. Ed. K. E. Trenberth, Cambridge University Press, New York, chapter 18, 583–614.

Cess, R.D., and G.L. Potter, 1987: Exploratory studies of cloud radiative forcing with a general circulation model. *Tellus*, **40A**, 460-473.

Cess, R.D, and 33 co-authors, 1996: Cloud feedback in atmospheric general circulation models: an update. *J.Geophys. Res*., **101** (D8), 12791-12794.

Cess, R.D, and 35 co-authors, 1997: Comparison of the seasonal change in cloud-radiative forcing from atmospheric general circulation models and satellite observations. *J. Geophys. Res*., **102** (D14), 16593-16603.

Charnock, H., 1955: Wind stress on a water surface. *Quart. J. Roy. Meteor. Soc*., **81**, 639-640.

Chen, D., A.J. Busalacchi, and L.M. Rothstein, 1994: The roles of vertical mixing, solar radiation, and wind stress in a model simulation of the sea surface temperature seasonal cycle in the tropical Pacific Ocean. *J. Geophys. Res. (Oc.)*, **99**, 20345–20359.

Chen, T.H., and 42 co-authors, 1997: Cabauw experimental results from the Project for Intercomparison of Land-surface Parameterization schemes. *J Climate*, **10**, 1194-1215.

Chouinard, C., M. Beland and N. McFarlane, 1986: A simple gravity wave drag parameterization for use in medium-range weather forecast models. *Atmos. Ocean*, **24**, 91-110.

Connolley, W.M., and S.P. O'Farrell, 1998: Comparison of warming trends over the last century around Antarctica from three coupled models. *Annals Glaciol.*, **27**, 565-570.

Covey, C. and 22 co-authors, 2000: The seasonal cycle in coupled ocean-atmosphere general circulation models. *Climate Dynamics*, **16**, 775-787

Clapp, R.B., and G.M. Hornberger, 1978: Empirical equations for some soil hydraulic properties. *Water Resour. Res.*, **14**, 601-604.

Cox, M.D., 1984: A primitive equation, three-dimensional model of the ocean. Tech. Rep. No. 1, Ocean Group, Geophysical Fluid Dynamics Laboratory, Princeton, NJ, 143 pp.

Cusack, S., J.M. Edwards, and R. Kershaw, 1999: Estimating the subgrid variance of saturation, and its parametrization for use in a GCM cloud scheme. *Quart. J. Roy. Meteor. Soc*., **125**, 3057-3076.

Davies, H.L., and B.G. Hunt, 1994: The problem of detecting climatic change in the presence of climatic variability. *J. Meteor. Soc. Japan*, **72**, 765-771.

Deardorff, J.W., 1977: A parameterization of ground-surface moisture content for use in atmospheric prediction models. *J. Appl. Meteor*., **16**, 1182-1185.

Dickinson, R.E., A. Henderson-Sellers and P.J. Kennedy, 1993: Biosphere-Atmosphere Transfer Scheme (BATS) version 1e as coupled to the NCAR Community Climate Model. NCAR Technical Note NCAR/TN-387+STR, 72 pp.

Dix, M.R., and B.G. Hunt, 1995: Chaotic influences and the problem of deterministic seasonal predictions. *Intl. J. Climatol*., **15**, 729-752.

Dix, M.R., and B.G. Hunt, 1998: Transient climatic change to 3x CO_2 conditions. *Global and Planetary Change*, **18**, 15-36.

DKRZ, 1993: Report No. 6. The ECHAM3 atmospheric general circulation model. Edited by Deutsches Klimarechenzentrum GmbH (DKRZ), Bundesstraβe 55, D-2000, Hamburg 13, Germany.

Dorman, J.L., and P.J. Sellers, 1989: A global climatology of albedo, roughness length and stomatal resistance for atmospheric general circulation models as represented by the simple biosphere model (SiB). *J. Appl. Meteor*., **28**, 833-855.

England, M.H., and A.C. Hirst, 1997: Chlorofluorocarbon uptake in a world ocean model. 2. Sensitivity to surface thermohaline forcing and subsurface mixing parameterizations. *J. Geophys. Res*., **102** (C7), 15709-15731.

Farouki, O.T., 1986: *Thermal properties of Soils*. Series on Rock and Soil Mechanics, Vol. 11, Trans Tech, 136 pp.

Fels, S.B., and M.D. Schwarzkopf, 1975: The simplified exchange approximation: a new method for radiative transfer calculations. *J. Atmos. Sci*., **32**, 1475-1488.

Fels, S.B., and M.D. Schwarzkopf, 1981: An efficient algorithm for calculating CO_2 15μ*m* cooling rates. *J. Geophys. Res*., **86**, 1205-1232.

Fels, S.B., 1985: Radiative-dynamical interactions in the middle atmosphere. *Advances in Geophysics, 28A: Issues in Atmospheric and Oceanic Modeling*, S. Manabe, Ed., Academic Press, 277-300.

Flato, G.M. and W.D. Hibler III, 1990: On a simple sea-ice dynamics model for climate studies. *Ann. Glaciol*., **14**, 72-77.

Flato, G.M. and W.D. Hibler III, 1992: On modelling pack ice as a cavitating fluid. *J. Phys. Oceanogr*., **22**, 626-651.

Francis, P.N., A. Jones, R.W. Saunders, K.P. Shine, A. Slingo and Z. Sun, 1994: An observational and theoretical study of the radiative properties of cirrus: Some results from ICE'89. *Quart. J. Roy. Meteor. Soc*., **120**, 809-848.

Frederiksen, J.S., and A.G. Davies, 1997: Eddy viscosity and stochastic backscatter paramterizations on the sphere for atmospheric models. *J. Atmos. Sci*., **53**, 887-904.

Frederiksen, J.S., M.R. Dix and A.G. Davies, 2000: A new eddy diffusion parameterization for the CSIRO GCM. CSIRO Atmospheric Research Technical Paper No. 44, 31 pp.

Garratt, J.R., 1993: Sensitivity of climate simulations to land-surface and atmospheric boundary-layer treatments – a review. *J. Climate*, **6**, 419-449.

Garratt, J.R., P.B. Krummel and E.A. Kowalczyk, 1993: The surface energy balance at local and regional scales: a comparison of general circulation model results with observations. *J. Climate*, **6**, 1090-1109.

Garratt, J.R., 1994: Incoming shortwave fluxes at the surface: a comparison of GCM results with observations. *J. Climate*, **7**, 72-80.

Garratt, J.R., 1995: Observed screen (air) and GCM surface/screen temperatures: implications for outgoing longwave fluxes at the surface. *J. Climate*, **8**, 1360-1368.

Garratt, J.R., and A.J. Prata, 1996: Downwelling longwave fluxes at continental surfaces: a comparison of observations with GCM simulations and implications for the global land-surface radiation budget. *J. Climate*, **9**, 646-655.

Garratt, J.R., A.J. Prata, L.D. Rotstayn, B.J. McAvaney and S. Cusack, 1998: The surface radiation budget over oceans and continents. *J. Climate*, **11**, 1951-1968.

Garratt, J.R., D.M. O'Brien, M.R. Dix, J.M. Murphy, G.L. Stephens and M. Wild, 1999: Surface radiation fluxes in transient climate simulations. *Global and Planetary Change*, **20**, 33-55.

Garratt, J.R., 2001: Clear-sky longwave irradiance at the earth's surface: evaluation of climate models. *J. Climate*, **14**, 1647-1670.

Geleyn, J-F., 1987: Use of a modified Richardson number for parameterizing the effect of shallow convection. *Short- and Medium-Range Numerical Weather Prediction*, T. Matsuno, Ed., Special Volume of the J. Meteor. Soc. Japan, 141-149.

Gent, P.R., and J.C. McWilliams, 1990: Isopycnal mixing in ocean circulation models. *J. Phys. Oceanogr*., **20**, 150-155.

Gerdes, R., C. Koberle, and J. Willebrand, 1991: The influence of numerical advection schemes on the results of ocean general circulation models. *Climate Dynamics*, **5**, 211-226.

Gleckler, P.J., and 15 co-authors, 1995: Cloud-radiative effects on implied oceanic energy transports as simulated by atmospheric general circulation models. *Geophys. Res. Lett.*, **22**. 791-794.

Gordon, H.B., 1981: A flux formulation of the spectral atmospheric equations suitable for use in long-term climate modeling. *Mon. Wea. Rev.*, **109**, 56-64.

Gordon, H.B., 1983: Synoptic cloud variations in a low resolution spectral atmospheric model. *J. Geophys. Res.*, **88,** 6563-6575.

Gordon, H.B., and B.G. Hunt, 1987: Interannual variability of the simulated hydrology in a climate model - implications for drought. *Climate Dynamics*, **1**, 113-130.

Gordon, H.B., and B.G. Hunt, 1991: Droughts, floods, and sea surface temperature anomalies: a modelling approach. *Int. J. Climatol.*, **11,** 347-365.

Gordon, H.B., and B.G. Hunt, 1994: Climatic variability within an equilibrium greenhouse simulation. *Climate Dynamics*, **9** 195-212.

Gordon, H.B., and S.P. O'Farrell, 1997: Transient climate change in the CSIRO coupled model with dynamic sea-ice. *Mon. Wea. Rev.*, **125**, 875-907.

Gray, D.M., and D.H. Male, 1981: *Handbook of Snow*. Pergamon Press. 559 pp.

Gregory, D., and P.R. Rowntree, 1990: A mass flux convection scheme with representation of cloud ensemble characteristics and stability dependent closure. *Mon. Wea. Rev.*, **118**, 1483-1506.

Griffies, S.M., 1998: The Gent-McWilliams skew flux. *J. Phys. Oceanogr.*, **28**, 831-841.

Griffies, S.M., A. Gnanadesikan, R.C. Pacanowski, V.D. Larichev, J.K. Dukowicz, and R.D. Smith, 1998: Isoneutral diffusion in a z-coordinate ocean model. *J. Phys. Oceanogr.*, **28**, 805-830.

Heymsfield, A.J., 1977: Precipitation development in stratiform ice clouds: A microphysical and dynamical study. *J. Atmos. Sci*., **34**, 367-381.

Hibler, W.D. III, 1979: A dynamic thermodynamic sea-ice model. *J. Phys. Oceanogr*., **9**, 815-846.

Hillel, D., 1982: *Introduction to soil physics*. Academic Press. 364 pp.

Hirst, A.C., and T.J. McDougall, 1996: Deep-water properties and surface buoyancy flux as simulated by a z-coordinate model including eddy-induced advection. *J. Phys. Oceanogr*., **26**, 1320-1343.

Hirst, A.C., H.B. Gordon and S.P. O'Farrell, 1996: Global warming in a coupled climate model including oceanic eddy-induced advection. *Geophys. Res. Lett*., **23**, 3361-3364.

Hirst, A.C., and T.J. McDougall, 1998: The meridional overturning and dianeutral transport in a z-coordinate ocean model including eddy-induced advection. *J. Phys. Oceanogr*., **28**, 1205-1223.

Hirst, A.C., 1999: The Southern Ocean response to global warming in the CSIRO coupled ocean-atmosphere model. *Environmental Modelling and Software*, **14**, 227-241.

Hirst, A.C., S.P. O'Farrell and H.B. Gordon, 2000: Comparison of a coupled ocean-atmosphere model with and without oceanic eddy-induced advection. Part I: Ocean spinup and control integrations. *J. Climate*, **13**, 139-163.

Holzer, M., 1996: Optimal spectral topography and its effects on model climate. *J. Climate*, **9**, 2442-2463.

Hoskins, B.J., 1980: Representation of the earth topography using spherical harmonics. *Mon. Wea. Rev*., **108**, 111-115.

Hughes, R.L. and S.P. O'Farrell, 1999: Spatially growing Rossby Lee waves: Implications for a coupled atmosphere-ocean GCM. *J. Geophys. Res.*,**104** (C5), 11009-11019.

Hunke, E.C. and J.K. Dukowicz, 1997: An elastic-viscous-plastic model for sea-ice dynamics. *J. Phys. Oceanogr*., **27**, 1849-1867.

Hunt, B.G., and H.B. Gordon, 1988: The problem of "naturally" occurring drought. *Climate Dynamics*, **3**, 19-33.

Hunt, B.G., and H.B. Gordon, 1989: Diurnally varying regional climatic simulations. *Int. J. Climatol*., **9**, 331-356.

Hunt, B.G., and H.B. Gordon, 1991: Simulations of the 1988 US drought. *Int. J. Climatol*., **11**, 629-644.

Hunt, B.G., S.E. Zebiak and M.A. Cane, 1994: Experimental predictions of climatic variability for lead times of twelve months. *Intl. J. Climatol*., **14**, 507-526.

Hunt, B.G., H.B. Gordon and H.L. Davies, 1995: Impact of the greenhouse effect on sea-ice characteristics and snow accumulation in the polar regions. *Intl. J. Climatol*., **15,** 3-23.

Hunt, B.G., 1997: Prospects and problems for multi-seasonal predictions: some issues arising from a study of 1992. *Intl. J. Climatol*., **17**, 137-154

Hunt, B.G., and H.L. Davies, 1997: Mechanisms of multi-decadal climatic variability in a global climate model. *Intl. J. Climatol*., **17**, 565-580.

Hunt, B.G., 1998: Natural climatic variability as an explanation for historical climatic fluctuations. *Climatic Change*, **38**, 133-157.

Hunt, B.G., 2000a: Natural climatic variability and Sahelian rainfall trends. *Global and Planetary Change*, **24**, 107-131.

Hunt, B.G., 2000b: Multiseasonal hindcasts for 1972-92. *Mon. Wea. Rev*., **128**, 1474-1489.

Hunt, B.G., 2001: A description of persistent climatic anomalies in a 1000-year climatic model simulation. *Climate Dynamics*, **17**, 717-733.

Hunt, B.G., and T.I. Elliott, 2002: Mexican megadrought. Accepted by *Climate Dynamics*.

IPCC, 1990: Climate Change: The IPCC Scientific Assessment. J.T. Houghton, G.J. Jenkins, J.J. Ephraums, Eds., Cambridge University Press, 365 pp.

IPCC, 1995: Climate Change 1995: The Science of Climate Change. T. Houghton, L.G. Meira Filho, B.A. Callandar, N. Harris, A. Kattenberg and K. Maskell, Eds., Cambridge University Press, 572 pp.

IPCC SPM, 2001: Climate Change – The Scientific Basic. Summary for Policymakers and Technical Summary of the IPCC WGI Third Assessment Report. Watson, R., Houghton, J and Yihui, D. (eds.) WMO/UNEP. Cambridge University Press, 98 pp.

Jackett, D.R., T.J. McDougall, M.H. England and A.C. Hirst, 2000: Thermal expansion in ocean and coupled general circulation models. *J. Climate*, **13**, 1384-1405.

Jerlov, N.G., 1976: Marine Optics, Chapter 10, Elsevier Oceanography Series, **14**, 127-150.

Johansen, O., 1975: Thermal conductivity of soils. Ph. D. thesis. University of Trondheim, 236 pp.

Kidson, J.W., and I.G. Watterson, 1995: A synoptic climatological evaluation of the changes in the CSIRO nine-level model with doubled CO_2 in the New Zealand region. *Int. J. Climatol*., **15**, 1179-1194.

Kidson, J.W., and I.G. Watterson, 1999: The structure and predictability of the 'high-latitude mode' in the CSIRO9 general circulation model. *J. Atmos. Sci*., **56**, 3859-3873.

Kojima, K., 1967: Densification of seasonal snow cover. *In Physics of ice and snow. Proc. Int. Conf. Low. Temp. Sci*., vol. 1, part 2, 929-952.

Kowalczyk, E.A., J.R. Garratt and P.B. Krummel, 1991: A soil-canopy scheme for use in a numerical model of the atmosphere – 1D stand alone model. CSIRO Division of Atmospheric Research technical paper No. 23. 56 pp.

Kowalczyk, E.A., J.R. Garratt and P.B. Krummel, 1994: Implementation of a soil-canopy scheme into the CSIRO GCM – regional aspects of the model response. CSIRO Division of Atmospheric Research technical paper No. 32. 59 pp.

Kreyscher, M., M. Harder, P. Lemke and G. M. Flato, 2000: Results of the Sea-ice Model Intercomparison Project: Evaluation of sea-ice rheology for use in climate simulations. *J. Geophys. Res*., **105**(C5), 11299-11320.

Kuo, H.L., 1974: Further studies of the parameterization of the influence of cumulus convection on the large-scale flow. *J. Atmos. Sci*., **31**, 1232-1240.

Lacis, A.A., and J.E. Hansen, 1974: A parameterization for the absorption of solar radiation in the earth's atmosphere. *J. Atmos. Sci*., **31**, 118-133.

Lambert, S.J., and G.J. Boer, 2001: CMIP1 evaluation and intercomparison of coupled climate models. *Climate Dynamics*, **17**, 83-106.

Ledley, T.S., 1985: Sea-ice: multi-year cycles and white ice. *J. Geophs. Res*., **90**, 5676-5686.

Ledwell, J.R., A.J. Watson, and C.B. Law, 1999: Mixing of a tracer in the pycnocline. *J. Geophys. Res.*, **103**, 21499 – 21519.

Leonard, B.P., 1979: A stable and accurate convective modelling procedure based on quadratic upstream interpolation. *Computer Methods in Applied Mechanics and Engineering*, **19**, 59-98.

Liu, W.T., K.B. Katsaros and J.A. Businger, 1979: Bulk parameterization of air-sea exchanges of heat and water vapor including the molecular constraints at the interface. *J. Atmos. Sci*., **36**, 1722-1735.

Loth, B., H.F. Graf and J.M. Oberhuber, 1993: Snow cover model for global climate simulations. *J. Geophys. Res*., **98**, 10451-10464.

Louis, J-F., 1979: A parametric model of vertical eddy fluxes in the atmosphere. *Bound.-Layer Meteor*., **17**, 187-202.

Marshall, T.J., J.W. Holmes and C.W. Rose, 1979: *Soil Physics*. Cambridge University Press, 453 pp.

Martin, G.M., D.W. Johnson, and A. Spice, 1994: The measurement and parameterization of effective radius of droplets in warm stratocumulus clouds. *J. Atmos. Sci*., **51**, 1823-1842.

Matear, R.J., and A.C. Hirst, 1999: Climate change feedback on the future oceanic CO_2 uptake. *Tellus*, **51B**, 722-733.

Matear R., Hirst A.C. and McNeil B.I., 2000: Changes in dissolved oxygen in the Southern Ocean with climate change. *Geochem. Geophys. Geosys*t., **1**, Paper number 20000GC000086.

Maykut, G.A., 1986: The surface heat and mass balance. In *Geophysics of Sea Ice*, Ed. N. Untersteiner, NATO ASI Series Vol. **146**, 395-464.

McFarlane, N.A, 1987: The effect of orographically excited gravity wave drag on the general circulation of the lower stratosphere and troposphere. *J. Atmos. Sci*., **44**, 1775-1800.

McGregor, J.L., 1993: Economical determination of departure points for semi-Lagrangian models. *Mon. Wea. Rev*., **121**, 221-230.

McGregor, J.L., H.B. Gordon, I.G. Watterson, M.R. Dix and L.D. Rotstayn, 1993: The CSIRO 9-level atmospheric general circulation model. CSIRO Division of Atmospheric Research technical paper No. 26. 89 pp.

Mechoso, C.R., A.W. Roberston, N. Barth, M.K. Davey, P. Delecluse, P.R. Gent, S. Ineson, B. Kirtman, M. Latif, H. LeTreut, T. Nagal, J.D. Neelin, S.G.H. Philander, J. Polcher, P.S. Schopf, T. Stockdale, M.J. Suarez, L. Terray, O. Thual, and J.J. Tribbia, 1995: The seasonal cycle over the tropical Pacific in coupled ocean-atmosphere general circulation models. *Mon. Wea. Rev.*, **123**, 2825-2838.

Meehl, G.A., P. Gent, J.M. Arblaster, B.L. Otto-Bliesner, E. Brady, and A. Craig, 2001: Factors that affect the amplitude of El Niño in global coupled climate models. *Climate Dyn.*, **17**, 515–526.

Mitchell, J.F.B., R.A. Davis, W.J. Ingram and C.A. Senior, 1995: On surface temperature, greenhouse gases, and aerosols: models and observations. *J. Climate*, **8,** 2364-2386

Moore, A.M., and H.B. Gordon, 1994: An investigation of climate drift in a coupled atmosphere-ocean-sea ice model. *Climate Dynamics*, **10**, 81-95.

Nakicenvic, N. and N Nakicenovic (editors), 2001: Special Report on Emissions Scenarios, Intergovernmental Panel on Climate Change, 98 pp.

NOAA, 1988: Digital relief of the surface of the Earth. Data Announcement 88-MGG-02, NOAA, National Geophysical Data Center, Boulder, Colorado, U.S.A.

Noilhan, J. and S. Planton, 1989: A simple parameterization of land surface processes for meteorological model. *Mon. Wea. Rev.*, **117**, 536-549.

O'Farrell, S.P., J.L. McGregor, L.D. Rotstayn, W.F. Budd, C. Zweck and R. Warner, 1997: Impact of transient increases in atmospheric CO_2 on the accumulation and mass balance of the Antarctic ice sheet. *Annals Glaciol.*, **25**, 137-144.

O'Farrell, S.P., 1998: Investigation of the dynamic sea-ice component of a coupled atmosphere sea-ice general circulation model. *J. Geophys. Res.*, **103** (C8), 15751-15782.

O'Farrell, S.P., and W.M. Connolley, 1998: Comparison of warming trends predicted over the next century around Antarctica from two coupled models. *Annals of Glaciology*, **27**, 576-582.

Pacanowski, R.C., and S.G.H. Philander, 1981: Parameterization of vertical mixing in numerical models of tropical oceans. *J. Phys. Oceanogr.*, **11**, 1443-1451.

Pacanowski, R.C. (ed.), 1996: MOM 2 Version 2, Documentation, User's Guide and Reference Manual. GFDL Ocean Technical Report #3.2, Geophysical Fluid Dynamics Laboratory/NOAA, Princeton, N.J. 08542.

Palmer, T.N., G.J. Shutts and R. Swinbank, 1986: Alleviation of a systematic westerly bias in general circulation and numerical weather prediction models through an orographic gravity wave drag parameterization. *Quart. J. Roy. Meteor. Soc.*, **112**, 1001-1040.

Parker,D.E., C.K. Folland, A. Bevan, M.N. Ward, M. Jackson and K. Maskell, 1995: Marine Surface Data for Analysis of Climatic Fluctuations of Interannual to Century Timescales. In "*Natural Climate Variability on Decade-to-Century Timescales*", D.G. Martinson, K.Bryan, M.Ghil, M.M. Hall, T.R.Karl, E.S.Sarachik, S.Sorooshian and L.D. Talley (eds.). National Academy press, Washington, D.C.

Parkinson, C.L., and W.M. Washington, 1979: A large scale numerical model of sea-ice. *J. Geophys. Res*., **84**, 311-337.

Paulson C.A., and J.J. Simpson, 1977: Irradiance measurements in the upper ocean. *J. Phys. Oceanogr.*, **7**, 952-956.

Penner, J.E., C.A. Atherton, and T.E. Graedel, 1994: Global emissions and models of photochemically active compounds. Global Atmospheric-Biospheric Chemistry, R. Prinn, Ed., Plenum Publishing, New York, 223-248.

Peters-Lidard, C.D., E. Blackburn, X. Liang and E.F. Wood, 1998, The effect of soil thermal conductivity parameterization on surface energy fluxes and temperatures. *J. Atmos. Sci*., **55**, 1209-1224.

Peters H., M.C. Gregg, and J.M. Toole, 1988: On the parameterization of equatorial turbulence. *J. Geophys. Res*., **93**, 1199-1218.

Pitman, A.J., and 41 co-authors, 1993: Project for Intercomparison of Land-surface Parameterization Schemes (PILPS): results from off-line control simulations (Phase 1a). (IGPO Publication Series; 7) GEWEX. 47 pp.

Pontaud, M., J.-P. Céron, M. Kimoto, F. Pluviaud, L. Terray, and A. Vintzileos, 2000. CoPIVEP: a theory-based analysis of coupled processes and interannual variability in the Eqatorial Pacific in four coupled GCMs. *Climate Dynamics*, **16**, 917-933.

Price J.F., R.A. Weller, and R. Pinkel, 1986: Diurnal cycling: observations and models of the upper ocean response to diurnal heating, cooling, and wind mixing. *J. Geophys. Res.*, **91**, 8411-8427.

Rahmstorf, S., 1993: A fast and complete convection scheme for ocean models. *Ocean Modelling*, **101**, 9-11.

Ramaswamy, V., and S.M. Freidenreich, 1992: A study of broadband parameterizations of the solar radiative interactions with water vapor and water drops. *J. Geophys. Res*., 97**,** 11487-11512.

Rautenbach, C.J. de W., 1999: Introduction of a hybrid vertical co-ordinate to an Atmospheric General Circulation Model. Ph. D. Thesis, Faculty of Science, University of Pretoria, South Africa. 142 pp.

Robert, A.J., 1966: The integration of a low order spectral form of the primitive meteorological equations. *J. Meteor. Soc. Japan*, **44**, 237-244.

Rothrock, D.A., 1975: The steady drift of an incompressible Arctic ice cover. *J. Geophys. Res*., **80**, 387-397.

Rotstayn, L.D., and M.R. Dix, 1992: Parallelization of a spectral general circulation model. *Supercomputer* 47, **IX-1**, 33-42.

Rotstayn, L.D., 1997: A physically based scheme for the treatment of stratiform clouds and precipitation in large-scale models. I: Description and evaluation of the microphysical processes. *Quart. J. Roy. Meteor. Soc*., **123**, 1227-1282.

Rotstayn, L.D., 1998: A physically based scheme for the treatment of stratiform clouds and precipitation in large-scale models. II: Comparison of modelled and observed climatological fields. *Quart. J. Roy. Meteor. Soc*., **124**, 389-415.

Rotstayn, L.D., 2000: On the "tuning" of autoconversion parameterizations in climate models. *J. Geophys. Res*., **105**, 15,495-15,507.

Rotstayn, L.D., B.F. Ryan, and J.J. Katzfey, 2000: A scheme for calculation of the liquid fraction in mixed-phase stratiform clouds in large-scale models. *Mon. Wea. Rev*., **128**, 1070-1088.

Sasamori, T., J. London and D.V. Hoyt, 1972: Radiation budget of the southern hemisphere. *Meteor. Monog*., **13**, No. 35, 9-23.

Sausen, R., K. Barthel and K. Hasselmann, 1988: Coupled ocean-atmosphere models with flux correction. *Climate Dynamics*, **2**, 145-163.

Schneider, N., and P. Müller, 1994: Sensitivity of the surface equatorial ocean to the parameterization of vertical mixing. *J. Phys. Oceanogr*., **24**, 1623–1640.

Schneider, N., T. Barnett, M. Latif, and T. Stockdale, 1996: Warm pool physics in a coupled GCM. *J. Climate*, **9**, 219–239.

Schwarzkopf, M.D., and S.B. Fels, 1985: Improvements to the algorithm for computing CO_2 transmissivities and cooling rates. *J. Geophys. Res*., **90**, 10541-10550.

Schwarzkopf, M.D., and S.B. Fels, 1991: The simplified exchange method revisited: An accurate, rapid method for computation of infrared cooling rates and fluxes. *J. Geophys. Res*., **96**, 9075-9096.

Semtner, A. J.. Jr, 1976: A model for the thermodynamic growth of sea-ice in numerical investigations of climate. *J. Phys. Oceanogr*., **6**, 379-389.

Semtner, A. J. Jr., 1987: A numerical study of sea-ice and ocean circulation in the Arctic. *J. Phys. Oceanogr*., **17**, 1077-1099.

Simmonds, I.H., and W.F. Budd, 1990: A simple parameterization of ice leads and the sensitivity of climate to a change in ice concentration. *Annals Glaciol*. **14**, 266-269.

Simmons, A.J., and J. Chen, 1990. The calculation of geopotential and the pressure gradient in the ECMWF atmospheric model: Influence on the simulation of the polar atmosphere and on the temperature analyses. ECMWF Technical Report No 66.

Simonot, J.-Y., and H.L. Treut, 1986: A climatological field of mean optical properties of the world ocean. *J. Geophys. Res. (Oc.)*, **91**, 6642--6646.

Sinclair, M.R., and I.G. Watterson, 1999: Objective assessment of extratropical weather systems in simulated climates. *J. Climate*, **12**, 3467-3485.

Slingo, A., 1989: A GCM parameterization for the shortwave radiative properties of water clouds. *J. Atmos. Sci*., **46**, 1419-1427.

Slingo, J.M., and 21 co-authors, 1996: Intra-seasonal oscillations in 15 atmospheric general circulation models: results from an AMIP diagnostic subproject. *Climate Dynamics*, **12**, 325-357.

Smith, I.N., and H.B. Gordon, 1992: General circulation model simulations of precipitation and atmospheric circulation changes associated with equatorial Pacific warm sea surface temperature anomalies - results from an ensemble of long term integrations. *Climate Dynamics*, **7**, 141-154.

Smith, I.N., 1994: A GCM simulation of global climatic trends: 1950-1988. *J. Climate*, **7**, 732-744.

Smith, I.N., 1995: A GCM simulation of global climate interannual variability: 1950-1988. *J. Climate*, **8**, 709-718.

Smith, I.N., M.R. Dix and R.J. Allan, 1997: The effect of greenhouse SSTs on ENSO simulations with an AGCM. *J. Climate*, **10**, 342-352

Smith, I.N., W.F. Budd and P. Reid, 1998: Model estimates of Antarctic accumulation rates and their relationship to temperature changes. *Annals Glaciol.*, **27**, 246-250.

Smith, I.N., 1999: Estimating mass balance components of the Greenland ice sheet from a long-term GCM simulation. *Global and Planetary Change*, **20**, 19-32.

Smith, R.N.B., 1990: A scheme for predicting layer clouds and their water content in a general circulation model. *Quart. J. Roy. Meteor. Soc*., **116**, 435-460.

Stockdale, T.N., D. Anderson, M. Davey, P. Delecluse, A. Kattenberg, Y. Kitamura, M. Latif, and T. Yamagata, 1993: Intercomparison of tropical ocean GCMs. TOGA Numerical Experimentation Group WCRP-80, 98 pp, WMO.

Sun, Z., and K.P. Shine, 1994: Studies of the radiative properties of ice and mixed-phase clouds. *Quart. J. Roy. Meteor. Soc*., **120**, 111-138.

Suppiah, R., 1994: Synoptic aspects of wet and dry conditions in central Australia: observations and GCM simulations for 1x CO_2 and 2x CO_2 conditions. *Climate Dynamics*, **10**, 395-405.

Suppiah, R., 1995: The Australian summer monsoon: CSIRO9 GCM simulations for 1x CO_2 and 2x CO_2 conditions. *Global and Planetary Change*, **11**, 95-109.

Syktus, J.I., and H.B. Gordon, 1994: Sensitivity of a coupled atmosphere-dynamic upper ocean GCM to variations of CO_2, solar constant, and orbital forcing. *Geophys. Res. Lett*., **21**, 1599-1602

Syu, H.-H., J.D. Neelin, and D. Gutzler, 1995: Seasonal and interannual variability in a hybrid coupled GCM. *J. Climate*, **8**, 2121–2143.

Tiedtke, M., 1987: Parameterization of cumulus convection in large-scale models. *Physically-Based Modelling and Simulation of Climate and Climatic Change, Part I*, M.E. Schlesinger, Ed., NATO ASI Series, Kluwer Academic, pp. 375-431.

Troup, A.J., 1965: 'The Southern Oscillation.' *Quart. J. Roy. Meteor. Soc*., **91**, 490-506.

Vimont, D.J., D.S. Battisti and A.C. Hirst, 2001: Footprinting: A seasonal connection between the tropics and mid-latitudes. *Geophys. Res. Lett.*, **28**, 3923-3926.

Vimont, D.J., D.S. Battisti and A.C. Hirst, 2002: Pacific interannual and interdecadal equatorial variability in a 1000-year simulation of the CSIRO coupled general circulation model. *J. Climate*, **15**, 160-178.

Wadhams, P., 1991: The seasonal sea-ice zone. In *Geophysics of Sea Ice*, Ed. N. Untersteiner, NATO ASI Series, Vol **146**, 825-992.

Walland, D.J., S.B. Power and A.C. Hirst, 2000: Decadal climate variability simulated in a coupled general circulation model. *Climate Dynamics*, **16,** 201-211.

Walsh, J.E., 1991: The Arctic as bellweather. *Nature*, **352**, 19.

Wang, W.-C., X.-Z. Liang, M.P. Dudek, D. Pollard and S.L. Thompson, 1995: Atmospheric ozone as a climate gas. *Atmos. Res*., **37**, 247-256.

Watterson, I.G., M.R. Dix, H.B. Gordon and J.L. McGregor, 1995: The CSIRO nine-level atmospheric general circulation model and its equilibrium present and doubled CO_2 climates. *Australian Meteorological Magazine*, **44**, 111-125.

Watterson, I.G., and M.R. Dix, 1996: Influences on surface energy fluxes in simulated present and doubled CO_2 climates. *Climate Dynamics*, **12**, 359-370.

Watterson, I.G., 1997: The diurnal cycle of surface air temperature in simulated present and doubled CO_2 climates. *Climate Dynamics*, **13**, 533-545.

Watterson, I.G., S.P. O'Farrell and M.R. Dix, 1997: Energy and water transport in climates simulated by a general circulation model that includes dynamic sea-ice. *J. Geophys. Res*., **102** (D10), 11027-11037.

Watterson, I.G., 1998: An analysis of the global water cycle of present and doubled CO_2 climates simulated by the CSIRO General Circulation Model. *J. Geophys. Res*., **103** (D18), 23113-23129.

Watterson, I.G., M.R. Dix and R.A. Colman, 1999: A comparison of present and doubled CO_2 climates and feedbacks simulated by three general circulation models. *J. Geophys. Res*., **104** (D2), 1943-1956.

Watterson, I.G., 2000: Southern midlatitude zonal wind vacillation and its interaction with the ocean in GCM simulations. *J. Climate*, **13**, 562-578.

Whetton, P.H., P.J. Rayner, A.B. Pittock and M.R. Haylock, 1994: An assessment of possible climate change in the Australian region based on an intercomparison of general circulation modelling results. *J. Climate*, 7, 441-463.

Whetton, P.H., M.H. England, S.P. O'Farrell, I.G. Watterson and A.B. Pittock, 1996: Global comparison of the regional rainfall results of enhanced greenhouse coupled and mixed layer ocean experiments: implications for climate change scenario development. *Climatic Change*, **33**, 497-519.

Williams, P.J., and M.W. Smith, 1989: *The Frozen Earth*. Cambridge University Press, 306 pp.

Wilson, S.G., 2000: How ocean vertical mixing and accumulation of warm surface water influence the "sharpness" of the equatorial thermocline. *J. Climate*, **13**, 3638-3656.

Wilson, S.G., 2002: Evaluation of various vertical mixing parameterizations in a tropical Pacific Ocean GCM. *Ocean Modelling*, **4**, 291-311.

Wu, X. Q., W.D. Hall, W.W. Grabowski, M.W. Moncrieff, W.D. Collins and J.T. Kiehl, 1999: Long-term behavior of cloud systems in TOGA COARE and their interactions with radiative and surface processes. Part II: Effects of ice microphysics on cloud-radiation interaction. *J. Atmos. Sci*., **56**, 3177-3195.

Xie, P, and P.A. Arkin, 1997: Global precipitation. A 17-year monthly analysis based on gauge observations, satellite estimates and numerical model outputs. *Bull. Amer. Meteor. Soc.*, **78**, 2539-2558.

Yang, Z.L., R.E. Dickinson, A. Robock and K.Y. Vinnikov, 1997: On validation of the snow sub-model of the Biosphere-Atmosphere Transfer Scheme with Russian snow cover and meteorological observational data. *J. Climate*, **10**, 353-373.

Yonetani, T., and H.B. Gordon, 2001a: Abrupt changes as indicators of decadal climate variability. *Climate Dynamics*, **17**, 249-258

Yonetani, T., and H.B. Gordon, 2001b: Simulated changes in the frequency of extremes and regional features of seasonal/annual temperature and precipitation when atmospheric CO_2 is doubled. *J. Climate*, **14**, 1765-1779.

Yu, Z., and P. Schopf, 1997: Vertical eddy mixing in the tropical ocean: Its influence on zonal currents. *J. Phys. Oceanogr*., **27**, 1447–1458.

Zeng, X., M. Zhao and R.E. Dickinson, 1998: Intercomparison of bulk aerodynamic algorithms for the computation of sea surface fluxes using TOGA COARE and TAO data. *J. Climate*, **11**, 2628-2644.

Zhang, Y., and 10 co-authors, 1997: East Asian winter monsoon: results for eight AMIP models. *Climate Dynamics*, **13**, 797-820.

Zobler, L., 1988: A world soil file for global climate modeling. NASA Tech. Memo. 87802. [Available from NASA Goddard Institute for Space Studies, 2880Broadway, New York, NY 10025.]

26 Appendix A

List of symbols and abbreviations used in the text

Due to the complexity of the climate system model, the list of symbols is divided into four sections. Section (a) deals with the atmospheric model; section (b) deals with the land surface component; section (c) deals with the sea-ice model; and section (d) deals with the ocean and coupled model component. There are initial references to the parts of the text covered by the symbols listed in each section. The abbreviations used in the text are detailed in section (e).

(a) Symbols for the atmospheric model (Sections 4-8, 10-18 and Appendix B):

(In the text below, some variables will have a superscript ^ which indicates a weighting that depends upon by surface pressure. The subscript $_s$ will often be used to denote a surface value.)

a	radius of the earth
$A_k, A(\eta)$	level coefficient for determining p_k
$B_k, B(\eta)$	level coefficient for determining p_k
B_p	pressure term for dynamical equations $= \mu B / p$
C	cloud fraction
C_{DN}, C_{HN}	neutral transfer coefficients for momentum and heat
C_p	specific heat capacity of dry air
$\hat{D}$	divergence
$\hat{E}$	pressure weighted kinetic energy
$\overline{E}$	predefined mean kinetic energy per model level
E_s	surface evaporation flux
f	coriolis parameter
F_m, F_h	Stability function for momentum and heat
F_r	Froude number
$\underline{F}$	friction term for momentum equation
g	acceleration due to gravity
G	heat flux into ground
h_e	gravity wave drag launching height
H_s	upward sensible heat flux
J	cube root of moisture $= q^{1/3}$
k	model level; von Karman constant (0.4)
K_m, K_h	vertical mixing coefficients for momentum and heat
K_H	horizontal diffusion coefficient
L_C, L_F	latent heat of condensation and fusion
l	total (zonal + meridional) wavenumber
l_m	mixing length
m	meridional wavenumber

M_p	convective mass flux
MW	total meridional wave number at model spectral resolution
N	Brunt-Vaisala frequency
NL	number of atmospheric model levels
p	pressure
p_s	surface pressure
P_{00}	constant pressure = 1000 hPa
P_l^m	associated Legendre polynomial of order m and degree l
P_{sr}	predefined surface pressure field governed by surface height
q	moisture variable
q_C	cloud water plus cloud ice = $q_L + q_I$
q_I	cloud ice
q_L	cloud liquid water
q_V	moisture vapour
q_W	total water content $= q_V + q_L + q_I$
Q	atmospheric heating
R	specific gas constant for dry air
$R_s^{\downarrow}$	downward longwave radiation at surface
Ri_b	bulk Richardson number
S	dry static energy; vertically integrated sulfate mass
$S_s^{\downarrow}$	downward solar radiation at surface
T	temperature
T_{00}	constant temperature = 288 K
T_0	constant temperature $= 0.6652\, T_{00}$
T_1	constant temperature $= T_{00} - T_0$
$\tilde{T}$	hybrid vertical coordinate temperature variable $= T - T_0 - T_1\{p / P_{00}\}^K$
$\overline{T}$	predefined constant temperature (290 K)
T'	atmospheric temperature variable $= (T - \overline{T})$
T_L	liquid-frozen water temperature
T_s	surface temperature
T_v	virtual temperature
U, u	zonal velocity
u_*	scaling velocity
Y	projection of atmospheric velocity on surface velocity
V, v	meridional velocity
V_I	fall speed for ice crystals
z	height
z_0, z_T	roughness lengths for momentum and heat
α_s	surface albedo
$\tilde{\beta}_T, \tilde{\beta}_Q$	cloud buoyancy parameter

$\hat{\chi}$	velocity potential
δ_1	surface pressure gradient term $= \underline{k}.(\underline{V} x \underline{\nabla}) p_s$
δ_2	surface pressure gradient term $= \underline{V}.\underline{\nabla} p_s$
ε	ratio of molecular weight of water to dry air.
ε_s	emissivity of the surface
ϕ	geopotential height (= gz) or latitude
η	hybrid (σ : p) vertical coordinate
η_c	gravity wave drag critical level
$\dot{\eta}$	"vertical" velocity in hybrid coordinate system
κ	R / C_p
λ_l	asymptotic mixing length
λ_r	gravity wave drag parameter
μ	vertical pressure weighting $= \partial p / \partial \eta$
θ	potential temperature
θ_V	virtual potential temperature
θ_L	potential temperature for temperature T_L
ρ	density of air
σ	p / p_s or Stefan-Boltzmann coefficient
τ	timestep number
$\underline{\tau}_s$	surface stress
ω	vertical (pressure) velocity (= dp / dt); angular velocity
$\hat{\omega}$	pressure weighted “vertical” velocity in η or σ coordinate system
$\hat{\xi}$	vorticity
$\hat{\psi}$	stream function
Δt	timestep

(b) Symbols for the land surface (vegetation canopy) model (Section 9):

b	non-dimensional constant
c_s	specific heat (c_{soil}, c_{ice} are soil and ice values)
c_{sn}	heat capacity of snow
E_s	surface evaporation flux
E_{sn}	rate of sublimation
F	soil water flux
$Fage$	transformed snow age
F_{bg}	fraction of bare ground covered by snow
g	acceleration due to gravity
G	net heat flux at the surface
H_s	surface sensible heat flux
k_{dry}	dry conductivity
k_s	thermal conductivity

k_{sat}	saturated conductivity
k_{sn}	thermal conductivity of snow
K	hydraulic conductivity (K_s = value at saturation)
K_r	Kersten number
L_f	latent heat of fusion
P_{rain}	rainfall rate
P_{sn}	snowfall rate
r_i	runoff, drainage and root extraction for evapotranspiration
$R_s^{\downarrow}$	downward longwave radiation at surface
R_{rain}	heat flux associated with rain
$S_s^{\downarrow}$	downward solar radiation at surface
S_d	snow depth
S_{melt}	snowmelt
S_{sn}	total snow mass
$SNage$	prognostic snow age
T_f	canopy temperature
T_{frz}	freezing temperature
T_s	surface temperature
T_{sn}	snow temperature
z	soil depth
zo_{bg}	bare ground roughness length
α_s	surface albedo
α_{veg} , α_{bg} , α_{sn}	albedo of vegetation, bare ground and snow
σ_{veg}	snow-free vegetation cover fraction
ε_s	emissivity of the ground
ε_{sn}	emissivity of snow
η_{fc}	field capacity
η_i	frozen soil moisture
η_l	liquid soil moisture
η_{lf}	fractional liquid content
η_{sat}	saturation content
η_{sm}	soil moisture $= \eta_l + \eta_i$
η_w	wilting content
η_{Asat}	actual saturation
π_c	viscosity coefficient for snow
π_T	viscosity of snow
ρ_s	density (ρ_{soil} , ρ_{ice} are soil and ice values)

ρ_{sn}	snow density
σ	Stefan-Boltzmann constant
τ	timestep number
ψ	matrix potential (ψ_s = value at saturation)
ξ_a	zenith angle

(c) Symbols for the sea-ice model (Section 19):

c_w	ocean heat capacity
C	ice concentration
C_w	drag coefficient
dz	thickness of upper ocean layer
E_s	surface latent heat flux
f	Coriolis parameter
$\underline{F}$	internal ice stress term
F_i	oceanic heat flux term
h	ice thickness
H_s	surface sensible heat flux
k_{frz}	heat transfer coefficient
$P_{\max}$	ice strength
$R_s^{\downarrow}$	downward longwave radiation at surface
$S_s^{\downarrow}$	downward solar radiation at surface
T_s	ice surface temperature or temperature of leads
u, v	ice velocity components
$\underline{V}_i$	ice velocity
α_s	surface albedo (snow or ice)
γ_i	ice heat capacity
γ_0	heat capacity of leads water column
λ_C	SST relaxation time constant
θ	turning angle
ρ_w	ocean density
$\underline{\tau}_a$	atmospheric surface stress
$\underline{\tau}_w$	ocean stress
Ω	angular velocity of the earth
$\underline{\nabla} H$	sea surface slope term

(d) Symbols for the ocean model and coupled model (Sections 20 and 21)

A_I	isoneutral tracer diffusivity
A_m	horizontal viscosity
A_V	vertical diffusivity

A_{VT}	tropical vertical diffusivity
dz_1	depth of the first ocean level
E_s	surface evaporation flux
g	acceleration due to gravity
G	heat flux into the ocean
H_s	surface sensible heat flux
K_m, K_h	vertical mixing coefficients for momentum and heat
$P-E$	precipitation less evaporation
Ri_b	bulk Richardson number
Ri_g	gradient Richardson number
R_{off}	land runoff
$R_s^{\downarrow}$	downward longwave radiation at surface
S	ocean salinity
S_{ICE}	mean sea-ice salinity (10 ppt)
S_{OC}	mean ocean salinity at surface (35 ppt)
$S_s^{\downarrow}$	downward solar radiation at surface
T	ocean temperature
T_{OC}	surface ocean temperature
T_z	first derivative of temperature with respect to depth
U, V	ocean zonal and meridional velocity components, respectively
U_z, V_z	first derivatives of U and V with respect to depth
z	ocean depth
α	coefficient of thermal expansion of water
α_s	surface albedo
δ_{FW}	freshwater flux into the oceans
δ_{IS}	depth change due to ice formation
δ_{SB}	depth change due to sublimation from bare ice
ε_s	emissivity of the surface
κ	isopycnal thickness diffusivity
μ	background minimum default vertical viscosity
ρ_0	reference density
σ	Stefan-Boltzmann constant
Δt	model timestep
$\Delta\sigma_\theta$	potential density difference between surface and depth z
ΔU	zonal velocity difference " " " "
ΔV	meridional velocity difference " " " "

(e) List of abbreviations

AGCM	atmospheric general circulation model
AMIP	Atmospheric Model Intercomparison Project
BMRC	Bureau of Meteorology Research Centre (Australia)

CCM3	NCAR Community Climate Model 3
CFC	chlorofluorocarbon
CMIP	Coupled Model Intercomparison Project
CO_2	carbon dioxide
CSIRO	Commonwealth Scientific and Industrial Research Organization (Australia)
DJF	December, January, February
ENSO	El Niño-Southern Oscillation
FANGIO	Feedback Analysis for GCM Intercomparison and Observations
FFT	Fast Fourier Transform
GCM	general circulation model
GFDL	Geophysical Fluid Dynamics Laboratory (USA)
GISST	Global Ice and Sea Surface Temperature data set
GM	Gent and McWilliams (1990) ocean eddy mixing scheme
JJA	June, July, August
PCMDI	Program for Climate Model Diagnosis and Intercomparison
IPCC	Intergovernmental Panel on Climate Change
LAM	limited area model
Mk1,2,3	versions 1,2,3 of the CSIRO climate system model
MLO	mixed-layer ocean
MOM	Modular Ocean Model (GFDL)
NADW	North Atlantic deep water
NCAR	National Center for Atmospheric Research (USA)
NH	Northern Hemisphere
OGCM	ocean general circulation model
O_3	ozone
PBL	planetary boundary layer
R21,R42	spectral atmospheric model truncation at rhomboidal 21,42
SH	Southern Hemisphere
SIMIP	Sea-ice Model Inter-comparison Project
SLT	Semi-Lagrangian Transport
SOI	southern oscillation index
SSS	sea surface salinity
SST	sea surface temperature
T63	Mk3 spectral model truncation at triangular 63 (1.875°EW x 1.875°NS)
T63_2	Mk3 ocean model resolution (1.875°EW x 0.9375°NS)
UKMO	United Kingdom Meteorological Office

27 Appendix B

AGCM dynamical core

The formulation of the dynamical core for the Mk3 spectral model is described in this appendix. Initial details about the spectral model with dynamical equations cast in the flux form can be found in Gordon (1981). The basic definition of variables and terminology used here is the same as in that reference. The model equations were originally formulated in terms of a sigma (σ) vertical coordinate, where $\sigma = p / p_s$. The current (Mk3) atmospheric model is now formulated in terms of a hybrid (σ : p) vertical coordinate. Full details on implementing the hybrid system in the model are contained in Rautenbach (1999). Only brief details about the equations in hybrid form will be given in this appendix.

In the Mk1 model σ-coordinate system, the spectral prognostic variables are the surface pressure (p_s), the surface pressure weighted divergence ($\hat{D} = \underline{\nabla}.(p_s \underline{V}) = \underline{\nabla}.\underline{\hat{V}}$), vorticity ($\hat{\xi} = k.\underline{\nabla} x \underline{\hat{V}}$), and temperature ($\hat{T}$).

27.1 Hybrid vertical coordinate system

In the Mk3 version of the atmospheric model, the hybrid vertical coordinate is defined by η, and the pressure at a model level η is given by

$$p(\eta) = A(\eta)P_{00} + B(\eta)p_s . \qquad 26.1$$

Here $A(\eta)$ and $B(\eta)$ have pre-defined values and $P_{00} = 1000\ hPa$. The method of deriving $A(\eta)$ and $B(\eta)$ is given in full in Rautenbach (1999), and the values are generated in the model code via subroutine *vertc*. In the hybrid system, the Earth's surface still forms the first coordinate surface (identical to the σ-system), while the remaining vertical coordinate surfaces gradually revert with altitude to isobaric levels. In the Mk3 model, the top two model full levels (and three half levels) are constant pressure levels. The hybrid coordinate has η = 1 at the surface and η = 0 at the top of the model atmosphere. The form of $A(\eta)$ is such that it ranges from zero near the surface and tends to η in the upper atmosphere. On the other hand, the form of $B(\eta)$ is such that is equal to 1 at the surface and diminishes with height to become zero for the top two model full levels. (The $A(\eta)$ and $B(\eta)$ for the Mk3 model with 18 vertical levels are given in Table 1 in Section 4).

In the hybrid equations, the p_s weighting of the model variables used in the σ-system is replaced by the quantity μ where

$$\mu = \frac{\partial p}{\partial \eta} = P_{00}\frac{\partial A}{\partial \eta} + p_s \frac{\partial B}{\partial \eta} . \qquad 26.2$$

We then have $\underline{\hat{V}} = \mu \underline{V}$ etc as model "pressure weighted" variables. The above implies that for the implementation of the η-system in the flux form of the equations, we should have $A(\eta)$ and

$B(\eta)$ as pre-defined, smoothly varying functions of η. It can be shown that, for energy conservation in finite difference form in the vertical, we should derive A and B for model "half" levels in the vertical only, and then derive "full" level values by averaging the half level values. The μ values are obtained using $\frac{\partial A}{\partial \eta}$ and $\frac{\partial B}{\partial \eta}$ evaluated by finite differences between half levels.

27.2 Dynamical core equations

In the hybrid system, the momentum equation may be written as

$$\frac{\partial \hat{\underline{V}}}{\partial t} + \hat{D}\underline{V} + \mu\underline{\nabla}E + \left(\hat{\xi} + \frac{\partial B}{\partial \eta}\delta_1 + \mu f\right)\underline{k}x\underline{V} + \frac{\partial \hat{\omega}\underline{V}}{\partial \eta} + \mu\underline{\nabla}(\phi + \phi_s) + \mu\frac{RT}{p}\underline{\nabla}p = \mu\underline{F}\cdot \qquad 26.3$$

Here we have $\underline{\nabla} \equiv \underline{\nabla}_\eta$, and some of the basic quantities used above are: $\hat{\underline{V}} = \mu\underline{V}$; $E = V^2/2$; $\delta_1 = \underline{k}.(\underline{V}x\underline{\nabla})p_s$; and $\hat{\omega} = \mu\dot{\eta}$. (Essentially p_s in the σ form of the equation has been replaced by μ). For convenience, certain terms are now gathered together for later manipulation. These are defined by $\underline{C}$ where

$$\underline{C} = \mu\underline{\nabla}E + \mu\underline{\nabla}(\phi + \phi_s) + \mu\frac{RT}{p}\underline{\nabla}p = \mu\underline{\nabla}E + \mu\,\underline{PG} \qquad 26.4$$

and $\underline{PG}$ is defined as the "pressure gradient" term. The momentum equation is then converted to equations for vorticity $\hat{\xi}$ and divergence $\hat{D}$ for use in the spectral model (see sub-section 26.4 and also Gordon (1981)).

The thermodynamic equation in the model is cast in terms of a temperature deviation from a mean (defined for the moment by T'). The temperature prognostic variable is denoted by $\hat{T} = \mu T'$ and the equation is:

$$\frac{\partial \hat{T}}{\partial t} + \underline{\nabla}.(\mu\underline{V}T') + \frac{\partial \hat{\omega}T'}{\partial \eta} = \frac{\mu\kappa T\omega}{p} + \frac{\mu Q}{C_p}. \qquad 26.5$$

The hydrostatic equation in p-coordinates is given by $\frac{\partial \phi}{\partial p} = -\frac{RT}{p}$ which, in the hybrid system, becomes

$$\frac{\partial \phi}{\partial \eta} = -\frac{RT\mu}{p}. \qquad 26.6$$

The continuity equation in hybrid coordinates is given by:

$$\frac{\partial \mu}{\partial t} + \underline{\nabla}.(\mu\underline{V}) + \frac{\partial(\mu\dot{\eta})}{\partial \eta} = \frac{\partial B}{\partial \eta}\frac{\partial p_s}{\partial t} + \hat{D} + \frac{\partial \hat{\omega}}{\partial \eta} = 0. \qquad 26.7$$

The surface pressure prognostic is obtained by the vertical integral of this equation (using $\hat{\omega} = B = 0$ at $\eta = 0$ and $\hat{\omega} = 0$, $B = 1$ at $\eta = 1$):

$$\frac{\partial p_s}{\partial t} = -\int_0^1 \hat{D}\, d\eta = -[\hat{D}]^1 . \qquad 26.8$$

The vertical "velocity" $\hat{\omega} = \mu\dot{\eta}$ (at a half level) is obtained by vertically integrating the continuity equation between $\eta = 0$ and the requisite half-level η giving:

$$\hat{\omega} = -B\frac{\partial p_s}{\partial t} - \int_0^\eta \hat{D}\, d\eta = B\,[\hat{D}]^1 - [\hat{D}]^\eta . \qquad 26.9$$

In addition, we require $\omega = Dp/Dt$ for the thermodynamic equation:

$$\omega = \frac{Dp}{Dt} = \frac{\partial p}{\partial t} + \underline{V}.\underline{\nabla} p + \dot{\eta}\frac{\partial p}{\partial \eta} = -B[\hat{D}]^1 + B\underline{V}.\underline{\nabla} p_s + \mu\dot{\eta} = B\,\delta_2 - [\hat{D}]^\eta . \qquad 26.10$$

27.2.1 Virtual temperature

The momentum equation and thermodynamic equation above are further modified to include the use of virtual temperature T_V. The virtual temperature is defined by

$$T_v = T(1 + q/\varepsilon)/(1 + q) \qquad 26.11$$

where q is the atmospheric moisture vapour mixing ratio, and $\varepsilon = 0.622$. The inclusion of T_V is accomplished (in an energy conserving manner) by replacing terms such as RT by RT_V, and ϕ by ϕ_V, where ϕ_V is the geopotential height derived by using T_V in the hydrostatic equation. Considering the momentum equation, the pressure gradient term $\underline{PG}$ is defined by

$$\underline{PG} = \underline{\nabla}(\phi + \phi_s) + T\frac{R}{p}\underline{\nabla} p . \qquad 26.12$$

In terms of virtual temperature this is replaced by

$$\underline{PG} = \underline{\nabla}(\phi_V + \phi_s) + T_V\frac{R}{p}\underline{\nabla} p = \underline{\nabla}(\phi + \phi_s + (\phi_V - \phi)) + T_V\frac{R}{p}\underline{\nabla} p . \qquad 26.13$$

This implies that the geopotential term can be reformulated by means of an additional simple "adjustment" term, namely $(\phi_V - \phi)$.

The thermodynamic equation also has to be modified for virtual temperature. This change only affects the term involving ω, and is implemented in a way that ensures conservation of energy. The original ω term can be written as:

$$\frac{\mu\kappa T\omega}{p} = \frac{\mu\kappa T}{p}\left\{B\,\delta_2 - [\hat{D}]^{\eta}\right\} = \kappa T\,\frac{\mu B}{p}\delta_2 + \frac{1}{C_p}\frac{\partial\phi}{\partial\eta}[\hat{D}]^{\eta}\,. \qquad 26.14$$

(Note that casting these terms in this particular form ensures cancellation with terms in the momentum equation when the equation for the global and vertical mean of the total energy of the system, $C_pT + E$, is considered.) In order to use virtual temperature in a consistent way with that used in the momentum equation, we replace the above form by

$$\frac{\mu\kappa T_V\omega}{p} = \kappa T_V\,\frac{\mu B}{p}\delta_2 + \frac{1}{C_p}\frac{\partial\phi_V}{\partial\eta}[\hat{D}]^{\eta}\,. \qquad 26.15$$

27.2.2 Semi-implicit time integration

The equations are integrated using a semi-implicit time integration scheme. Certain components that link the momentum, thermodynamic and surface pressure equations are treated implicitly. Details can be found in Gordon (1981). The geopotential is related to the temperature via the hydrostatic equation. In hybrid coordinates this is given by

$$\frac{\partial\phi}{\partial\ln(\eta)} = -RT\,\frac{\mu\eta}{p} = -RT_N\,. \qquad 26.16$$

With the assumption that T_N varies as $\ln(\eta)$ in the vertical (and $\mu\eta / p \approx 1$), this can be vertically integrated to obtain ϕ at each level. It may then be cast in a (vertical) vector-matrix form (where the under-bar means a vertical vector):

$$\underline{\phi} = \underline{\underline{A}}\,\underline{T}_N\,. \qquad 26.17$$

In order to implement a semi-implicit time integration method, we now define an equivalent for the flux form of the equations (which uses a temperature variable based upon a deviation from a mean):

$$\underline{\hat{\phi}} = \underline{\underline{A}}\,\underline{\hat{T}}\,. \qquad 26.18$$

Here it must be noted that $\hat{\phi}$ is *not* equal to $\mu\phi'$ (although it has a very similar form and magnitude). Thus in order to implement the semi-implicit time integration scheme, the terms $\nabla\hat{\phi}$ and $R\bar{T}\nabla p_s$ are added and subtracted to the components in the equation for $\underline{C}$

$$\underline{C} = \mu\underline{\nabla}E + \mu\underline{\nabla}(\phi + \phi_s) - \underline{\nabla}\hat{\phi} + \mu\frac{RT}{p}\underline{\nabla}p - R\bar{T}\,\underline{\nabla}p_s + \left\{\underline{\nabla}\hat{\phi} + R\bar{T}\,\underline{\nabla}p_s\right\} \qquad 26.19$$

in which the last two terms contained in {..} undergo an implicit treatment. Here $\overline{T}$ is a predefined constant (temperature) with a value of order that of the global mean in the lower atmosphere (290 K).

In the thermodynamic equation, the term needing implicit treatment is the $\hat{D}$ component in the ω term. Thus (following the method used for the σ version of the equation), we add and subtract a linearized $\hat{D}$ dependent term:

$$\frac{\mu\kappa T_V \omega}{p} = \kappa T_V \frac{\mu B}{p}\delta_2 + \frac{1}{C_p}\frac{\partial \phi_V}{\partial \eta}[\hat{D}]^\eta + \frac{\kappa\overline{T}}{\eta}[\hat{D}]^\eta - \frac{\kappa\overline{T}}{\eta}[\hat{D}]^\eta \qquad 26.20$$

$$= \kappa\left\{T_V \frac{\mu B}{p}\delta_2 + [\hat{D}]^\eta\left(\frac{1}{R}\frac{\partial \phi_V}{\partial \eta} + \frac{\overline{T}}{\eta}\right)\right\} - \frac{\kappa\overline{T}}{\eta}[\hat{D}]^\eta . \qquad 26.21$$

In the semi-implicit time integration scheme, the last term is treated implicitly.

27.2.3 Formulation with temperature variable based on T'

The equations are now presented using the model temperature prognostic as used in the original Mk1 model. (Note that the Mk3 model uses a different temperature variable, but it is instructive to consider the Mk1 formulation first. The Mk3 method is described in sub-section 26.3 below). The Mk1 temperature prognostic is given by $\hat{T} = \mu T' = \mu(T - \overline{T})$. For the momentum equation we define the quantity $B_p = \mu B / p$, and the component $\underline{C}$ then becomes (with virtual temperature representation included):

$$\underline{C} = \mu\underline{\nabla}E + \mu\underline{\nabla}(\phi + \phi_s + (\phi_V - \phi)) - \underline{\nabla}\hat{\phi} + RT_V B_p \underline{\nabla}p_s - R\overline{T}\underline{\nabla}p_s + \left\{\underline{\nabla}\hat{\phi} + R\overline{T}\underline{\nabla}p_s\right\} \qquad 26.22$$

Using global means and deviations ($E = \overline{E} + E'$ etc) in some gradient terms gives:

$$\begin{aligned}\underline{C} &= \mu\underline{\nabla}E' + \mu\underline{\nabla}(\phi' + \phi_s' + (\phi_V - \phi)) - \underline{\nabla}\hat{\phi} + R\left[T_V B_p - \overline{T}\right]\underline{\nabla}p_s + \left\{\underline{\nabla}\hat{\phi} + R\overline{T}\underline{\nabla}p_s\right\} \\ &= \underline{\nabla}\left[\mu E' + \mu(\phi' + \phi_s' + (\phi_V - \phi)) - \hat{\phi}\right] - \left[E' + (\phi' + \phi_s') + (\phi_V - \phi)\right]\underline{\nabla}\mu \\ &\quad + R\left[T_V B_p - \overline{T}\right]\underline{\nabla}p_s + \left\{\underline{\nabla}\hat{\phi} + R\overline{T}\underline{\nabla}p_s\right\} \\ &= \underline{\nabla}\hat{E} + \left(R\left[T_V B_p - \overline{T}\right] - \left[E' + (\phi' + \phi_s') + (\phi_V - \phi)\right]\frac{\partial B}{\partial \eta}\right)\underline{\nabla}p_s + \left\{\underline{\nabla}\hat{\phi} + R\overline{T}\underline{\nabla}p_s\right\}\end{aligned} \qquad 26.23$$

where

$$\hat{E} = \mu E' + \mu(\phi' + \phi_s' + (\phi_V - \phi)) - \hat{\phi} . \qquad 26.24$$

27.3 Hybrid spectral equations with the Simmons-Chen temperature variable.

In the Mk1 spectral model formulation (see above), the model prognostic temperature variable was based upon $T' = (T - \overline{T})$ where $\overline{T}$ is an isothermal mean temperature (290 K). In the Mk3 model, the temperature variable has been replaced by one which has a pressure dependency. This pressure dependency can be used to ensure that the cancellation of large terms in the pressure gradient term in the momentum equation is minimized. The new temperature variable is based on that described in Simmons and Chen (1990), and is defined by:

$$\tilde{T} = T - T_0 - T_1\{p / P_{00}\}^{\kappa} \qquad 26.25$$

where $T_0 + T_1 = T_{00} = 288\ K$, and $T_0 = 0.6652\ T_{00}$

The main prognostic temperature variable for the model is now defined by $\hat{T} = \mu\tilde{T}$.

The method will also require modified geopotential terms $\hat{\phi}, \tilde{\phi}$ and $\tilde{\phi}_s$ as shown below.

27.3.1 The thermodynamic equation

The original thermodynamic equation (with virtual temperature) is given by

$$\frac{DT}{Dt} = \frac{\kappa T_v \omega}{p} + \frac{Q}{C_p}. \qquad 26.26$$

Using $\tilde{T}$ this becomes

$$\frac{D\tilde{T}}{Dt} = \frac{\kappa\{\tilde{T} + T_0 + (T_v - T)\}\omega}{p} + \frac{Q}{C_p}. \qquad 26.27$$

Converting to flux form, and defining $\hat{T} = \mu\tilde{T}$ (rather than the original $\mu T'$) we get

$$\frac{\partial \hat{T}}{\partial t} + \underline{\nabla}(\underline{\hat{V}}\tilde{T}) + \frac{\partial \hat{\omega}\tilde{T}}{\partial \eta} = \frac{\mu\kappa\{\tilde{T} + T_0 + (T_v - T)\}\omega}{p} + \frac{\hat{Q}}{C_p}$$

$$= \frac{\mu\kappa T_v \omega}{p} + \kappa\left(\frac{\mu\omega}{p}\right)(\tilde{T} - T + T_0) + \frac{\hat{Q}}{C_p}. \qquad 26.28$$

Note that this has the same form on the RHS when not using the Simmons-Chen temperature variable except for an additional term A_{KWT} where

$$A_{KWT} = \kappa\left(\frac{\mu\omega}{p}\right)(\tilde{T} - T + T_0) \qquad 26.29$$

Following the method outlined above, the gravity wave generator term involving $\hat{D}$ is added and subtracted in exactly the same way for semi-implicit treatment. However, this particular term now uses T_{00} as the global mean temperature instead of $\overline{T}$. Thus the term $(\kappa T_{00}/\eta)[\hat{D}]^{\eta}$ is added and subtracted for the sake of the semi-implicit time integration method.

27.3.2 The momentum equation

From the momentum equation, we have the pressure gradient term

$$\underline{PG} = \underline{\nabla}_{\eta}(\phi + \phi_s) + T\frac{R}{p}\underline{\nabla}_{\eta} p\,. \qquad 26.30$$

Using the hydrostatic equation, we can obtain the geopotential height between the surface ($\eta = 1,\ p = p_s$) and model level η (pressure = p) from

$$\begin{aligned}\phi_{\eta} &= \int_{p}^{p_s}\frac{RT}{p}dp = \int_{p}^{p_s}\frac{R}{p}\left\{\tilde{T} + T_0 + T_1\{p/P_{00}\}^{\kappa}\right\}dp \\ &= \int_{p}^{p_s}\frac{R\tilde{T}}{p}dp + \int_{p}^{p_s}\frac{R}{p}\left\{T_0 + T_1\{p/P_{00}\}^{\kappa}\right\}dp \qquad 26.31 \\ &= \tilde{\phi} + RT_0\ln(p_s/p) + \frac{RT_1}{P_{00}^{\kappa}}\frac{1}{\kappa}\left\{p_s^{\kappa} - p^{\kappa}\right\}\quad .\end{aligned}$$

For the pressure gradient term, we then get

$$\begin{aligned}\underline{PG} &= \underline{\nabla}_{\eta}\phi_s + \underline{\nabla}_{\eta}\phi + T\frac{R}{p}\underline{\nabla}_{\eta} p \\ &= \underline{\nabla}_{\eta}\phi_s + \underline{\nabla}_{\eta}\tilde{\phi} + \underline{\nabla}_{\eta}\{RT_0\ln(p_s/p)\} + \underline{\nabla}_{\eta}\left\{\frac{RT_1}{P_{00}^{\kappa}}\frac{1}{\kappa}\left\{p_s^{\kappa} - p^{\kappa}\right\}\right\} + T\frac{R}{p}\underline{\nabla}_{\eta} p\,.\end{aligned} \qquad 26.32$$

Now a key part of the Simmons-Chen method entails defining a modified surface geopotential which is given by

$$\tilde{\phi}_s = \phi_s + RT_0\ln(p_s/P_{00}) + C_p T_1\left\{(p_s/P_{00})^{\kappa} - 1\right\}. \qquad 26.33$$

This then gives

$$\underline{PG} = \underline{\nabla}_{\eta}\tilde{\phi}_s + \underline{\nabla}_{\eta}\tilde{\phi} + \tilde{T}\frac{R}{p}\underline{\nabla}_{\eta} p\,. \qquad 26.34$$

Note that this has an identical form to the initial definition of $\underline{PG}$ given above. If we now define a pressure field "P_{sr}" such that

$$\phi_s + RT_0 \ln(P_{sr} / P_{00}) + C_p T_1 \left\{ (P_{sr} / P_{00})^{\kappa} - 1 \right\} = 0 \qquad 26.35$$

it is found that the equation for $\tilde{\phi}_s$ becomes

$$\begin{aligned} \tilde{\phi}_s &= RT_0 \ln(p_s / P_{sr}) + C_p T_1 \left\{ (p_s / P_{00})^{\kappa} - (P_{sr} / P_{00})^{\kappa} \right\} \\ &= C_p \left[T_0 \ln \left\{ (p_s / P_{00})^{\kappa} / (P_{sr} / P_{00})^{\kappa} \right\} + T_1 \left\{ (p_s / P_{00})^{\kappa} - (P_{sr} / P_{00})^{\kappa} \right\} \right]. \end{aligned} \qquad 26.36$$

From this it can be seen that because P_{sr} will closely resemble p_s, then $\tilde{\phi}_s$ will be much more uniform horizontally than ϕ_s, especially in mountainous regions. Thus the term $\underline{\nabla}\tilde{\phi}_s$ will be correspondingly much smaller than $\underline{\nabla}\phi_s$.

The method used to obtain a P_{sr} field suitable for a spectral model is much the same as for obtaining a ϕ_s field (spectrally smoothed) from the grid point $\phi_s = gz_s$. The known ϕ_{sg} (the grid-point, non-spectrally fitted surface geopotential heights) are used to obtain the grid point values of P_{sr}, denoted by P_{srg}. These are obtained from

$$\phi_{sg} + RT_0 \ln(P_{srg} / P_{00}) + C_p T_1 \left\{ (P_{srg} / P_{00})^{\kappa} - 1 \right\} = 0 \qquad 26.37$$

which is solved by a Newton-Raphson iterative method. These grid point P_{srg} values are then spectrally fitted at the appropriate model resolution, to generate a *spectrally smooth* form of P_{sr}. This is, in fact, input to the Mk3 model in the form of a model code variable denoted by $PSRK = (P_{sr} / P_{00})^{\kappa}$. The variable $PSRK$ is used directly in the generation equation for $\tilde{\phi}_s$ shown above. The surface elevation $z_s (= \phi_s / g)$ for the Mk3 model also makes use of *PSRK* and is given by

$$z_s = -C_p \left(T_0 \ln(P_{sr} / P_{00})^{\kappa} + T_1 \left\{ (P_{sr} / P_{00})^{\kappa} - 1 \right\} \right) / g \,. \qquad 26.38$$

Returning now to the momentum equation, with the virtual temperature representation included, the term $\underline{C}$ may be rewritten (now using a global mean temperature T_{00} instead of $\overline{T}$) as

$$\begin{aligned} \underline{C} = \mu \underline{\nabla} E + \mu \underline{\nabla}(\phi + \phi_s + (\phi_V - \phi)) - \underline{\nabla}\hat{\phi} + RT_V B_p \underline{\nabla} p_s \\ - RT_{00} \underline{\nabla} p_s + \left\{ \underline{\nabla}\hat{\phi} + RT_{00} \underline{\nabla} p_s \right\}. \end{aligned} \qquad 26.39$$

Then, by implementing the Simmons-Chen method, we get:

$$\begin{aligned} \underline{C} = \mu \underline{\nabla} E + \mu \underline{\nabla}(\tilde{\phi} + \tilde{\phi}_s + (\phi_V - \phi)) - \underline{\nabla}\hat{\phi} \\ + R(\tilde{T} + T_V - T) B_p \underline{\nabla} p_s - RT_{00} \underline{\nabla} p_s + \left\{ \underline{\nabla}\hat{\phi} + RT_{00} \underline{\nabla} p_s \right\}. \end{aligned} \qquad 26.40$$

As before, by using global means and deviations, this becomes:

$$\underline{C} = \underline{\nabla}\hat{E} + \left(R\left[(\tilde{T} + T_V - T)B_p - T_{00}\right] - \left[E' + (\tilde{\phi} + \tilde{\phi}_s) + (\phi_V - \phi)\right]\frac{\partial B}{\partial \eta}\right)\underline{\nabla} p_s + \left\{\underline{\nabla}\hat{\phi} + RT_{00}\underline{\nabla} p_s\right\}. \qquad 26.41$$

where $\hat{E}$ is now defined by

$$\hat{E} = \mu E' + \mu(\tilde{\phi} + \tilde{\phi}_s + (\phi_V - \phi)) - \hat{\phi}\,. \qquad 26.42$$

It is also to be noted that

$$\tilde{\phi} = \int_p^{p_s} \frac{R\tilde{T}}{p} dp = \int_\eta^1 R\tilde{T}\,\frac{\mu\eta}{p}\, d(\ln\eta) = \int_\eta^1 R\tilde{T}_N\, d(\ln\eta) \qquad 26.43$$

and so we may use the usual (vertical) vector-matrix form $\underline{\tilde{\phi}} = \underline{\underline{A}}\,\underline{\tilde{T}}_N$. In addition, the definition of $\hat{\phi}$ is also changed, and is given by $\underline{\hat{\phi}} = \underline{\underline{A}}\,\underline{\hat{T}}$ in which $\hat{T} = \mu\tilde{T}$, the new prognostic temperature variable.

27.4 An implicit treatment of the vorticity equation (*dynmvo*).

For the sake of numerical stability, an implicit treatment of the spectral vorticity equation can be invoked. Given that the model equations (as for the current Mk3 model) are based upon those is in the sub-section above, the momentum equation (26.3) may now be re-written as

$$\frac{\partial \hat{V}}{\partial t} + \left(\hat{\xi} + \frac{\partial B}{\partial \eta}\delta_1 + \mu f\right)\underline{k}x\underline{V} = -\underline{\hat{C}} - \underline{\nabla}\hat{E} - \underline{\nabla}\hat{\phi} - RT_{00}\underline{\nabla} p_s \qquad 26.44$$

where

$$\underline{\hat{C}} = \left(R\left[(\tilde{T} + T_V - T)B_p - T_{00}\right] - \left[E' + (\tilde{\phi} + \tilde{\phi}_s) + (\phi_V - \phi)\right]\frac{\partial B}{\partial \eta}\right)\underline{\nabla} p_s + \hat{D}\underline{V} + \frac{\partial \hat{\omega}\underline{V}}{\partial \eta} - \mu\underline{F}\,. \qquad 26.45$$

The *vorticity* equation then becomes

$$\frac{\partial \hat{\xi}}{\partial t} + \underline{\nabla}.\left(\hat{\xi} + \frac{\partial B}{\partial \eta}\delta_1 + \mu f\right)\underline{V} = -\underline{k}.\,\underline{\nabla}x\underline{\hat{C}} \qquad 26.46$$

and the *divergence* equation becomes

$$\frac{\partial \hat{D}}{\partial t} - \underline{k}.\underline{\nabla}x\left(\hat{\xi} + \frac{\partial B}{\partial \eta}\delta_1 + \mu f\right)\underline{V} = -\underline{\nabla}.\underline{\hat{C}} - \nabla^2\hat{E} - \nabla^2\hat{\phi} - RT_{00}\nabla^2 p_s\,. \qquad 26.47$$

Note that the ∇^2 terms in the divergence equation can be readily represented in spectral terms and lend themselves to an implicit time integration treatment (see Gordon 1981 for details).

Consider next the vorticity equation in the form

$$\frac{\partial \hat{\xi}}{\partial t} = -\frac{1}{a\cos^2\phi}\left[\frac{\partial[\hat{A}]}{\partial\lambda} + \cos(\phi)\frac{\partial[\hat{B}]}{\partial\phi}\right] \qquad 26.48$$

in which

$$\hat{A} = \left(\hat{\xi} + \frac{\partial B}{\partial \eta}\delta_1 + \mu f\right)U + \cos(\phi)\hat{C}_\phi \qquad 26.49$$

$$\hat{B} = \left(\hat{\xi} + \frac{\partial B}{\partial \eta}\delta_1 + \mu f\right)V - \cos(\phi)\hat{C}_\lambda \cdot \qquad 26.50$$

Here we have defined $U = u\cos(\phi)$ and $V = v\cos(\phi)$. We now wish to make an implicit version of the advection in the vorticity equation (following DKRZ (1993) methods as used in the ECHAM3 model). To do this we modify the vorticity equation above by use of an (additional) implicit form of the zonal advection of vorticity:

$$\frac{\partial \hat{\xi}}{\partial t} = -\frac{1}{a\cos^2\phi}\left[\frac{\partial[\hat{A}]}{\partial\lambda} + \cos(\phi)\frac{\partial[\hat{B}]}{\partial\phi}\right] - \frac{\bar{u}}{a\cos(\phi)}\frac{\partial}{\partial\lambda}\left\{\hat{\xi}^{\tau+1} + \hat{\xi}^{\tau-1} - 2\hat{\xi}^{\tau}\right\} \qquad 26.51$$

where $\bar{u}$ is a zonally averaged wind speed. By transforming to Fourier coefficient form

(using $\hat{A} = a\sum_m \hat{A}_m e^{im\lambda}$ and $\hat{\xi} = \sum_m \hat{\xi}_m e^{im\lambda}$) gives:

$$\frac{\partial \hat{\xi}_m}{\partial t} = -\frac{1}{\cos^2\phi}\left[im\,\hat{A}_m + \cos(\phi)\frac{\partial \hat{B}_m}{\partial\phi}\right] - \alpha(\phi)\,im\left\{\hat{\xi}_m^{\tau+1} + \hat{\xi}_m^{\tau-1} - 2\hat{\xi}_m^{\tau}\right\} \qquad 26.52$$

where

$$\alpha(\phi) = \frac{\bar{u}(\phi)}{a\cos(\phi)} = \frac{\bar{U}(\phi)}{a\cos^2(\phi)} \cdot \qquad 26.53$$

This leads to

$$\frac{\partial \hat{\xi}_m}{\partial t}\left[1 + (2\Delta t)im\,\alpha(\phi)\right] = -\frac{1}{\cos^2\phi}\left[im\,\hat{A}_m + \cos(\phi)\frac{\partial \hat{B}_m}{\partial\phi}\right] - im\alpha(\phi)2\left\{\hat{\xi}_m^{\tau-1} - \hat{\xi}_m^{\tau}\right\} \cdot \qquad 26.54$$

Defining $b_m(\phi) = 1/\left[1 + (2\Delta t)\,im\,\alpha(\phi)\right]$ gives

$$\frac{\partial \hat{\xi}_m}{\partial t} = -\frac{1}{\cos^2\phi} b_m(\phi)\left[im\ \hat{A}_m + \cos(\phi)\frac{\partial \hat{B}_m}{\partial \phi}\right] - im\ \alpha(\phi) b_m(\phi) 2\left\{\hat{\xi}_m^{\tau-1} - \hat{\xi}_m^{\tau}\right\}. \qquad 26.55$$

We also have that

$$b_m(\phi)\frac{\partial \hat{B}_m}{\partial \phi} = \frac{\partial (b_m(\phi)\hat{B}_m)}{\partial \phi} - \hat{B}_m \frac{\partial (b_m(\phi))}{\partial \phi} = \frac{\partial (b_m(\phi)\hat{B}_m)}{\partial \phi} + \hat{B}_m b_m^2(\phi)\ 2\Delta t\ im\ \frac{\partial \alpha(\phi)}{\partial \phi}. \qquad 26.56$$

Then

$$\frac{\partial \hat{\xi}_m}{\partial t} = -\frac{1}{\cos^2\phi}\left[\begin{array}{l} im\ b_m(\phi)\left\{\hat{A}_m + \cos^2\phi\ \alpha(\phi) 2(\hat{\xi}_m^{\tau-1} - \hat{\xi}_m^{\tau}) + \hat{B}_m b_m(\phi)\ 2\Delta t \cos(\phi)\frac{\partial \alpha(\phi)}{\partial \phi}\right\} \\ + \cos(\phi)\frac{\partial (b_m(\phi)\hat{B}_m)}{\partial \phi}. \end{array}\right] \qquad 26.57$$

If we now define

$$\hat{B}_m^+ = b_m(\phi)\ \hat{B}_m \qquad 26.58$$

and

$$\hat{A}_m^+ = b_m(\phi)\left\{\hat{A}_m + \cos^2\phi\ \alpha(\phi) 2(\hat{\xi}_m^{\tau-1} - \hat{\xi}_m^{\tau}) + \hat{B}_m^+\ 2\Delta t \cos(\phi)\frac{\partial \alpha(\phi)}{\partial \phi}\right\} \qquad 26.59$$

we then get the final form

$$\frac{\partial (\hat{\xi}_m)}{\partial t} = -\frac{1}{\cos^2\phi}\left[im\ \hat{A}_m^+ + \cos(\phi)\frac{\partial \hat{B}_m^+}{\partial \phi}\right]. \qquad 26.60$$

Note that this is ***exactly*** the same form as the (Fourier transform equivalent) of Equ. (26.48) without an implicit treatment of the velocity term. Thus to utilize the method, we simply replace $\hat{A}_m$ by $\hat{A}_m^+$, and $\hat{B}_m$ by $\hat{B}_m^+$ before evaluating the spectral vorticity tendencies.

Note that $\cos^2(\phi)\,\alpha(\phi) = \overline{U}(\phi)/a$ and so

$$\cos(\phi)\frac{\partial \alpha(\phi)}{\partial \phi} = \frac{1}{a\cos^2\phi}\left[\cos(\phi)\frac{\partial \overline{U}}{\partial \phi} + 2\sin(\phi)\,\overline{U}\right]. \qquad 26.61$$

The method will require $\hat{\xi}_m^{\tau}$, which are available on the grid (produced during the Dynamics Loop process of transforming from spectral space to grid space). The method will also require $\hat{\xi}_m^{\tau-1}$, which will have to be generated as well. The method also requires $b_m(\phi)$, which (using real and imaginary components) can be written as:

$$b_m(\phi) = 1/\left[1 + (2\Delta t) im\ \alpha(\phi)\right] = br_m(\phi) - i\ bi_m(\phi) \qquad 26.62$$

where

$$br_m(\phi) = 1/\left(1 + \{2\Delta t\ m\ \alpha(\phi)\}^2\right) \qquad 26.63$$

$$bi_m(\phi) = \{2\Delta t\ m\ \alpha(\phi)\}\, br_m(\phi)\,. \qquad 26.64$$

Thus for the vorticity tendency evaluation, the components are:

$$\hat{A}_m^+ = \hat{A}_m \qquad 26.65$$

$$\hat{B}_m^+ = \hat{B}_m \qquad 26.66$$

for the non-implicit case and

$$\hat{B}_m^+ = [br_m(\phi) - i\ bi_m(\phi)]\hat{B}_m \qquad 26.67$$

$$\hat{A}_m^+ = [br_m(\phi) - i\ bi_m(\phi)] \left\{ \hat{A}_m + \frac{\overline{U}}{a} 2(\hat{\xi}_m^{\tau-1} - \hat{\xi}_m^{\tau}) + \hat{B}_m^+\ 2\Delta t \cos(\phi) \frac{\partial \alpha(\phi)}{\partial \phi} \right\} \qquad 26.68$$

for the implicit case. Note that the divergence equation will always use the original $\hat{A}_m$ and $\hat{B}_m$ values (i.e. the advection term in the divergence equation is not treated implicitly).

Now for the implicit vorticity treatment, we need zonal mean winds (at each model level). We also need to be able to get the meridional derivative.

Now $U = u\cos(\phi)$, and so for (e.g.) a rhomboidal spectral resolution ($m = 0, MW$) we have

$$U = a \sum_m \sum_l U_l^m P_l^m e^{im\lambda} \qquad 26.69$$

$$\cos(\phi)\frac{\partial U}{\partial \phi} = a \sum_m \sum_l U_l^m \cos(\phi) \frac{\partial (P_l^m)}{\partial \phi} e^{im\lambda} \qquad 26.70$$

in which the summations are over the range ($m = 0, MW$; $l = m, m+MW+1$). To obtain the zonal mean values we use

$$\overline{U}(\phi)/a = \sum_l U_l^0 P_l^0 \qquad 26.71$$

$$\frac{\cos(\phi)}{a}\frac{\partial \overline{U}}{\partial \phi} = \sum_l U_l^0 \cos(\phi) \frac{\partial (P_l^0)}{\partial \phi} \qquad 26.72$$

in which the summations are over the range (*l = 0, MW+1*). These also have to be generated as part of the Dynamics Loop spectral to grid transform. In practice, the terms involving $\overline{U}$ are multiplied by $F_{rd}(\eta_k)$ which varies between 0 and 1 and allows for the implicit vorticity to be gradually phased in for use in the model stratosphere only:
$F_{rd}(\eta_k) = ((0.2 - \eta_k)/(0.2 - \eta_{NL}))^2$ for ($\eta_k \le 0.2$), else $F_{rd}(\eta_k) = 0$.

27.5 Spectral diffusion of temperature (*diffn*).

For the temperature T, the horizontal diffusion is represented by

$$\mu \frac{\partial T}{\partial t} = \sim + K_H \, \underline{\nabla}_p . (\mu \underline{\nabla}_p T) , \qquad 26.73$$

which is in a flux form which maintains conservation of heat. The gradient operator should be evaluated on constant pressure surfaces, but may be expanded as

$$\underline{\nabla}_p T = \underline{\nabla}_\eta T - \frac{\partial T}{\partial p} \underline{\nabla}_\eta p \, . \qquad 26.74$$

The temperature variable in the Mk3 model is defined by $\hat{T} = \mu \tilde{T}$ where

$$T = \tilde{T} + T_0 + T_1 (p / P_{00})^\kappa , \qquad 26.75$$

and T_0, T_1 are constants. Note that due to the dependence on pressure, the temperature variable $\tilde{T}$ is much more horizontally uniform than T on model η surfaces. In order to obtain a spectral form of the diffusion that can be applied directly (and in a simple manner) on η surfaces, the diffusion term has to be approximated. We thus initially represent the diffusion by

$$\frac{\partial \hat{T}}{\partial t} = \sim + K_H \mu \, \nabla_p^2 T \, . \qquad 26.76$$

We next approximate $\nabla_p^2 T = \underline{\nabla}_p . (\underline{\nabla}_p T)$ (dropping cross products) by:

$$\nabla_p^2 T \approx \nabla_\eta^2 T - \frac{\partial T}{\partial p} \nabla_\eta^2 p = \nabla_\eta^2 \tilde{T} + \frac{T_1}{P_{00}^\kappa} \nabla_\eta^2 p^\kappa - \frac{\partial T}{\partial p} \nabla_\eta^2 p \, . \qquad 26.77$$

This gives

$$\frac{\partial \hat{T}}{\partial t} = \sim + K_H \mu \left\{ \nabla_\eta^2 \tilde{T} + \frac{T_1}{P_{00}^\kappa} \nabla_\eta^2 p^\kappa - \frac{\partial T}{\partial p} \nabla_\eta^2 p \right\} . \qquad 26.78$$

Two of these components are next approximated by

$$\mu\nabla_\eta^2\tilde{T} \approx \nabla_\eta^2(\mu\tilde{T}) - \tilde{T}\nabla_\eta^2\mu = \nabla_\eta^2\hat{T} - \tilde{T}\frac{\partial B}{\partial\eta}\nabla_\eta^2 p_s \qquad 26.79$$

and

$$\nabla_\eta^2(p^\kappa) \approx \kappa p^{\kappa-1}\nabla_\eta^2 p = \kappa p^{\kappa-1}B\nabla_\eta^2 p_s\,. \qquad 26.80$$

This gives

$$\begin{aligned}
&\mu\left\{\nabla_\eta^2\tilde{T} + \frac{T_1}{P_{00}^\kappa}\nabla_\eta^2 p^\kappa - \frac{\partial T}{\partial p}\nabla_\eta^2 p\right\} \\
&= \nabla_\eta^2\hat{T} - \tilde{T}\frac{\partial B}{\partial\eta}\nabla_\eta^2 p_s + \frac{\mu B}{p}\kappa T_1\left(\frac{p}{P_{00}}\right)^\kappa\nabla_\eta^2 p_s - \frac{\partial p}{\partial\eta}\frac{\partial T}{\partial p}B\nabla_\eta^2 p_s \qquad 26.81\\
&= \nabla_\eta^2\hat{T} - \left\{(T-T_0)\frac{\partial B}{\partial\eta} - T_1\left[\frac{\partial B}{\partial\eta} + \kappa\frac{\mu B}{p}\right]\left(\frac{p}{P_{00}}\right)^\kappa + B\frac{\partial T}{\partial\eta}\right\}\nabla_\eta^2 p_s\,.
\end{aligned}$$

For ease of spectral computation and to maintain conservation, the term multiplying $\nabla_\eta^2 p_s$ is replaced by one that contains global means:

a) T is replaced by the global mean (at level k) $\overline{T}_k$,

b) $\frac{\mu B}{p}$ is replaced by $\frac{B}{\eta}$,

c) $\left(\frac{p}{P_{00}}\right)^\kappa$ is replaced by η^κ, and

d) $B\frac{\partial T}{\partial\eta}$ is replaced by $\frac{B}{\eta}\frac{\partial\overline{T}}{\partial\ln(\eta)}$.

This gives

$$\begin{aligned}
&\frac{\partial\hat{T}}{\partial t} = \sim + K_H\nabla_\eta^2\hat{T} \\
&- K_H\left\{(\overline{T}-T_0)\frac{\partial B}{\partial\eta} - T_1\left[\frac{\partial B}{\partial\eta} + \kappa\frac{B}{\eta}\right]\eta^\kappa + \frac{B}{\eta}\frac{\partial\overline{T}}{\partial\ln(\eta)}\right\}\nabla_\eta^2 p_s\,.
\end{aligned} \qquad 26.82$$

It is to be noted that the term multiplying $\nabla_\eta^2 p_s$ is much smaller than its counterpart when deriving the spectral diffusion in sigma coordinates. It is in fact zero for the top two levels of the model.

28 Appendix C

Below is the "tree" structure of the Mk3 AGCM. It shows the calling order of the subroutines. However not all subroutines are shown - some simple subroutines and routines for optional or alternative physical parameterizations have been omitted. In addition, routines pertaining to the Mk1 version of the (coupled) model are not shown. The starting point for the Mk3 AGCM (and the Mk3 coupled model) is "*main.f*". It performs the start-up and time stepping for the model. The tree structure is now given, with the subroutine names given in italics. The subroutines called by *main* have a leading "•". The purpose of subroutines is also indicated. Given at the end of this appendix are the amendments to *main.f* to enable interfacing to the GFDL MOM2 ocean model code. The model is usually run in segments of 1 calendar month at a time.

•*readnml1*	Read control file and namelists
•*atstart*	Start AGCM
----*gauleg*	Set up Gaussian latitudes, Legendre polynomials, FFTs
------*gaussv*	
--------*ordleg*	
------*fftfax*	
------*lgndre*	
----*initial*	Initialize AGCM 1
------*vertc*	Hybrid vertical coordinates
------*openfl*	Open storage files
------*gaussj*	
----*initax*	Initialize AGCM 2
----*flatset*	Ocean current data for ice model (uncoupled)
----*filerd*	Read AGCM restart file
----*datard*	Read data files (climatological fields, e.g. SST)
------*insoilveg*	Prepare surface types for biospheric model
----*initfs*	Initialize radiation model
------*co2_read*	Read CO_2 amounts
------*o3_read*	Read O_3 amounts
------*solargh*	Solar zenith angle routine
----*icesetup*	Set up ice model
----*icecon*	" " " "
----*landrun*	Runoff routing data set
----*zerost*	Zero statistics arrays
•*atstep*	Do AGCM timestep
----*uvharm*	Spectral U,V harmonics
----*zerogi*	
********** Physics Loop **********	
----*phys*	Control of loop
------*ptog*	Physics spectral to grid
--------*mfftg*	Spectral to grid FFT
------*radin*	Physical parameterizations - see below*
------*hist_wlat*	Limited Area Model (LAM) data

------*hist_cld*
------*mfftm* Grid to spectral FFT
------*ftospec* Spectral temperature re-synthesis
------*hist_save* LAM data
------*just_fm* Mask change due to freezing/melting
----*physgm* Compute global means (physics)
****
----*zerogi*
********** Dynamics Loop **********
----*dynm* Control of loop
------*dtog* Dynamics spectral to grid
--------*mfftg* Spectral to grid FFT
------*dynmnl* Non-linear dynamics terms
------*dynmst* Statistics on pressure levels
------*mfftm* Grid to spectral FFT
------*dynmvo* Implicit vorticity (optional)
------*ftospec* Spectral synthesis of tendencies
****
----*energy* Energy diagnostics
----*specam* Spectral amplitudes
----*linear* Linear spectral tendencies
----*assel* Asselin time filter
----*uvreal* Velocities for SLT routine
********** Semi-Lagrangian Transport (SLT)**********
----*jmcgslt* SLT sequence control
------*vadvect* Determine vertical departure points
------*vinterp* Perform vertical SLT
------*jmcghor* Horizontal SLT
--------*hadvect* Determine horizontal departure points
--------*hinterp* Perform horizontal SLT
------*enforce_conq* Enforce conservation of moisture/tracers
****
----*matset* Matrices for spectral time integration
----*semii* Semi-implicit spectral time integration
----*diffn* Spectral horizontal diffusion
----*ocicurr* Ocean currents (if coupled) for ice model
********** Sea-ice Model **********
----*icedrive* Ice model sequence control
------*icetau* Prepare atmospheric stresses for ice model grid
------*icefhx* Ice-land grid matching for stresses
------*dynice* Ice dynamics
--------*timefilt* Time filtering
--------*polefilt* Polar Fourier filtering
--------*icebound* Determine sea/ice boundaries
--------*icefree* Free drift calculation
--------*cavit* Flato-Hibler (FH) cavitating fluid model
--------*icediag* Check for FH convergence
--------*advect* Advection of ice mass, concentration, heat etc
****

----*ocntau* Surface stresses for ocean model
----*ocforce* Surface forcings for ocean model

•*ateday* End-of-day jobs
----*timet*
----*prdaily* Save some daily data
----*prclza* Digital cloud/height map
----*przav* Digital latitude-height maps
----*prtcl* Digital horizontal cloud maps
----*prtt* Digital flux maps
----*prsmap* Mixed layer ocean temperature maps
----*prmlomap*

•*atemon* End-of-month jobs
----*prtcd*
----*flatme* Write ice model statistics files
----*filest* Write the AGCM statistics files
----*filewr* Write the AGCM restart file

*Subroutines called by "*radin*" (called by "*phys*" above).
Below are the main parts of the physics parameterizations.
(-----*radin* Physical parameterizations sequence control)
--------*surfset* Surface types
--------*hsflux* Surface fluxes
--------*surfupa* 1st part of surface update
----------*surfa*
----------*snowpr* 3-layer snow model
----------*stemp* 6-layer soil temps
--------*hvertmx* Vertical mixing
--------*gwdrag* Gravity wave drag
--------*rainda* Optional explicit rainfall
--------*convukmo* UKMO convection
--------*hkuo* or Kuo convection
--------*conv* or Mk1 Mass Flux convection
--------*cvmix* Momentum mixing by convection
--------*progcld* Clouds with microphysics
----------*newcloud* Mixed phase clouds
----------*newrain* Precipitation
----------*icefall* Ice fall speed
--------*surfupb* 2nd part of surface update
----------*surfb*
----------*smoisture* 6-layer soil moisture
----------*seaice* Thermodynamic part of ice model
--------*radfs* Longwave and shortwave radiation
----------*zenith* Solar zenith angle
----------*o3set* Ozone amount
----------*cloud2* Clouds : Microphysics
----------*slingo*

----------*slingi*
----------*cloud* Optional Mk1 model cloud scheme
----------*clddia*
----------*cldset*
----------*swr89* Shortwave radiation
----------*clo89*
----------*lwr88* Longwave radiation
----------*fst88*
----------*e1e288*
----------*e3v88*
----------*spa88*
--------*surfupl* Ice model : leads update
--------*cloudm* Digital cloud mapping
--------*surfdiag* Single point diagnostics
--------*hist_acc* LAM data

Interface to the Mk3 ocean model

The GFDL MOM2 ocean general circulation model (OGCM) can be run as a stand alone ocean model with suitable surface forcing – heat flux, freshwater flux and stresses. In coupled mode, these fields are generated by the atmospheric model, and passed directly to the ocean model via common-blocks inserted directly into the relevant MOM2 subroutines. Both the AGCM and OGCM use 15 minute timesteps (T63 and T63_2 resolutions respectively). The sequence of computation in the Mk3 coupled model is such that the AGCM first performs a timestep using the previous timestep OGCM sea surface temperatures and ocean currents for drift in the ice model. There then follows an OGCM timestep using AGCM forcing fields. In the routines below, the original MOM2 controlling routine "*driver.F*" has been separated into 4 sub-components : "*mom2start.F*", "*mom2_to_agcm.F*", "*mom2step.F*", and "*mom2end.F*" for Mk3 coupling purposes. In addition "*atmos.F*" below is a MOM2 supplied subroutine, modified for the coupled Mk3 model. Details about ocean model subroutines are available from GFDL, and thus a tree structure for the MOM2 model is not given here. The Mk3 coupled model version of "*main.f*" contains the following basic steps/subroutine calls (•):

•*readnml1* Read control file and namelists
•*atstart* Start AGCM
•*mom2start* Start OGCM

********** Coupled model timestep **********
•*mom2_to_agcm* Prepare OGCM fields for AGCM
•*atstep* Do AGCM timestep
•*atmos* Prepare AGCM fields for OGCM
•*mom2step* Do OGCM timestep
****
•*ateday* End-of-day jobs (AGCM)
•*atemon* End-of-month jobs (AGCM)
•*mom2end* " " (OGCM)